MSc Systems & Control

Modulation enhanced multi-emitter localization microscopy

Multi-emitter fitting with structured illumination patterns for high imaging density super-resolution localization microscopy

Ahmed Zahran

Master of Science Thesis

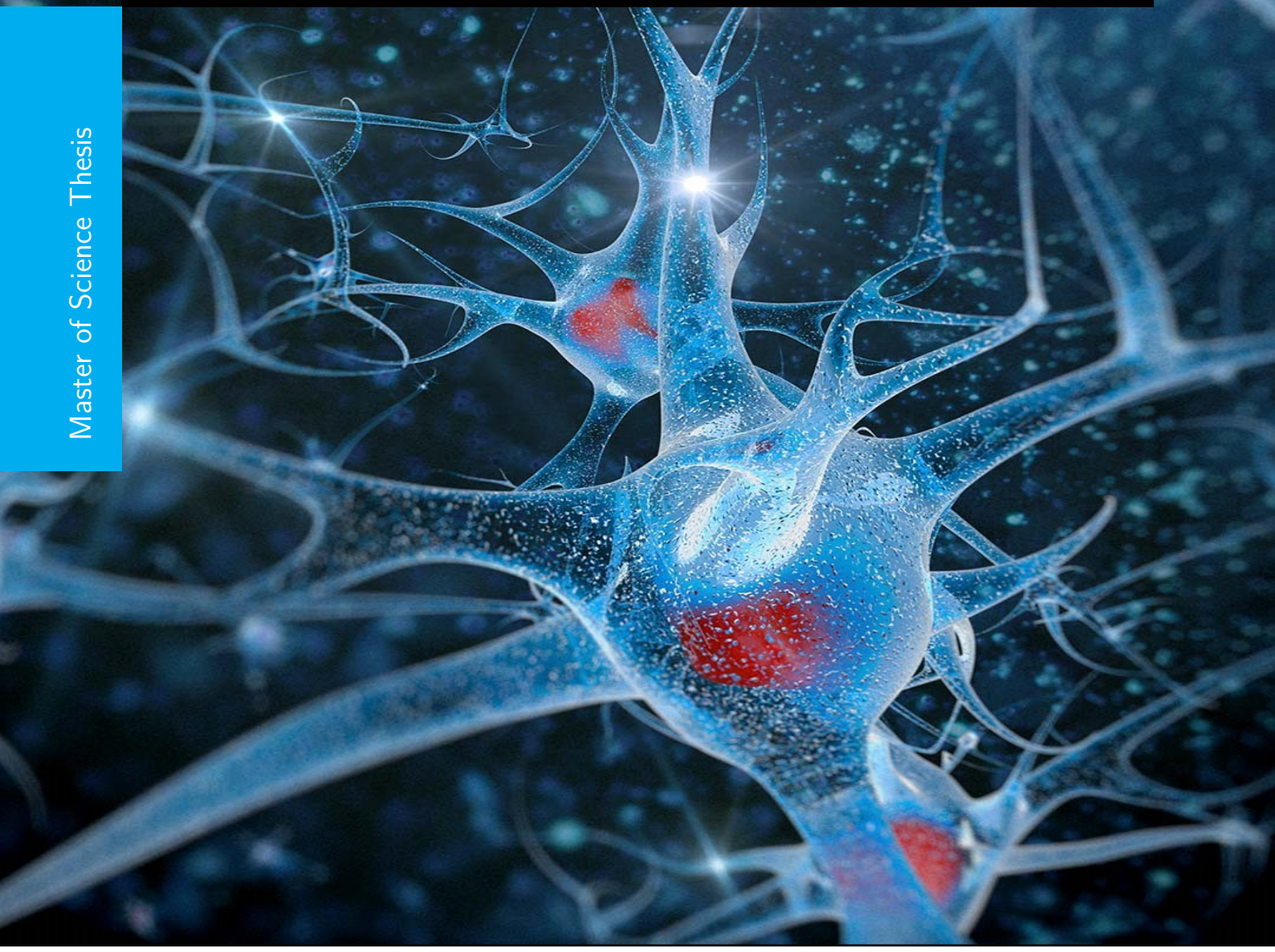

TU Delft Delft University of Technology

Delft Center for Systems and Control

Modulation enhanced multi-emitter localization microscopy

Multi-emitter fitting with structured illumination patterns for high imaging density super-resolution localization microscopy

Master of Science Thesis

For the degree of Master of Science in Systems and Control at Delft University of Technology

Ahmed Zahran

December 1, 2020

Faculty of Mechanical, Maritime and Materials Engineering (3mE) · Delft University of Technology

Delft University of Technology
Department of
Delft Center for Systems and Control (dcsc)

The undersigned hereby certify that they have read and recommend to the Faculty of Mechanical, Maritime and Materials Engineering (3mE) for acceptance a thesis entitled

Modulation enhanced multi-emitter localization microscopy

by

Ahmed Zahran

in partial fulfillment of the requirements for the degree of

Master of Science Systems and Control

Dated: December 1, 2020

Supervisor(s):

dr.ir. C. S. Smith

ir. J. Cnossen

Reader(s):

dr. ir. S. Wahls

dr. D. Boskos

Abstract

For a long time, scientists believed that it is not possible to achieve a better microscopic resolution than half the wavelength of light ($\sim 200\ nm$). During the last decades, various super-resolution fluorescence microscopy techniques have been developed, offering high-resolution imaging beyond the diffraction limit. It has been established as one of the major tools currently available for the study and analysis of biological tissues. The observation of, previously limited and unclear, cellular structures has demonstrated the great promise of super-resolution fluorescence microscopy in exemplifying biological processes at the cellular level. Inherently, single-molecule localization microscopy (SMLM) is based upon acquiring a sequence of diffraction-limited images, consisting of localizations of sparsely distributed emitting fluorophores. Next, precise and accurate estimates of the spatial coordinates of the fluorophores, placed on the structures of interest, are made. Subsequently, all recovered emitter positions from each frame are combined, and a super-resolution image is generated. One of the most crucial questions in SMLM concerns the precision with which the location of a single molecule can be determined. The Cramér–Rao lower bound (CRLB) is used to quantify the estimation performance in terms of localization precision. Recently, several modulation enhanced methods have shown resolution improvement by combining structured patterned illumination with SMLM techniques, such as MINFLUX [18] and SIMFLUX [9]. However, the analysis of images by SMLM and these modulation enhanced methods requires sparse activation regions to prevent overlap between active emitters. Recently, several methods have been developed with the ability to analyze higher density data, allowing partial overlap between emitters.

In this work, we propose a maximum likelihood-based, modulation enhanced SMLM method able to localize multiple active emitters within a single region of interest (ROI), which we refer to as Multi-SIMFLUX. The mathematical framework of the algorithm is comprehensively built up throughout this work. The performance of the algorithm has been evaluated, and validated under a wide range of realistic imaging conditions. This involves various active-emitter densities, different emitter- and background intensities, numerous emitter configurations, a multitude of ROI-sizes and point spread function widths. As theoretically expected, our approach significantly outperforms conventional $2D$-Gaussian SMLM with a twofold improvement factor in terms of localization precision for various emitter densities and intensities. At higher active emitter imaging densities, the extension from a single to a multi-emitter approach showed a clear improvement in recall fraction.

Contents

Preface & Acknowledgements **vii**

Nomenclature **ix**

1 Introduction **1**

1-1 Background & Motivation 1

1-2 Problem Formulation
State-of-the-art techniques 3

1-3 Outline of Thesis 6

2 Theory and Literature **7**

2-1 Introduction 7

2-2 The Diffraction Limit 8

2-3 Point Spread Function 8

2-4 Fluorescence Microscopy 9

2-5 Beyond the Diffraction Limit 11

2-6 Structured Illumination Microscopy 12

2-7 Single Molecule Localization Microscopy 13

2-8 Modulation-enhanced Localization Microscopy 15

2-9 The Image Processing Pipeline 16

3 Mathematical Concepts and Theoretical Limits **18**

3-1 Parameter Estimation 18

3-2 The Poisson Distribution 19

3-3 Fisher information and Cramér-Rao Lower Bound 19

3-4 Maximum Likelihood Estimation 22

3-5 The Chi-Squared $\mathcal{X}^2$-Test . . . 23
3-6 Image Formation Model . . . 23

4 Manuscript **26**
4-1 Introduction . . . 27
4-2 Methods . . . 29
4-2-1 Image Formation Model . . . 29
4-2-2 Theoretical Precision Limit . . . 30
4-2-3 Algorithm Setup . . . 31
4-3 Results . . . 38
4-3-1 Localization Performance . . . 39
4-3-2 Probability Error . . . 42
4-3-3 Separation Distance . . . 45
4-3-4 Active Emitter Density . . . 48
4-3-5 Pattern Fitting . . . 50
4-4 Discussion . . . 54
4-5 Conclusion . . . 55
4-6 References . . . 56
4-7 Supplementary Figures . . . 58
4-8 Supplementary Notes . . . 78
4-8-1 Image Formation Model - SMLM . . . 78
4-8-2 Theoretical Localization Precision . . . 80
4-8-3 Levenberg-Marquardt Algorithm . . . 85

5 Conclusion **86**
5-1 Summary . . . 86
5-2 Future Outlook . . . 88

A Appendices **89**
A-1 Fisher Information and Cramér Rao Lower Bound . . . 89
A-2 Likelihood Ratio Test . . . 93
A-3 Multiple Hypothesis Testing . . . 94

Bibliography **99**

Glossary **103**
List of Acronyms . . . 103

List of Figures

1-1 An overview of some microscopy techniques with their respective lateral resolution. 2

2-1 An illustration of the convolution between specimen and point spread function (PSF) resulting in the obtained image. 9

2-2 **(I)** The fluorescence principle. **(II)** Schematic representation of a simple fluorescence microscope setup. 10

2-3 Example of the resolution improvement achieved by super-resolution imaging techniques in comparison with conventional microscopy techniques. 11

2-4 STED and SIM imaging techniques. 13

2-5 A schematic representation of the principle of SMLM. 14

2-6 Schematic representation of the image-processing pipeline used in single-molecule localization microscopy from raw data to a super-resolution image. 16

3-1 The principle of the resolution improvement obtained by SIM 25

A-1 Schematic illustration of a decision problem. 97

Preface & Acknowledgements

"If I have seen further, it is by standing on the shoulders of Giants."
- Isaac Newton

I would like to thank my supervisors dr.ir. C. Smith and ir. J. Cnossen for their support and valuable insights during the course of my thesis. Thank you for all the given remarks and suggestions. Due to the global COVID-19 pandemic, our contact was mainly virtual. However, I am very proud of conducting my research within such an ambitious, friendly and hard-working team. A couple of months were spent contemplating over literature, writing out some tortuous mathematical derivations and of course the never-ending struggle with simulation code. All during a global pandemic which did also affect close ones unfortunately. All in all, I have learned a lot of new useful software skills and was able to improve my scientific reading and writing capabilities. At last but perhaps most important, I am very grateful for the unconditional support and love received from my family and friends, and desired distraction sometimes, which kept me going to get the best out of myself.

Delft, University of Technology — Ahmed Zahran
December 1, 2020

Nomenclature

Abbreviations

α	Maximum half-angle of acceptance $[rad]$
ϵ	Acceptable localization recall error $[m]$
η_p	Normalized relative intensity factor of the p_{th} pattern [-]
λ	Wavelength $[m]$
$\mathcal{I}(\theta)$	Fisher information matrix [-]
$\mathcal{P}$	Number of illumination patterns [-]
p	Pitch $[m]$
μ_k	Expected photon count in the k_{th} pixel [photons]
ϕ	Pattern phase $[rad]$
ψ	Phase offset $[rad]$
$\sigma_{x,y}$	Localization precision in x and y direction, respectively $[m]$
Θ	Feasible parameter space [-]
θ_{I_e}	Photon count expected from the e_{th} emitter $[photons]$
A_k	Area of the k_{th} pixel $[m^2]$
b	Border size [pixels]
E	Total number of emitters [-]
FN	False Negative [-]
FP	False Positive [-]
GT	Ground true [-]
K	Number of pixels [-]
N	Number of photons $[photons]$
n	Refractive index [-]
TP	True Positive [-]
$\Delta_{x,y}$	Pixel size in x and y direction, respectively [-]
σ/σ_{PSF}	Width of the Point-Spread Function $[m]$
σ_{CRLB}	Cramér-Rao lower bound $[m]$
θ_{bg}	Expected background count $[photons/pixel]$
m	Modulation contrast [-]


بسم الله الرحمن الرحيم

Chapter 1

Introduction

"If you accept my thesis that the universe and this earth are the most outrageous miracles by an infinite margin, then you will understand that simply for us to exist requires a miracle."

- Eric Metaxas

This chapter serves as a general introduction of this work. First, some background information and the motivation for studying single-molecule localization microscopy is given. Then, the state-of-the-art applications and limitations are briefly discussed. Finally, the scope and main focus of this thesis is stated.

1-1 Background & Motivation

Cells are considered to be the basic units of life. They have complex configurations and come in different types and forms. Proteins are the molecular building blocks and functional machines of cells and are one of the key components controlling biological processes. There are thousands of different types of proteins within the human body, each with a specific task, location and three-dimensional structure. We humans are interested in visualizing protein molecules in order to aid us in understanding and explaining complex inner structures and mechanisms in organic cells. Scientists are able to create modified proteins, which are used for the study of cellular processes on a molecular level. As a consequence, it is possible to extract useful information about the natural physiology and anomalous deviations that lead to diseases and disorders.

The Dutch scientist Antony van Leeuwenhoek has made a great contribution to the invention and development of microscopy in the $17th$ century, due to his pioneering work in the study and analysis of living micro-organisms [20]. From that point onwards, optical microscopy has played a central role in our understanding of biology and chemistry. The types and shapes of microscopes over the last decades have been continuously altered and optimized, with the aim of improving both the image resolution and acquisition speed. Nonetheless, the basic principle has somewhat stayed the same. Microscopic applications are based on the interaction (scattering, reflection, attenuation, absorption, etc.) of an electromagnetic wave with some material, where based on its response, some knowledge can be gained about its characteristics and structural dimensions.

The analysis of molecule's emission patterns is critical for obtaining structural and physiological information regarding the targeted molecules. There are several types of microscopy fields, based on their variance in energy, such as: light, electron, infrared, magnetic resonance, atomic force and x-ray microscopes. In this study, we focus on light microscopes due to their inherently minimal invasive approach, which provides powerful insights into the observation of living organisms for biological and medical research, without damaging the tissues. Light microscopes operate by making use of the visible light, with a wavelength λ of $400 - 700$ nm. This is the primary reason for them being the firmly established optical tool for biological studies, especially living cells. Other microscopes which make use of much higher energies, such as infrared or electron microscopes, are capable of achieving higher resolution. However, their energy levels are so high that even a minimal electron dose can result in heating up issues that are destructive to the sample, which makes them unsuitable for biological studies.

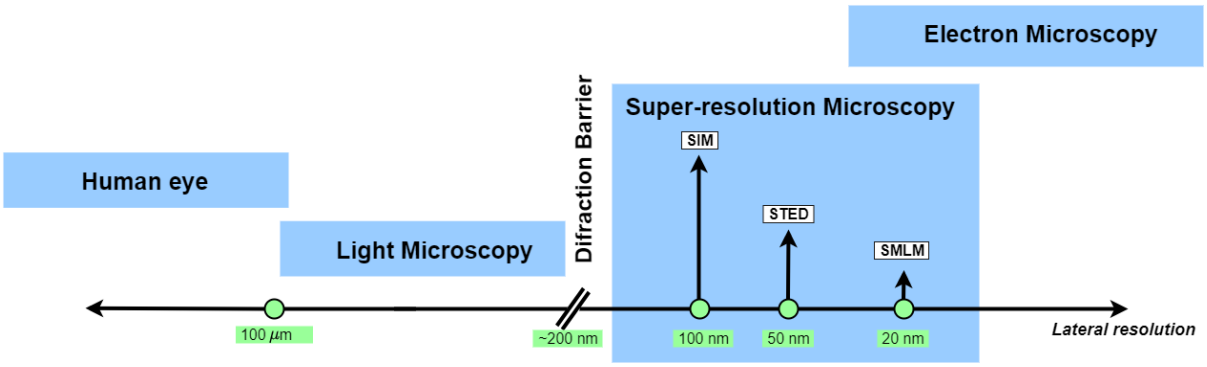

Figure 1-1: An overview of some microscopy techniques with their respective lateral resolution. Conventional light microscopy is limited by the diffraction barrier known as the Abbe-diffraction limit, $\lambda/2NA$ in the lateral direction. This limitation causes the images of objects with separation distances smaller than $\sim$ 200 nm in the lateral direction to be indistinguishable. Super-resolution microscopy methods break the diffraction barrier; some pioneer methods are shown with their average lateral resolution. In the next sections, each method is briefly discussed.

The challenging part is that proteins are typically in the range of a billionth of a meter (nm) in size, while conventional light microscopes can not observe objects this small. Conventional (fluorescence) light microscopy is limited by the physical barrier known as the Abbe-diffraction limit, quantified as $\lambda/2NA$ (see Section 2-2). This limitation prevents the images of objects with separation distances smaller than 200 nm in the lateral (x, y) direction and 500 nm in the axial (z) direction to be distinguished from each other.

The widespread advancements of microscopy have been driven by the coherent engagement of physicists and mathematicians in optimizing the optical hard- and software instruments, alongside biologists and chemists facilitating and extending the use of fluorescent proteins. This is where super-resolution imaging techniques have revolutionized (fluorescence) light microscopy. The tremendous increase in the amount of data available, should permit the development of image analysis tools that are able to extract more valuable information, making the image analysis procedure significantly more quantitative. The availability of advanced and sensitive optical instrumentation has further permitted the acquisition of super-resolution images of densely packed regions and complex cellular structures. It has enabled the study of cell structure details and dynamics of cellular events. For instance, it gives us the ability to visualize and study the process of synapse creation between nerve cells within the brain, the ability to track and trace proteins involved in certain diseases such as AIDS, Cancer or Alzheimer, the applications are numerous and boundless. Perhaps more applicable these days, is the role that microscopes can play in the study of the ongoing pandemic due to the emergence of the new Corona (SARS-CoV-2) virus in December 2019, in a market in Wuhan, China. This virus is currently being witnessed by more than 150 countries, has infected more than 60 million people around the world, and has resulted in the death of more than 1.4 million people[4].

1-2 Problem Formulation

State-of-the-art techniques

Single-molecule localization microscopy (SMLM), with its variations, is currently one of the broadly used super-resolution imaging techniques. The probe-based super-resolution techniques, such as Photo-activated localization microscopy (PALM) [46] and Stochastic optical reconstruction microscopy (STORM) [26;45;17], achieve lateral spatial resolution in the range of $\sim 20\ nm$ instead of $200-300\ nm$. Regardless of their extraordinarily lateral spatial resolution and their ease of implementation, there are still some factors limiting the resolution. The majority of the leading methods in the field of SMLM, face three fundamental issues: achieving sub-optimal localization precision, lengthy acquisition/data-processing time and sample-dependent parameter tuning. Localization microscopy inherently requires a large number of imaging cycles ($\sim 10^3 - 10^5$) [32] in order to generate one single super-resolution image. Due to the fact that they make use of sparse emitter activation, the chance of emitters overlapping each other is minimized. At the same time, this is one of the main causes of the enduring acquisition/data-processing times, hindering the throughput and live-cell imaging applications. On top of that, some of the applications of these techniques require an estimate of the Point spread function (PSF). Meaning that uncertainties in the PSF estimation affect the confidence in the recovered signals directly. Therefore, most single-molecule localization based techniques are restricted to the analysis of a small number of cells. Also, unavoidable or unnoticeable acts during sample preparation could lead to alteration or damages to the cellular structure, leading again to inaccurate results.

The number of photons collected from a fluorophore is a major decisive factor for the localization precision in SMLM, and so for the resolution of the generated super-resolution images. The labeling density is another main factor which affects the resolution. When the targeted structure is not sufficiently labelled, inaccurate observations can be obtained, e.g. causing in-reality continuous structures to appear discontinuous. However, too high spatial densities of activated molecules can result in a crowded field of activations, thus providing inaccurate or unsatisfying results. When there are too many photo-activated molecules in a single camera frame, their PSFs start to overlap, resulting in a number of non adequately resolved fluorophores. This increases the active density and hence decreases the spatial resolving power. In other words, the overlapping of PSF's reduces the ability to distinguish single emitters from each other, by which the whole benefit of SMLM is hardly utilized. The effect of labeling density on the effective spatial resolution can be quantified by the Nyquist criterion [26]. This consideration has to be made in nearly all super-resolution fluorescence microscopy methods, including STED [25;54], (S)SIM [52;21;1], (F)PALM [17;46] and STORM [26;45;17]. Likewise, the choice between organic dyes and fluorescent proteins (FPs) is an issue to deal with. Organic dyes are inherently brighter and have more ideal photophysical properties, applicable for super-resolution imaging, in comparison to FPs. However, the size of FPs is much smaller, making them more convenient for viewing the structures and dynamics of molecular regions of interest, yet also causing the labelling and localization procedure to be more time consuming. Several methods on combing benefits of both sides are conducted and are still ongoing [39;30]. Regardless of the fact that this topic is outside of the scope of this thesis, we foresee that the further development and investigation of efficient and specific labeling methods will be of great benefit for super-resolution fluorescence microscopy [26].

Obtaining accurate and precise information regarding the dynamics of biological processes, depends on both temporal and spatial resolutions. Due to the trade-off between the temporal and spatial resolutions, involved in basically all super-resolution imaging techniques, super-resolution fluorescence microscopy is intrinsically slower than conventional fluorescence microscopy under the same conditions [26]. Different kinds of approaches have been developed and utilized to approach these issues. For example: the usage of brighter dyes with faster switching kinetics, higher power lasers and faster camera's (e.g. sCMOS's and EMCCD's) which allows minimization of exposure time while maintaining a high S/N ratio [45;26]. For increasing the acquisition speed, typically the total area coverage is reduced or larger pixel sizes are used [27]. Faster switching rates are able to improve temporal resolution; however, such wavelengths and high excitation intensities have shown to increase phototoxicity [11].

Further, it is possible to achieve higher spatial resolution in the lateral direction, by considering a smaller pixel size. However, this is inherently associated with a longer acquisition time. The number of active fluorophores per frame can be increased, which improves the image acquisition, yet causing a degrading effect on the spatial resolution. In general super-resolution imaging techniques tend to achieve the necessary resolution, but lack the acquisition speed. In contrast, widefield imaging provides more or less the desired speed, but lacks the desired resolution.

Recently, a couple of modulation-enhanced localization microscopy (meLM) techniques have been developed, such as MINFLUX [18] and SIMFLUX [9]. These techniques are based on combining the structured illumination patterns of SIM (or doughnut illumination shapes of STED) and the emitter sparsity characteristic of SMLM, with the aim of taking benefit of the advantages of both techniques. The controlled construction and displacement of the illumination pattern, instead of uniform illumination, provides extra information; since it allows for the measurement of modulation fluorescence intensities coming from isolated emitters. Collecting thousands of frames allows the reconstruction of super-resolution images with a spatial resolution beyond the diffraction limit [32]. However, for obtaining optimal spatial resolution of cellular structures and dynamic processes, densely labelled structures can be unavoidable. As the amount of information available per area is related to the density of active emitters and their localization precision in this certain area. Current localization techniques are requiring fluorescence emissions of individual fluorophores not to overlap, which limits the number of fluorophores to be localized in a given frame, and hence affects the acquisition time negatively. Using the same optical setup, as in conventional light microscopy, for the generation of super-resolution images requires longer acquisition time to obtain more spatial information, which leads to a trade-off between spatial and temporal resolution. Initially, only imaging frames with well-isolated non-overlapping emitters were considered in the analysis. It is suggested that by allowing multiple emitters within a region of interest (ROI), instead of a single emitter, the overall performance of SMLM can be significantly improved, in terms of acquisition speed and a higher active single-frame density. Since SMLM is dependent on the localization of sparsely activated emitters, which cannot be guaranteed in all cases, a lot of data is being rejected. Several multi-emitter fitting techniques have been developed, aiming for exploiting all available fluorescence data, consequently leading to a resolution improvement at high molecular densities and the ability of resolving overlapping emitters, while minimizing the computational effort, e.g. FALCON [36], 3B [11], SPIDER [29], BAMF [19] and MFA [28]. They are computationally demanding, hence inherently dependent on high quality hardware and efficient and accurate algorithms for the reconstructions of super-resolution images.

Parallel to this, is the ongoing revolution of deep learning applications, which has demonstrated the capability of deep learning techniques in the handling of enormous amounts of data within a decent amount of time and impressive results in diverse image processing and computer-vision applications have been achieved. Deep learning is a branch of machine learning, which is a subset of the field of Artificial Intelligence (AI). AI traditionally refers to the theory and development of systems able to mimic human-like intelligence, in its ability of visual perception, speech recognition, learning, reasoning, planning and decision-making. Machine learning, by using statistical methods and algorithms, has the capability to learn and adapt to new events and improve by experience. The deep learning technology is a rapidly growing data-driving technique, which popped up in the 1940s [35]. It structures algorithms in layers to create artificial neural networks (ANNs), which can "learn and gain experience" and based on that addressing diverse types of problems and making intelligent decisions. Moreover, it can achieve unprecedented acquisition speeds, due to leverage Graphics processing unit (GPU) computation and parameter-free procedures. Inherently, this requires minimal expertise from the user. Several methods and techniques have already been demonstrated employing deep neural networks for super-resolution imaging enhancement, learning meaningful features, segmentation, particle tracking and many other purposes [13;50;40;42]. The state-of-the-art of deep neural networks architectures and algorithms, applied for localization microscopy show much potential. For example, a method called "Artificial Neural Network Accelerated PALM ", i.e. ANNA-PALM [42], is a neural network able to accelerate the PALM technique.

The principle of ANNA-PALM is as follows: it is an artificial neural network, which is trained on localizations from a sparse number of frames (so not all available frames) matched with dense localization data, obtained from long-duration acquisition of the same frames. Afterwhich the neural network is able to generate accurate super-resolution images from a smaller number of frames. Basically, the neural network is being trained to reconstruct high-quality super-resolution images from small numbers of frames. However, ANNAPALM requires long data post-processing procedures, and its performance is highly dependent on the availability and amount of training data, which in some cellular imaging applications not easy attainable or available at all. For new samples with prior unknown structures, so no training data available yet, the traditional techniques would be more reliable due to the lower risk of introducing image artifacts. Another deep learning based super-resolution method, called Deep-STORM [40], applies a fully convolutional neural network for the reconstruction of super-resolution images from dense fields of overlapping emitters. So it is not based on localizing single emitter, instead it creates a super-resolved image from the raw data directly, which makes it capable of achieving superior speed to conventional localization techniques. Some of the drawbacks of Deep-STORM method is that it is restricted to $2D$ localization, extending it to $3D$ is currently computationally inefficient. It is also unable to make use of the large number of post-processing methods available due to the fact that its output is not the usual format of a list of localizations.

All in all, there is still much space for improvement of the spatio-temporal resolution of SMLM applications. We foresee a bright future for deep learning and its contribution to super-resolution imaging techniques. However, to the best of our knowledge they have not shown groundbreaking results yet. Taking the above mentioned notations and discussions into consideration, we assume that exploring a new multi-emitter localization algorithm for enhancing the recall fraction at high active emitter density with a minimal loss in localization accuracy and precision, will directly benefit the SMLM-field in positive sense. In this thesis, we propose a method, which is based on combining and extending the modulation-enhanced localization microscopy technique SIMFLUX [9] and the multi-emitter fitting technique MFA [28]. This method will allow imaging frames to contain a higher active emitter density, which will benefit the acquisition speed positively. We foresee that after developing and optimizing this approach, it will be useful in particular for very highly densed regions and for high-speed live imaging. From now on, we will refer to the novel method as Multi-SIMFLUX (and just SIMFLUX interchangeably). Ideally, it will achieve a localization precision comparable with single-emitter localization methods, but provide an increased recall fraction at high active emitter densities. The method will be certified on simulations first, then put to the test on experimental data.

1-3 Outline of Thesis

This section provides an outline of the remainder of this study to provide guidance during the reading process. It is tried to make this work as self-contained and smooth to read as possible. Although it might not necessarily be complete, hopefully the relevant topics are adequately covered. The remainder of this study can be listed as follows:

- **Chapter 2**,
  Provides an overview of the relevant related background theoretical information to understand the state-of-the-art methods in the literature on super-resolution microscopy.
- **Chapter 3**,
  Discusses the mathematical concepts of imaging forming models, statistical properties of photon collection, parameter estimation, to provide the underlying theories, mathematical foundations and theoretical limitations.
- **Chapter 4**,
  In this chapter, the main findings of my thesis are presented and discussed in the form of a paper-draft manuscript. It starts by a short introduction followed by the mathematical framework which describes the problem formulation, the expected theoretical localization improvement and an outline of the algorithm setup. The theoretical results are numerically simulated in order to verify the expectations. Furthermore, there are some references for supplementary notes and figures for more in-depth clarifications and additional observations.
- **Chapter 5**,
  Serves as a summary of the main findings and insights gained during this study. It provides the reader with some concluding remarks and future recommendations for potential prospective studies on the discussed topics, to constantly work towards a more reliable and robust single-molecule localization microscopy algorithms.
- **Appendices**,
  In Appendix A, several preliminary mathematical notations and derivations considered during the work are provided.

Chapter 2

Theory and Literature

"Facts can not be observed without the guidance of some theory."
- Auguste Comte

In this chapter, the theory behind optical microscopy is briefly introduced and the relevant topics are elucidated. In order to make theoretical descriptions easily understandable, some general concepts, such as the fluorescence phenomenon, the point spread function, the diffraction limit and super-resolution are briefly discussed. Further, several essential discoveries and developments of microscopic techniques are stated. Subsequently, a concise overview is given of the main findings and insights gained during the literature study, while shortly mentioning the state-of-the-art super-resolution techniques.

2-1 Introduction

Microscopy makes use of an instrument, unsurprisingly called a microscope, which allows us to observe objects that are too small for the naked eye to be seen. Optical microscopes (regularly referred to as light microscopes) make use of the visible light, with a wavelength λ of $400 - 700$ nm. This is the major reason for them being the firmly established optical tool for biological explorations, especially living cells. Since visible light is minimally invasive and is minimally absorbed by the specimen, which mostly consists of water, it does not result in heating up issues of the sample. Conventional light microscopy is based on the principle of transmission and reflection of visible light transmitted through a series of lenses, where the image is captured by a digital camera or observed by the observer's eye directly. Essentially, biological samples are transparent, which hinders the image from obtaining all the details and structures of the molecules of interest. Thus just by transmission or reflection, the regions of interest are hard to distinguish from other objects and/or the background. This is a clear indication for the necessity of image contrast enhancement techniques. Fluorescence microscopy is the ultimate technique due to its specificity, as it is able to show the regions of interest, while all other objects and the background are set black. This feature gives fluorescence microscopy its intrinsic selectivity characteristics, which is the reason that it has become one of the main tools in current biological studies[33].

2-2 The Diffraction Limit

In the last few centuries, a huge number of technological developments led to significant advancements in the field of microscopy. However, there are still some limitations imposed by the diffraction limit of light. This physical phenomenon is referred to as the diffraction limit/barrier, known as the Abbe-diffraction limit [16]. Abbe made the statement that the resolution of an imaging instrument is not only constrained by the quality of the optical instrument, but also by the wavelength of light used [23;34]. The Abbe-diffraction limit, in the lateral and axial direction, is defined as follows:

$$Resolution_{x,y}: \ \sigma_{x,y} = \frac{\lambda}{2NA} \qquad Resolution_{z}: \ \sigma_{z} = \frac{2\lambda}{NA^2} \tag{2-1}$$

It is basically the disability of optical instruments to distinguish between two objects separated by a distance less than $\sigma_{x,y}$ and σ_z in the lateral and axial direction, respectively. Therefore, it describes the smallest level of detail (resolution), which the optical instrument is able to image. It can be considered as a low-pass filter, as the information coming from any structures with higher spatial frequencies (shorter wavelengths) will not be involved in the captured image. In microscopy, objective lenses with a numerical aperture NA of 1.2 or higher, are often used for the imaging of single fluorescent molecules in order to collect as many emitted photons as possible. The objective's NA is defined as NA$= n \sin \alpha$, where n is the refractive index and α is the maximum half-angle of acceptance by the objective. It should be noted that high-NA objectives can collect a broader range of angles. The collection efficiency of the emitted photons is proportional to α as follows; $(1-\cos\alpha)$ [48]. Even in case of using optical instruments equipped with the highest quality lenses, highest NA and incompatible immersion oil the resolution is still limited by the diffraction barrier.

2-3 Point Spread Function

An important characteristic of a microscope is the so-called point spread function (PSF). The spot created due to light diffraction is called the PSF. The PSF describes the impulse response of a microscope to a point source of light. The emission patterns of tiny light sources, i.e. PSFs, encode information about the molecule's location and orientation. The diffraction of light determines the resolution limit of microscopes, what blurs out any point-like object to a certain size and shape. For a proper calculation of the PSFs of objectives with these high NAs; vectorial effects, aberrations introduced by the specimen or by inevitable imperfections in the optical system, must be taken into consideration. The degree of spreading (blurring) of the point object is a measure for the quality and sharpness of an image. The PSF is usually taller than it is wide, since optical microscopes have worse resolution in the axial direction than in the lateral direction [22]. The PSF of the optical system is characterized by its width σ, which is related to the NA and the fluorescence emission wavelength λ. The shape of the PSF remains the same everywhere in the imaging space. The obtained image of an object is the convolution of the object and the PSF. Mathematically speaking, the blurring effect is described by the following convolution:

$$Specimen \circledast PSF = Image$$

where $\circledast$ is the $2D$ convolution operator (see Supplementary Notes in Section 4 for more details). This means that actually the output of the microscope is a convolution of the PSF with the specimen. So in reality, we do not know what the actual specimen looks like, since we get a blurred image. Considering the fact that we can record both the observed image and the PSF, with an operation called deconvolution, it is possible to reverse the blurring effect of the PSF on the specimen and get an unblurred image.

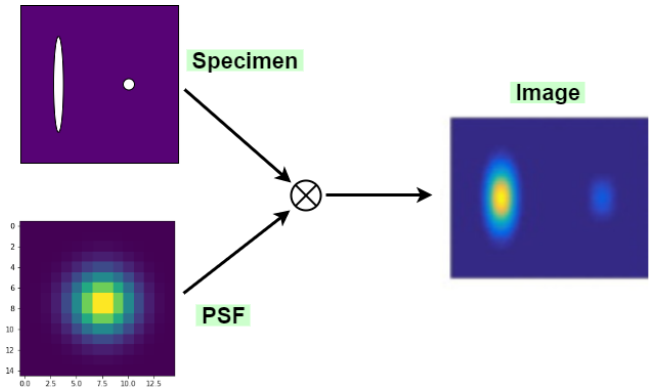

Figure 2-1: An illustration of the convolution between specimen and point spread function (PSF) resulting in the obtained image. The PSF carries information about the effect of the imaging system on the specimen i.e., the $2D$ spatial impulse response of the imaging setup.

The relation between the observed image and the raw true image can be described as follows: $Y = Cx + v$. The observed camera image is stored in a vector Y, a matrix C describes the convolution matrix defined by the PSF, the signal vector x contains the discretized intensities of the fluorophores of the raw image and v is introduced to represent the measurement noise. Another characteristic of an optical system is its optical transfer function (OTF). The OTF of an optical system is basically the Fourier transform of the PSF, which describes the response of an imaging system as a function of spatial frequency. Any imaged object can thus be thought as a linear combination (superposition) of spatial frequencies. The OTF of the lens is bandlimited. The lens acts as a low-pass filter with cutoff frequency ω_c, defined as:

$$\omega_c = \frac{4\pi NA}{\lambda} \tag{2-2}$$

The higher the cutoff frequency, the more high frequency details can be captured by the lens, the higher the image quality will be. A variant of the OTF is the MTF, which neglects phase effects, and is equivalent to the OTF in many cases.

2-4 Fluorescence Microscopy

The introduction of fluorescence microscopy in the 20_{th} century has revolutionised the use of optical microscopy in the fields of medicine and biology [23;31;33]. Fluorescence microscopy is much the same as conventional light microscopy, with additional features to enhance its contrast enhancing capabilities. Fluorescent imaging has provided an invaluable insight into many cellular structures and functions within biology. It gives the ability to visualize, out of the total sample, the desired organelles or specific features of interest. A specimen is illuminated with a specific wavelength (energy), which is absorbed by fluorescent molecules, called fluorophores. Fluorophores are fluorescent chemical compounds that can re-emit light upon light excitation, whose detection and tracking, based on their emission patterns, has laid the foundation for modern imaging methods [33;7]. The incoming light excites the orbital electron to a higher orbit. Subsequently, when relaxing to its so-called "ground state" (the initial orbit), it emits a photon of lower energy (longer wavelength) typically a few nanoseconds later. Thus, the excitation wavelength is always higher than the emission wavelength ($\sim 10 - 100\ nm$), which is also known as the Stokes shift (see Figure 2-2-I) [33]. This transition, to an excited state, happens very rapidly (in femtoseconds) [33]. Not always is all energy released in the form of light, also in the form of heat by vibrations or later (seconds to hours) via phosphorescence or transferring it to a neighbouring molecule [14].

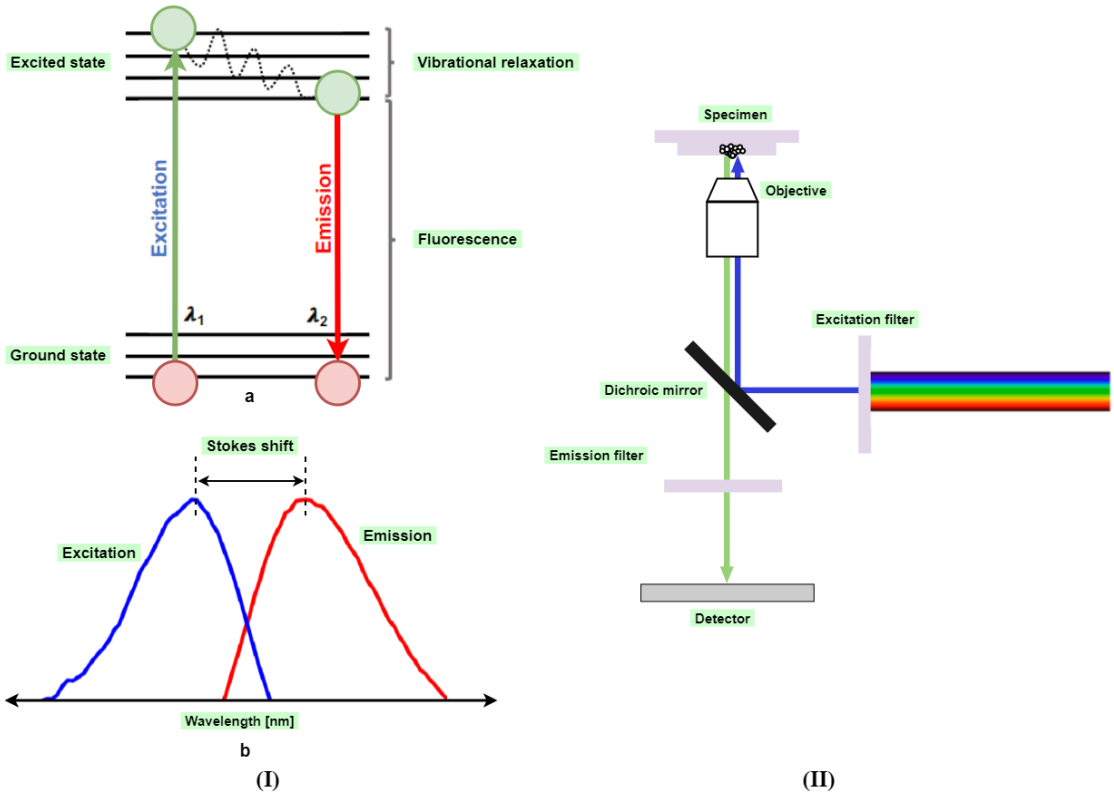

Figure 2-2: **(I)** The fluorescence principle. **(a)** A simplified Jablonski diagram. The incoming laser, excites an electron from its ground state to a higher nuclear vibrational level. After some fast vibrational relaxation (i.e. energy dissipation), the electron reaches the bottom of the excited level band, subsequently it decays back to its ground level while emitting a photon of lower energy, longer wavelength. **(b)** The Stokes shift - the difference between the excitation and emission spectrum due to energy losses. **(II)** Schematic representation of a simple fluorescence microscope setup. The specimen is illuminated with light that passes through the excitation filter, which dismisses the wavelengths that do not match the excitation spectrum of the used fluorophores. Then, the excitation light is reflected by the dichroic mirror and focused by the objective lens on the specimen. Fluorophores labels in the specimen absorb excitation light and emit fluorescence. The illumination (excitation) path is shown in blue and the image-forming (emission) path in green. The emitted light is then collected by the same objective and passes back through the dichroic mirror to the detector.

The 2008 Nobel Prize winners for chemistry, O. Shimomura, M.Chalfie and R. Tsien, had a major impact on the field of fluorescence microscopy, with their discovery and development of the green fluorescent protein (GFP)[44]. Fluorescence microscopy is able to contribute, by precisely labelling one or multiple parts of cells with different (non-overlapping excitation/emission spectra) fluorophores, whereby particular cell parts can be distinguished. A simple schematic representation of a fluorescence light microscope is shown in Figure 2-2-II. Typically lasers, light emitting diodes (LEDs) or even lamps are used as light source, followed by an excitation filter, which allows certain illumination wavelengths (depending on the application) to pass through. The light source coming through the excitation filter reaches a dichroic mirror, which acts as a beams splitter. It reflects shorter wavelengths that typically excite fluorophores, and transmits longer wavelengths that are emitted through. The shorter wavelengths reach the specimen, where a portion of the light is absorbed, a portion passes through and the rest is reflected back. The emitted light is then collected by the objective and passes back through the dichroic mirror to the detector. Since fluorescence signals are often weak, one of the main requirements for the camera is a high sensitivity and low readout noise, typically Electron-Multiplying Charge-Coupled Device (EMCCD) or scientific Complementary Metal-Oxide Semiconductor (sCMOS) cameras are used. One of the most widely used types of fluorescence microscopes is the widefield fluorescence microscope. The primary advantages of widefield fluorescence microscopy is that it allows for fast image acquisition, since it captures the whole field of view in one shot, makes use of low and uniform illumination doses and its relative ease of use.

2-5 Beyond the Diffraction Limit

In the past few years, a couple of so-called "super-resolution" microscopy techniques have been introduced, which are able to surpass the diffraction barrier. These techniques have resulted in a significant improvement in spatial resolution in three-dimensional sense. Super-resolution fluorescence microscopy has been established as one of the major tools currently available for the study and analysis of biological tissues. For a long time, scientists believed that it is not possible to achieve a better microscopic resolution than half the wavelength of light ($\sim 200\ nm$). The observation of, previously limited and unclear, cellular structures has demonstrated the great promise of super-resolution fluorescence microscopy in exemplifying biological processes at the cellular level [26].

Recently, combining several different principles together is being applied, able to reinforce each other by trying to benefit from each individual strengths and minimize their weaknesses. One of the ground-breaking discoveries was e.g. in 2014, by Eric Betzig, Stefan W. Hell and William E. Moerner, which was awarded the Nobel Prize in Chemistry [2], for their astonishing work in achieving resolution better than the limit imposed by Abbe's diffraction barrier. They worked on two separate principles, namely Stimulated emission depletion (STED) microscopy and Single-molecule localization microscopy (SMLM). The main idea of STED is modifying the excitation light pattern, through some controlled engineering to produce a much smaller focal spot size of the PSF. There is a diverse variety of super-resolution SMLM techniques, which are all more or less based on the same principle; bringing fluorophores in a controlled fashion in an ON or OFF state. In the coming sections we list and review some of the most applied principles in the current state of development, discussing their individual strengths and weaknesses.

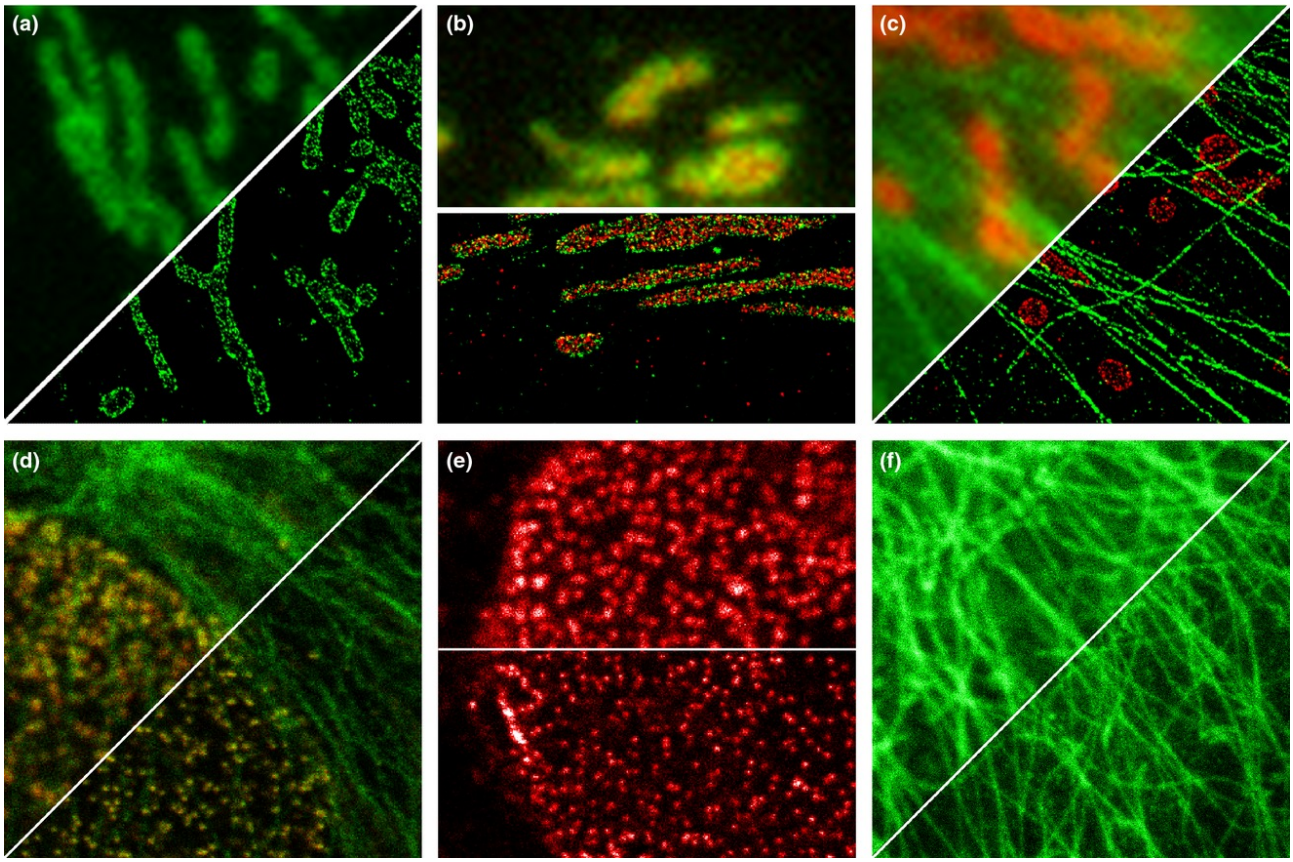

Figure 2-3: An example of the resolution improvement achieved by super-resolution imaging techniques in comparison with conventional microscopy techniques. All images are $10 \times 10\ \mu m$ in size. **(a-c)** Super-resolution images acquired with STORM and conventional images obtained using TIRF microscopy. **(d-f)** Super-resolution images acquired with STED and conventional images obtained using confocal microscopy [53].

2-6 Structured Illumination Microscopy

In structured illumination microscopy strategies, instead of illuminating the sample with an uniform field of light, a pattern has been put into the illumination. STED is first proposed and demonstrated in the 1990's[25]. In STED fluorescence microscopy, two synchronized and center-aligned intense laser beams are used. Intense radiation from the first laser beam, excites fluorescent molecules to glow producing a "standard" diffraction-limited PSF; then stimulated to return to its ground state, while the other pulse is a centered zero intensity doughnut-shaped laser beam (see Figure 2-4a). This results in a cancellation of fluorescence, except in a small (nano-sized) region located in the center of the STED beam[25], resulting in a substantially smaller effective PSF. The synchronization between the first and second pulse lasers are within hundreds of picoseconds[15]. Currently, the state-of-the-art achieved lateral resolution is typically in the range of $\sim 20\ nm$[24]. However, whether such results can be achieved in living cells without causing phototoxicity is an ongoing debate. A drawback of this method is that, it requires a complicated alignment of the optical setup and the usage of high power lasers, which can result in photo-bleaching (the photochemical alteration of a fluorophore molecule such that it is permanently unable to fluoresce) or damaging the sample in some cases. Regardless of these issues, it has been demonstrated that its usage is applicable for the study of dynamic processes in living cells[5].

Structured illumination microscopy (SIM) makes use of the so-called Moiré effect, making it able to achieve higher resolution in comparison with the conventional diffraction-limited microscopes. The Moiré effect is a phenomenon that occurs, when two high-frequency patterns are similar in structure but slightly shifted or displaced with respect to each other (see Figure 2-4b). Resulting in the creation of a third pattern with a lower frequency, which changes as the relative position of the two patterns change. SIM makes use of this principle to extend the microscope's region of spatial frequency support. The image is then reconstructed with the aim of extracting all the present information.

As previously mentioned, an essential characteristic of an optical system is its OTF. The OTF of an optical system is in essence the Fourier transform of the PSF, which describes the response of an imaging system as a function of spatial frequency. In the control theory realm, we call it the impulse response of the system. SIM basically increases the accessible Fourier space and therefore increases the number of accessible spatial frequencies. Thus, SIM uses a patterned illumination, where the spatial frequencies of the illumination pattern interfere with those of the sample features, resulting in new shifted frequencies. The shifted frequencies are lower than the cutoff frequency of the system, thus are detectable by the microscope (see Section 3-6). However, SIM is limited by the high risk of reconstruction artifacts, and is only capable of doubling the spatial resolution by combining two diffraction-limited sources of information, since the illumination pattern itself is also limited by the diffraction of light[23;26;45].

Saturated structured illumination microscopy (SSIM) is an extension of SIM, which utilizes the saturation of fluorescence emission that typically happens when the fluorophore is illuminated with very high intensity light[1;23]. The saturated excitation illumination produces narrow lines, between the high intensity levels of fluorescence, which are then used to generate a negative imprint of the imaged sample. The super-resolution image is then retrieved by some mathematical post-processing techniques. The SIM is able to achieve a resolution of $\sim 100\ nm$ and $\sim 300\ nm$ in the lateral and axial direction respectively[23;45], whereas SSIM is able to achieve $50\ nm$ resolution in both directions[1].

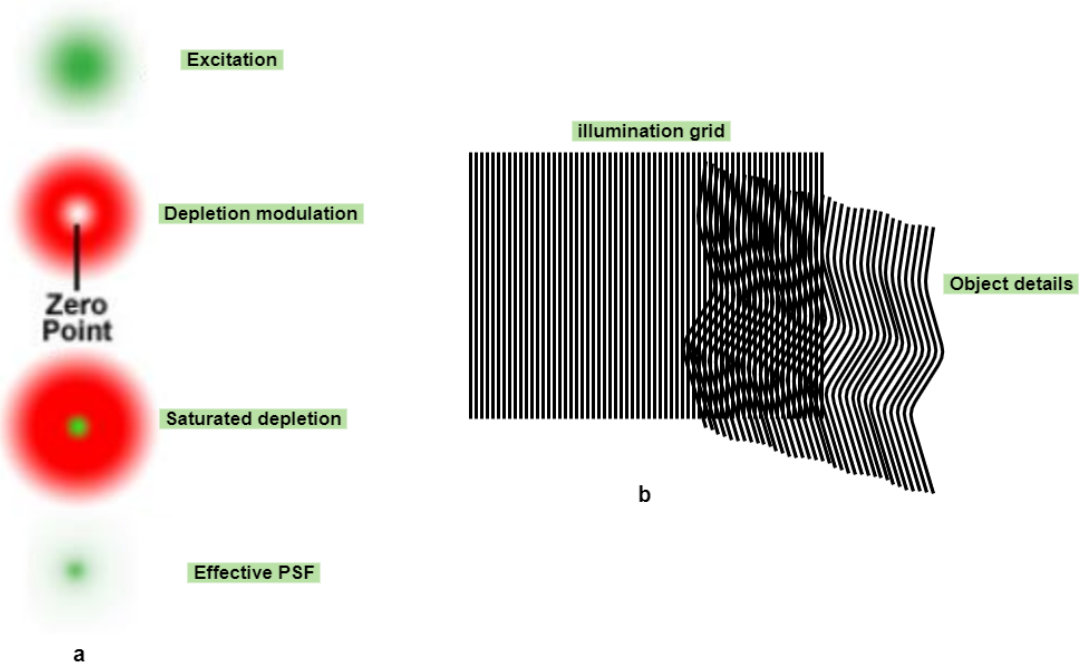

Figure 2-4: STED and SIM imaging techniques - **(a)** STED makes use of the two illumination laser beams (excitation and doughnut-shape depletion modulation), the first to excite fluorophores and the latter to deplete fluorescence, except for a small-sized region in the center. The resulting effective PSF, much smaller than the initial, is used in the process of scanning across the sample to create an improved super-resolution image. **(b)** Visualisation of the Moiré effect used in SIM. Fine object details and structures, which previously could not be resolved, become visible and distinguishable due to the interference with the structured illumination pattern.

2-7 Single Molecule Localization Microscopy

Super-resolution fluorescence imaging by single-molecule localization microscopy (SMLM) techniques, has fundamentally revolutionized the understanding of diverse cellular structures, functions and dynamics occurring at the molecular level [9]. Inherently, SMLM is based on acquiring a sequence of diffraction-limited images, consisting of localizations of sparsely distributed emitting fluorophores. Next, precise and accurate estimates of the spatial coordinates of the fluorophores, placed on the structures of interest, are made. Subsequently, all recovered emitter positions from each frame, are combined and a super-resolution image is generated. An advantage of this technique over other mentioned super-resolution techniques such as STED [25] and (S)SIM [1], is that it can be implemented using relatively simple and conventional microscopes [9]. A crucial remark is that, although the fluorescence signal coming from an active fluorophore is diffraction-limited, the precision of determining the fluorophore's position is not. Thus, the number of detected photons N will be decisive to the enhancement of localization precision. The image of a single fluorophore is obtained in the form of a PSF. The unbounded limiting value of localization precision of SMLM methods is proportional to $\sim \frac{\sigma_{x,y}}{\sqrt{N}}$. Hence, increasing the NA of the objective lens, shortening the emission wavelength (without damaging the specimen), increasing the photon emission rate (since the localization precision is inversely related by (the square root of) the number of photons captured) or improving the optical efficiency, will result in localization precision improvement. Typically, thousands or even millions of fluorophores are used in labelling cellular structures, which makes the spatial resolving approach troublesome at high active labelling densities. Photoswitchable fluorophores are able to reversibly or irreversibly switch between two or more spectrally distinct states. Several recent techniques, using different fluorescent probes, have been demonstrated with the capability of switching between a fluorescent (on) and a dark (off) state. Molecules within a diffraction-limited region can be activated at different time instances, so that they can be individually imaged and localized, thus enabling spatial distinction.

The same area is imaged multiple times, while individual fluorescence molecules are turned on and off. Parallel to each other, multiple fluorophores are being activated, and localized, subsequently combined to reconstruct a super-resolution image. This principle has been independently conceived and implemented by (F)PALM and STORM [26;46;17;3].

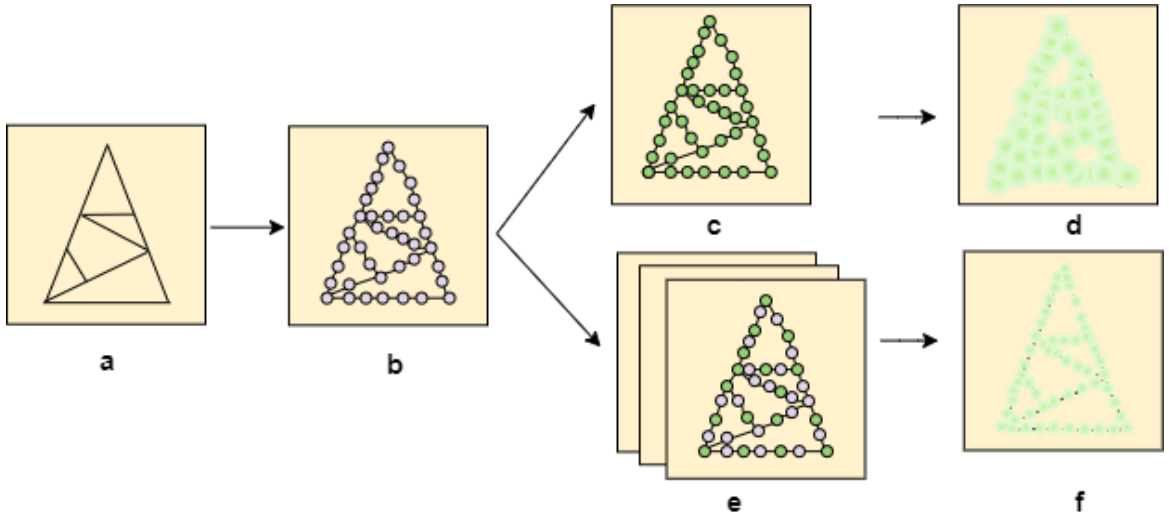

Figure 2-5: A schematic representation of the principle of SMLM - **(a)** The structure to be observed. **(b)** The structure labeled with fluorophores. **(c)** Simultaneous emission of all fluorophores. **(d)** The obtained image by simultaneously putting all fluorophores in their on-state. **(e)** SMLM principle - Capturing multiple frames containing a sparsely activated set of fluorophores. **(f)** The super-resolution image obtained after the acquisition and processing of the localized sparse emitters from all frames.

The (F)PALM and STORM Imaging Methods

Single-molecule based localization microscopy methods such as Photo-activated localization microscopy (PALM) [46], Fluorescence photo-activated localization microscopy (FPALM) [17] and Stochastic optical reconstruction microscopy (STORM) [3] are nowadays the widely used fluorescence microscopic imaging techniques [53]. These techniques are able to obtain super-resolution images beyond the diffraction limit. They all are more or less based on the same principle, but were initially published using different photoswitchable probes. They all make use of photoswitchable fluorescent dyes or proteins, which are being activated by a certain wavelength of light. The approach relies on the randomly switching between activation of individual photoactivable molecules into a fluorescent state (on-state) and a dark state (off-state), which then are being individually imaged resulting in an optically solvable set of activated fluorophores. Due to this stochastic activation characteristic, it provides the ability to distinguish and precisely localize closely packed molecules. Individual fluorescent molecules (in their on-state) are localized then a PSF model is fitted on the estimated location. All the obtained positions of single-molecules are then merged together after a certain amount of photoactivation cycles, resulting in a super-resolution image. It is clear that the resolution improvement is dependent on the degree of precision, by which individual fluorescent molecules can be localized. This is dependent on the number of photons collected, thus single-molecule detection with high accuracy requires a sufficiently high signal-to-noise ratio (S/N).

2-8 Modulation-enhanced Localization Microscopy

Recently, a couple of so-called modulation-enhanced localization microscopy (meLM) techniques have been developed, such as MINFLUX[18] and SIMFLUX[9]. These techniques are based on combing the structured illumination patterns of SIM (or doughnut illumination shapes of STED) and the emitter sparsity characteristic of SMLM with the aim of taking benefit of the advantages of both techniques. The controlled construction and displacement an illumination pattern, instead of uniform illumination, provides extra information since it allows for the measurement of modulation fluorescence intensities coming from isolated emitters. The illumination pattern shifts are typically equidistant in the propagation direction. For 2D localization of single emitters, using two orthogonal illumination patterns is found to be sufficient.

MINFLUX
MINFLUX is considered to be a pioneer in this field of super-resolution microscopy[18]. MINFLUX is able to localize molecules and attain nanoscale precision with minimal emission fluxes, i.e. from the same photon count more information can be extracted. It uses a doughnut-shaped illumination, which is a circular illumination pattern with low or zero intensity in the center, while higher intensities on the boundaries of the beam, as illustrated in Figure 2-4a. The information content of captured photons is increased, since the emission signal carries additional information on the position of the emitter relative to the doughnut-shaped beam, resulting in the localization of the emitters with an increased precision. For instance: when an emitter is close to the center of the doughnut-shaped beam (which is low or zero intensity), it will emit a low photon count. However, if it is further away from the center of the beam, it will emit higher photon counts. For MINFLUX each detected emitter has an uncertainty independent of the wavelength, but given by the probing size L. So by adjusting L below the diffraction limit, the emitted photon becomes more informative. The precision achieved is close to the Cramer-Rao Lower bound (CRLB), indicating the optimal use of photon information. The CRLB for quadratic approximation, at the center of the probe, is given by $\sigma_{CRLB}(0) = \frac{L}{4\sqrt{N}}$. Which means that with a probe size of $L = 50\ nm$ and just merely 100 detected photons a precision of $\approx 2.5\ nm$ is achievable[18]. MINFLUX offers a breakthrough in the field of SMLM, but suffers from a tiny field of view, low throughput and a lack of practical parallelism[9].

SIMFLUX
A practical way to extend the MINFLUX concept to sinusoidal illuminations patterns was suggested by Balzarotti et al.[18], where J. Cnossen, C. Smith et al. acted upon this suggestion and developed SIMFLUX[9]. It is based on the extraction of the molecule's position in a combined estimation from both the relative position with respect to the shifting sinusoidal illumination pattern during all camera frames within the molecule's on-state and from estimated centers of the detected spots on the camera. This makes it able to overcome the limited field-of-view issue of MINFLUX and is compatible with standard widefield imaging on a camera. The isotropic localization precision is given by the CRLB as[9]:

$$\sigma_{x,y} = \frac{\sigma}{\sqrt{N}} \frac{1}{\sqrt{1 + 2\pi^2\sigma^2/\mathsf{p}}}$$

where $\sigma \approx \lambda/4NA$ is the width of the PSF, N the total number of photons collected and p is the pitch of the standing wave illumination pattern, where $\mathsf{p} \approx \lambda/2NA$ is the smallest value. SIMFLUX achieves an improvement over SMLM, in terms of localization precision, with a factor of around 2, depending on the amount of captures photons N and the pattern pitch p in relation to the spot width σ. They also predict that this technique can be used to achieve similar precision to SMLM with up to four times less light needed, which enables faster imaging and the ability of imaging with less bright fluorophores. Also, further advances are envisioned in data processing by precisely modelling the on-off state transitions by the application of for instance hidden Markov-models. Another improvement for SIMFLUX could be achieved by the extension to 3D interference pattern, resulting in an improvement in both lateral and axial localization precision[9].

2-9 The Image Processing Pipeline

In this section, a brief outline of the image processing pipeline is given. A schematic representation is illustrated in Figure 2-6.

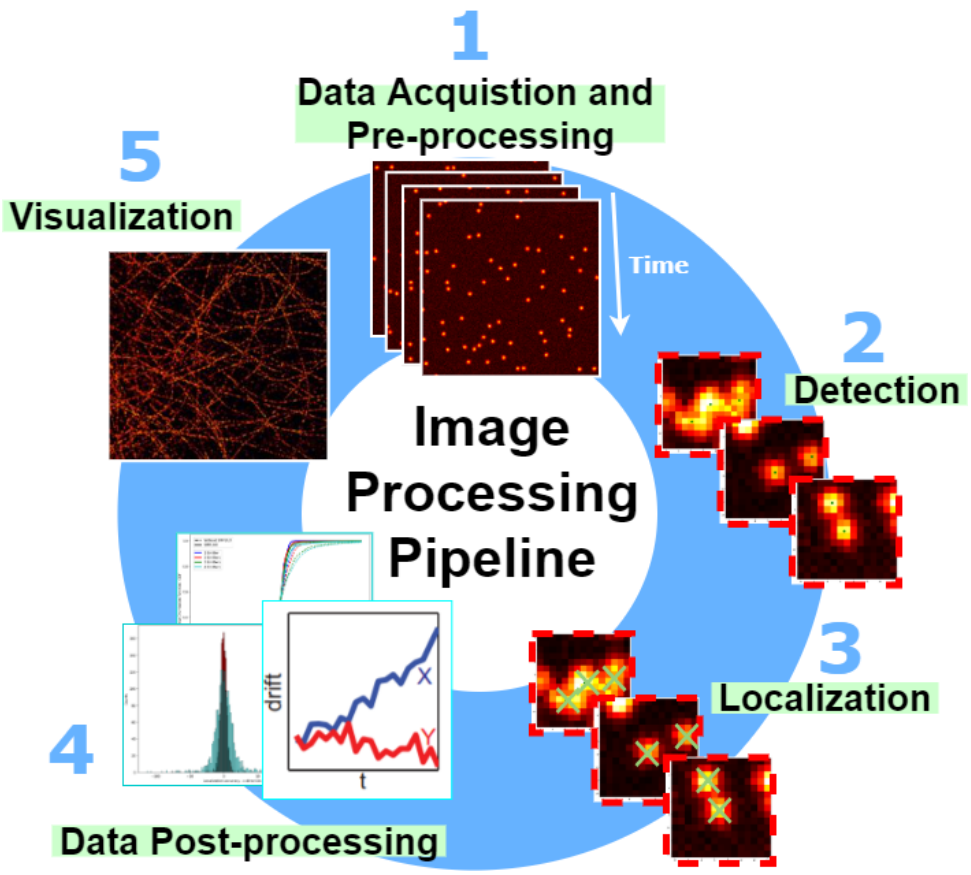

Figure 2-6: Schematic representation of the image-processing pipeline used in single-molecule localization microscopy (SMLM) from raw data to a super-resolution image. **1)** A sequence of diffraction-limited image frames constituted of sparsely distributed emitting fluorophores is acquired. The acquired raw image frames are pre-processed, where among other things the measured intensity values are converted into photon counts. **2)** Regions of interest which contain emitters are detected from each image frame. **3)** The position of the emitter(s) is estimated within each region of interest. **4)** The estimation outcome is checked, corrected and in some cases dismissed. **5)** The reconstructed super-resolution image can be visualized.

1) Data Acquisition and Pre-processing

In the data aquisition step, a sequence of diffraction-limited image frames is acquired, constituted of sparsely distributed emitting fluorophores placed on the structures of interest [32;49]. Selecting the most suitable camera for data collection is of key importance. The two most common types of cameras are: the sCMOS and EMCCD [49]. The key specifications looked at when selecting a camera type for a specific application are: photon sensitivity, readout noise, frame rate and field of view [10]. All acquired images will contain some noise contamination, such as shot noise, readout noise and thermal noise. Shot noise is a result of the random nature of photon emission, even if 100% quantum efficiency is achieved, meaning that every photon is successfully registered as an electronic signal, the number of photons in a given time interval will inherently follow a Poisson distribution [47]. The readout noise emerges during the process of sensor reading. Readout noise is dependent on the readout rate, thus mainly for high readout rates does it really form a limiting factor.

For image pre-processing typically the raw images are offset and gain corrected. An offset is added to avoid negative signals and the signal is usually multiplied by a gain factor in order to convert the electrical signal to photon counts. A major limitation of any photon detector has to do with the randomness of the photon emission. Throughout this work, we assume Poisson distributed data and therefore neglect the read-out noise of the sensor and assume only the shot noise to be present in the recorded images.

2) Detection
In the detection step, the detection of the regions of interests (ROIs) which contain emitters is usually done by thresholding based on a certain pixel intensity relative to the background noise [6]. A maximum filter can be applied, to isolate small regions containing local intensity maxima. to the already pre-processed uniformly filtered images [28]. Another approach for ROIs identification is based on performing a generalized likelihood ratio test (GLRT) in each pixel, whereby the ratio is computed between the likelihoods of the null hypothesis, H_0: the pixel contains only Gaussian noise, and the hypothesis H_1: the pixel also contains a Gaussian peak coming from the emission of a single fluorophore [6;49;32].

3) Localization
Once the regions of interest has been detected, the identified candidates are analyzed to extract the desired physical parameters of the emitters. For the estimation of the position coordinates (θ_x, θ_y) of the fluorophores, the most common approaches are based on CoM computations and algorithms which fit a PSF model to the data with a (weighted) Least-squares (LS) or a Maximum likelihood estimation (MLE) approach [6;28]. Algorithms based on CoM computations, usually require no to low prior information about the shape or size of the PSF, which makes them more robust to any invariances. A drawback of such algorithms is that the underlying imaging model does not take the background fluorescence into consideration, thus in the presence of non-negligible background intensities, they output biased results [49]. MLE algorithms provide optimal results, when accurate noise and imaging models are applied [12]. The main goal is to localize the emitters with a precision higher than the diffraction limit. The localization precision is fundamentally limited by the Cramér-Rao lower bound (CRLB), theoretically the lowest variance possible [37;41] (more details in section 3-3). For a Poisson model, a reasonable analytical approximation for the CRLB is given by [49;6;43]:

$$\sigma_x^2 = \frac{(\sigma^2 + A^2/12)}{N}\Big(1 + 4\tau + \sqrt{\frac{2\tau}{1+4\tau}}\Big)$$

where N is the number of signal photons, A is the pixel area and $\tau = \frac{2\pi\sigma^2\theta_{bg}}{Na^2}$ is the normalized background parameter.

4) Data Post-processing
After the ROI detection and emitter localization, three post-processing operations are commonly performed, typically localization filtering, drift correction and combining multiple localizations [6;49]. At the filtering, non-representative localizations are being dismissed. Non-representative localizations can be caused due to overlapping emissions of multiple fluorophores, or stucking in local minima in the optimization landscape, which we will later talk about in more detail. Combing multiple localiations in cases where fluorophores are visible in multiple consecutive frames (before transitioning into its off-state) their localizations are combined to prevent fluorophore miscounting, avoid false positive localizations and improve recall fraction.

5) Visualisation
Finally at the visualisation step, unlike the conventional fluorescence microscopy techniques, localization microscopy does not sample an image at pixel locations, instead it outputs a set of localized and post-processed emitter coordinates, that represent the estimated fluorophore positions. The obtained super-resolution image can then be visualised.

Chapter 3

Mathematical Concepts and Theoretical Limits

"There are no limitations to the mind except those we acknowledge."
- Napoleon Hill

3-1 Parameter Estimation

In this section, the search for estimators of the true value of the unknown parameters is discussed. The main goal is finding an estimator whose expected value yields to the true value of the unknown parameters, such an estimator is called an unbiased estimator. Suppose that $\hat{\theta}(x)$ is an unbiased estimator of the unknown parameter θ, where X is an independent random variable with a probability density function (PDF) $p(X = x|\theta)$. Unbiased estimators tend to have symmetric PDFs centered at the true value of θ, although symmetry is not a necessity. Mathematically, an estimator is unbiased if and only if:

$$E[\hat{\theta}] = \int \hat{\theta}(x)p(x|\theta)dx = \theta$$

An unbiased estimator does not necessarily mean that it is a good estimator. Preferably, the aim is finding such an unbiased estimator, which exhibits the least variability around the true value, by being as close as possible to the true value most of the time. Such an unbiased estimator, which minimizes the variance for all θ, is referred to as a minimum variance unbiased (MVU) estimator. The mean squared error (MSE), variance and bias of an estimator are defined as:

$$\begin{aligned} Var(\hat{\theta}) &= E[(\hat{\theta} - E[\hat{\theta}])^2] \\ Bias(\hat{\theta}) &= E[\hat{\theta} - \theta] \\ MSE(\hat{\theta}) &= Var(\hat{\theta}) + Bias^2(\hat{\theta}) = E[(\hat{\theta} - \theta)^2] \end{aligned}$$

so when the bias is zero, we get $E[\hat{\theta}] = \theta$ and the MSE and variance become equivalent.

The CRLB (see section 3-3) allows us to determine for any unbiased estimator the smallest variance theoretically achievable. If an estimator exists of which the variance is equal to the CRLB, for each value of θ, then this is an MVU estimator. If no estimator exists, whose variance is equal to the bound, then the MVU estimator is the one with variance closest to the CRLB.

3-2 The Poisson Distribution

Since counting photons is inherently a discrete operation, that can only produce positive integer outcomes, the Poisson distribution function is considered. By the consideration that the intensity (number of photons) n in each pixel follows a Poisson distribution, the probability of observing n photons in the k_{th} pixel is:

$$P(n_k|\mu_k(\theta)) = \frac{\mu_k^{n_k}}{n_k!}e^{-\mu_k} \tag{3-1}$$

where n_k is the observed intensity in the k_{th} pixel. Another fundamental characteristic of the Poisson distribution is that both the expected value and the variance of n_k are equal to μ_k, such that:

$$\mathbb{E}[n_k] = \mathbb{E}[(n_k - \mu_k)^2] = Var_\theta(n_k) = \mu_k$$

3-3 Fisher information and Cramér-Rao Lower Bound

By performing measurements, data samples are obtained, which contain information about the parameters and their underlying probability distributions. How do we know the amount of information a certain sample of data provides about a certain unknown parameter? Such a measure for information is introduced in this section.

We consider an independent random variable X, whose PDF is described by $p(X = x|\theta)$. Generally, if an event has a small probability of occurring, then the occurrence of that specific event does bring much information. The aim is to maximize the amount of information, which can be extracted from X about the estimation of the parameter θ. This can be achieved by maximizing the log-likelihood function of the obtained data $|l'(x|\theta)|$ (or preferably $[l'(x|\theta)]^2$). We define the log-likelihood function as follows:

$$l(x|\theta) = \ln\ p(x|\theta), \qquad l'(x|\theta) = \frac{\partial}{\partial\theta}\ln\Big(p(x|\theta)\Big) = \frac{p'(x|\theta)}{p(x|\theta)}$$

Thus the expected value of $[l'(x|\theta)]^2$, can be taken as a measure of the amount of information provided by the data about the parameter θ. The information in the data x regarding the estimation of the parameter θ is defined as the Fisher information matrix $\mathcal{I}(\theta)$ [37;48;41] (see Appendix A-1):

$$\mathcal{I}(\theta) = \mathbb{E}\left[\left(\frac{\partial l(x|\theta)}{\partial\theta}\right)^2\right] = -\mathbb{E}\left[\frac{\partial^2 l(x|\theta)}{\partial\theta^2}\right] \tag{3-2}$$

The likelihood function, defined as the likelihood of the data n, given the model parameterized by θ, for an image with K pixels, for parameter θ is defined as:

$$\mathcal{L}(n|\mu(\theta)) = \prod_{k=1}^{K} P(n_k|\mu_k(\theta)) \tag{3-3}$$

where $n = \{n_1, n_2, \ldots, n_K\}$ and $\mu = \{\mu_1, \mu_2, \ldots, \mu_K\}$ are the observed and expected intensities, respectively. The log-likelihood is:

$$l(x|\theta) = \sum_{k=1}^{K}\Big(x_k\ln(\mu_k) - \ln(x_k!) - \mu_k\Big)$$

The first and second partial derivatives of the log-likelihood:

$$l'(x|\theta) = \frac{\partial\ l(x|\theta)}{\partial\theta_i} = \sum_{k=1}^{K} \frac{x_k}{\mu_k}\frac{\partial\mu_k}{\partial\theta_i} - \frac{\partial\mu_k}{\partial\theta_i}$$

$$l''(x|\theta) = \frac{\partial^2\ l(x|\theta)}{\partial\theta_i\theta_j} = \sum_{k=1}^{K} \Big(\frac{-x_k}{\mu_k^2}\frac{\partial\mu_k}{\partial\theta_i}\frac{\partial\mu_k}{\partial\theta_j} + \frac{x_k}{\mu_k}\frac{\partial^2\mu_k}{\partial\theta_i\partial\theta_j} - \frac{\partial^2\mu_k}{\partial\theta_i\partial\theta_j}\Big)$$

The Fisher Information matrix can then be computed by calculating the following expectation:

$$\mathcal{I}_{i,j}(\theta) = -\mathbb{E}_\theta[l''(x|\theta)] = \sum_{k=1}^{K} \Big(\underbrace{\mathbb{E}[x_k]}_{=\mu_k}\frac{1}{\mu_k^2}\frac{\partial\mu_k}{\partial\theta_i}\frac{\partial\mu_k}{\partial\theta_j} - \underbrace{\mathbb{E}[x_k]}_{=\mu_k}\frac{1}{\mu_k}\frac{\partial^2\mu_k}{\partial\theta_i\partial\theta_j} + \frac{\partial^2\mu_k}{\partial\theta_i\partial\theta_j}\Big)$$

Hence, the Fisher Information matrix for Poisson distributed measurements is denoted a follows:

$$\mathcal{I}_{i,j}(\theta) = \sum_{k=1}^{K} \frac{1}{\mu_k}\frac{\partial\mu_k}{\partial\theta_i}\frac{\partial\mu_k}{\partial\theta_j} \tag{3-4}$$

while the Fisher Information matrix for Poisson distributed measurements with a sequence of $p = 1, 2, \ldots, \mathcal{P}$ illuminations is denoted a follows:

$$\mathcal{I}_{i,j}(\theta) = \sum_{k=1}^{K}\sum_{p=1}^{\mathcal{P}} \frac{1}{\mu_{k,p}}\frac{\partial\mu_{k,p}}{\partial\theta_i}\frac{\partial\mu_{k,p}}{\partial\theta_j} \tag{3-5}$$

By looking at the covariance around the expected estimate:

$$Var_\theta[l'(X|\theta)] = \mathbb{E}_\theta\big[[l'(X|\theta) - 0][l'(X|\theta) - 0]\big] = \mathbb{E}_\theta\big[[l'(X|\theta)]^2\big]$$

Therefore the definition of the Fisher information matrix can be written as:

$$\mathcal{I}(\theta) = Var_\theta[l'(X|\theta)] \tag{3-6}$$

Theoretically, the best-possible solution for an unbiased parameter estimation problem is by bounded the Cramér-Rao lower bound (CRLB), which is basically the limiting lower bound of the variance for any unbiased parameter estimator. Being able to place such a lower bound on the variance has proven to be extremely useful in practice. It shows us the theoretical impossibility of finding an unbiased estimator, whose variance is less than this bound. Besides, it provides a benchmark against which the performance achieved from any unbiased estimator can be compared.

$$Var(\hat{\theta}) \geq \mathcal{I}(\theta)^{-1}$$

$$\sigma_{\hat{\theta}} \geq \sqrt{\mathcal{I}(\theta)^{-1}}$$

The general expression for the CRLB is given by the inverse of the Fisher information matrix. In case of single emitter, where the parameter vector $\theta = [\theta_x, \theta_y, \theta_I, \theta_{bg}]$ the Fisher information matrix is defined as:

$$\mathcal{I}(\theta) = \sum_{k=1}^{K}\sum_{p=1}^{\mathcal{P}} \frac{1}{\mu_{k,p}} \begin{bmatrix} \frac{\partial^2\mu_{k,p}}{\partial\theta_x^2} & \frac{\partial\mu_{k,p}}{\partial\theta_x}\frac{\partial\mu_{k,p}}{\partial\theta_y} & \frac{\partial\mu_{k,p}}{\partial\theta_x}\frac{\partial\mu_{k,p}}{\partial\theta_I} & \frac{\partial\mu_{k,p}}{\partial\theta_x}\frac{\partial\mu_{k,p}}{\partial\theta_{I_{bg}}} \\ \frac{\partial\mu_{k,p}}{\partial\theta_y}\frac{\partial\mu_{k,p}}{\partial\theta_x} & \frac{\partial^2\mu_{k,p}}{\partial\theta_y^2} & \frac{\partial\mu_{k,p}}{\partial\theta_y}\frac{\partial\mu_{k,p}}{\partial\theta_I} & \frac{\partial\mu_{k,p}}{\partial\theta_y}\frac{\partial\mu_{k,p}}{\partial\theta_{I_{bg}}} \\ \frac{\partial\mu_{k,p}}{\partial\theta_I}\frac{\partial\mu_{k,p}}{\partial\theta_x} & \frac{\partial\mu_{k,p}}{\partial\theta_I}\frac{\partial\mu_{k,p}}{\partial\theta_y} & \frac{\partial^2\mu_{k,p}}{\partial\theta_I^2} & \frac{\partial\mu_{k,p}}{\partial\theta_I}\frac{\partial\mu_{k,p}}{\partial\theta_{I_{bg}}} \\ \frac{\partial\mu_{k,p}}{\partial\theta_{I_{bg}}}\frac{\partial\mu_{k,p}}{\partial\theta_x} & \frac{\partial\mu_{k,p}}{\partial\theta_{I_{bg}}}\frac{\partial\mu_{k,p}}{\partial\theta_y} & \frac{\partial\mu_{k,p}}{\partial\theta_{I_{bg}}}\frac{\partial\mu_{k,p}}{\partial\theta_I} & \frac{\partial^2\mu_{k,p}}{\partial\theta_{bg}^2} \end{bmatrix} \quad \in \mathbb{R}^{4\times4} \tag{3-7}$$

Whereby the estimation precision of each parameter is given by the diagonal terms as follows:

$$\sigma_{\hat{\theta}} = \begin{bmatrix} \sigma_{\theta_x} \\ \sigma_{\theta_y} \\ \sigma_{\theta_I} \\ \sigma_{\theta_{bg}} \end{bmatrix} = \begin{bmatrix} \sqrt{Var_{\theta_x}(\hat{\theta})} \\ \sqrt{Var_{\theta_y}(\hat{\theta})} \\ \sqrt{Var_{\theta_I}(\hat{\theta})} \\ \sqrt{Var_{\theta_{bg}}(\hat{\theta})} \end{bmatrix} = \begin{bmatrix} \sqrt{(\mathcal{I}(\theta)^{-1})_{1,1}} \\ \sqrt{(\mathcal{I}(\theta)^{-1})_{2,2}} \\ \sqrt{(\mathcal{I}(\theta)^{-1})_{3,3}} \\ \sqrt{(\mathcal{I}(\theta)^{-1})_{4,4}} \end{bmatrix}$$

For the multi-emitter case (i.e. $E > 1$), the following set of parameters per ROI is estimated:

$$\theta = [\theta_{bg}, \theta_{x_1}, \theta_{y_1}, \theta_{I_1}, \theta_{x_2}, \theta_{y_2}, \theta_{I_2}, \ldots, \theta_{x_E}, \theta_{y_E}, \theta_{I_E}], \qquad \in \mathbb{R}^T$$

$$\mathcal{I}(\theta) = \sum_{k=1}^{K} \sum_{p=1}^{\mathcal{P}} \frac{1}{\mu_{k,p}} \begin{bmatrix} \frac{\partial^2 \mu_{k,p}}{\partial \theta_{bg}} & \frac{\partial \mu_{k,p}}{\partial \theta_{bg}} \frac{\partial \mu_{k,p}}{\partial \theta_{x_1}} & \cdots & \cdots & & & \cdots & \frac{\partial \mu_{k,p}}{\partial \theta_{bg}} \frac{\partial \mu_{k,p}}{\partial \theta_{x_E}} \\ \frac{\partial \mu_{k,p}}{\partial \theta_{x_1}} \frac{\partial \mu_{k,p}}{\partial \theta_{bg}} & \frac{\partial^2 \mu_{k,p}}{\partial \theta_{x_1}} & \ddots & & & & & \vdots \\ \vdots & \vdots & \frac{\partial^2 \mu_{k,p}}{\partial \theta_{y_1}} & \ddots & & & & \vdots \\ \vdots & & \ddots & \frac{\partial^2 \mu_{k,p}}{\partial \theta_{I_1}} & & & & \vdots \\ \vdots & & & \ddots & \ddots & & & \vdots \\ \vdots & & & & \cdots & \frac{\partial \mu_{k,p}}{\partial^2 \theta_{x_E}} & \cdots & \vdots \\ \vdots & & & & & \cdots & \frac{\partial \mu_{k,p}}{\partial^2 \theta_{y_E}} & \frac{\partial \mu_{k,p}}{\partial \theta_{y_E}} \frac{\partial \mu_{k,p}}{\partial \theta_{I_E}} \\ \frac{\partial \mu_{k,p}}{\partial \theta_{I_E}} \frac{\partial \mu_{k,p}}{\partial \theta_{bg}} & \cdots & & & \cdots & \cdots & \frac{\partial \mu_{k,p}}{\partial \theta_{I_E}} \frac{\partial \mu_{k,p}}{\partial \theta_{y_E}} & \frac{\partial^2 \mu_{k,p}}{\partial \theta_{I_E}} \end{bmatrix} \in \mathbb{R}^{T \times T} \tag{3-8}$$

Whereby $T = 3E + 1$, for E being the number of emitters. However, for the multi-emitter case the Fisher information matrix can become singular due the occurrence of $\{\theta_{x_i}, \theta_{x_i}\} = \{\theta_{x_j}, \theta_{y_j}\}$. Near this singular point, the Fisher Information matrix can not be used to correctly determine the theoretical estimator precision, CRLB. For this reason we used the pseudo-inverse of the Fisher matrix to determine the CRLB [51]:

$$Var(\hat{\theta}) \geq \mathcal{I}^{\dagger}(\theta)$$

whereby † denoted the psuedo-inverse, which is defines as:

$$\mathcal{I}^{\dagger}(\theta) = (\mathcal{I}^{\top}\mathcal{I})^{-1}\mathcal{I}^{\top}$$

hence the precision becomes:

$$\sigma_{\hat{\theta}} \geq \sqrt{(\mathcal{I}^{\top}\mathcal{I})^{-1}\mathcal{I}^{\top}} \tag{3-9}$$

3-4 Maximum Likelihood Estimation

The maximum likelihood estimation (MLE) method is considered to be one of the most powerful statistically based methods for parameter estimation. Perhaps to some, the Least-squares (LS) approach may sound more familiar, however several comparison studies have shown that the maximum likelihood method generally provides more accurate estimation results[8], compared to other parameter estimation methods like the LS approach. The outcome of MLE, is defined to be the value of parameter vector θ that maximizes the probability of observing data n, i.e. the value that maximizes the likelihood function. The parameter values $\hat{\theta}$ are found such that they maximize the likelihood of the process described by the model, produced the data that were actually observed. The MLE is known to be asymptotically unbiased and efficient. When the PDF of the data $p(n|\theta)$ satisfies some regularity conditions (Appendix $7B$ of[37]), then the MLE of the unknown parameter θ is asymptotically normally distributed according to:

$$\hat{\theta}_{MLE} \sim \mathcal{N}(\theta^*, \mathcal{I}^{-1}(\theta))$$

with the mean being the true parameter value θ^* and it attains the CRLB as covariance matrix $(\mathcal{I}^{-1}(\theta))$. The likelihood function, for an image with K pixels, for parameter θ is defined as:

$$\mathcal{L}(n|\mu(\theta)) = \prod_{k=1}^{K} P(n_k|\mu_k(\theta)) \tag{3-10}$$

where $n = \{n_1, n_2, \ldots, n_K\}$ and $\mu = \{\mu_1, \mu_2, \ldots, \mu_K\}$ are the observed and expected intensities, respectively. The above expression can get quite complex when differentiating, therefore usually it is simplified by taking the (natural) logarithm of the expression, since the logarithm of a product is equal to the sum of the individual logarithms ($log(a \cdot b) = log(a) + log(b)$). Due to the fact that, logarithms are monotonically increasing functions, meaning that if the value on the x-axis increases the corresponding value on the y-axis also increases, this manipulation can be performed. After maximization, the obtained $\hat{\theta}$ that maximizes the manipulated function, is the same $\hat{\theta}$ that maximizes the original function[38]. Therefore we prefer working with the simpler log-likelihood function. To ease the computations further, it is common to normalize the likelihood function by dividing by the maximum possible likelihood $\mathcal{L}(n|n)$ (i.e. when $\mu_k = n_k$) and minimize twice the negative logarithm of this ratio in order to change the repeated products into sums. The obtained function to be minimized is then defined as:

$$\begin{aligned}
\mathcal{F}(\theta) &= -2 \ln \Big[\frac{\mathcal{L}(n|\mu(\theta))}{\mathcal{L}(n|n)} \Big] \\
&= -2 \ln \Big[\frac{\prod_{k=1}^{K} P(n_k|\mu_k(\theta))}{\prod_{k=1}^{K} P(n_k|n_k)} \Big] \\
&= -2 \Big(\sum_{k=1}^{K} \ln \left(P(n_k|\mu_k(\theta)) \right) - \sum_{k=1}^{K} \ln \left(P(n_k|n_k(\theta)) \right) \Big) \\
&= -2 \sum_{k=1}^{K} \Big(n_k \ln(\mu_k(\theta)) - \underbrace{\ln(n_k!)}_{=c} - \mu_k(\theta) - (n_k \ln(n_k) - \underbrace{\ln(n_k!)}_{=c} - n_k) \Big)
\end{aligned}$$

$$\mathcal{F}(\theta) = 2 \sum_{k=1}^{K} (\mu_k(\theta) - n_k) - 2 \sum_{\substack{k=1 \\ n_k \neq 0}}^{K} n_k \ln \big(\frac{\mu_k(\theta)}{n_k} \big) \tag{3-11}$$

Minimizing $\mathcal{F}(\theta)$, which is equivalent to the maximization of the likelihood, gives the best estimate for the parameters θ.

$$\hat{\theta}_{MLE} = arg \max_{\theta \in \Theta} \mathcal{L}(n|\mu(\theta)) = \arg \min_{\theta \in \Theta} 2 \sum_{k=1}^{K} (\mu_k(\theta) - n_k) - 2 \sum_{\substack{k=1 \\ n_k \neq 0}}^{K} n_k \ln \big(\frac{\mu_k(\theta)}{n_k} \big) \tag{3-12}$$

3-5 The Chi-Squared $\mathcal{X}^2$-Test

After finding the most suitable algorithm for parameter estimation, we still have to decide at what point the estimate is good enough. The Chi-squared test ($\mathcal{X}^2$-test) is used to determine whether there is a statistically significant difference between the expected and the observed model. This is can happen for instance when the optimization algorithm stucks in a local minimum, which does not satisfy the $\mathcal{X}^2$-test. The $\mathcal{X}^2$-test is defined as:

$$\mathcal{X}^2 = \sum_{k=1}^{K} \frac{(n_k - \mu_k)^2}{\mu_k} \tag{3-13}$$

where n_k and μ_k represent the observed and expected photon count in a given pixel, respectively. For the ROIs where there is a significant difference between the observed image and the theoretical model, different procedures are taken. If the measured values are produced by a Poisson process, the expected value and standard deviation for the $\mathcal{X}^2$ value are given by:

$$E[\mathcal{X}^2] = K$$
$$\sigma[\mathcal{X}^2] = \sqrt{2K + \sum_{k=1}^{K} \frac{1}{\mu_k}}$$

The critical value set to express the level of confidence (95%) we have in the observed with respect to the expected value is:

$$\mathcal{X}^2_{threshold} = K + 2\sqrt{2K + \sum_{k=1}^{K} \frac{1}{\mu_k}} \tag{3-14}$$

3-6 Image Formation Model

SIMFLUX

As mentioned in section 2-8, SIMFLUX makes use of three phase shifts and two orientations, which makes it a total of six illumination patterns captured by six frames. However for generalizing purposes the total number of shifted illumination patterns is denoted as $\mathcal{P}$ (i.e. $\mathcal{P} = 6$).

The sequence $p = \{1, 2, \ldots, \mathcal{P}\}$ illumination patterns, with the intensity profile $P(\phi)$ as a function of pattern phase ϕ, which is displaced according to phase offsets ψ_p such that:

$$\sum_{p=1}^{\mathcal{P}} P_p(\phi_p(\bar{r})) = 1$$

whereby,

Coordination vector: $\bar{r} := (x, y) \quad x, y \in [b, K - b]$

With K being the number of pixels, b border size in pixels (typically 2)

Phase: $\phi_p(\bar{r}) = 2\pi\bar{q}_p \cdot \bar{r} - \psi_p$

Phase offset:

$$\psi_p = \frac{1}{\frac{1}{2}}\frac{2\pi(p-1)}{\mathcal{P}} = [0, \frac{2\pi}{3}, \frac{4\pi}{3}, 2\pi, \frac{8\pi}{3}, \frac{10\pi}{3}], \quad for\ p = \{1, 2, \ldots, 6\}$$
$$= [\underbrace{0, \frac{2\pi}{3}, \frac{4\pi}{3}}_{x\ offset}, \underbrace{0, \frac{2\pi}{3}, \frac{4\pi}{3}}_{y\ offset}]$$

whereby the first- and last three elements of ψ_p represent the sequential phase offset in the x- and y orientation, respectively.

Spatial frequency vector:

$$\bar{q} = (q_{p,x}, q_{p,y}) = \frac{1}{\mathsf{p}}(\cos\beta_p, \sin\beta_p)$$

where p is the pitch and $\beta_x = \pi + \beta_0$, $\beta_y = \frac{\pi}{2} + \beta_0$, with β_0 being the global angular offset.
For conceptual simplicity and computational efficiency, the PSF can be approximated sufficiently well by a simplified form with a 2D Gaussian:

$$PSF(x,y) = \frac{1}{2\pi\sigma^2}e^{-\frac{(x-\theta_x)^2+(y-\theta_y)^2}{2\sigma^2}} \quad \Rightarrow \quad h(\bar{r}) = \frac{1}{2\pi\sigma^2}e^{-\frac{(\bar{r}-r^\circ)^2)}{2\sigma^2}} \tag{3-15}$$

with $r^\circ = [x^\circ, y^\circ]$ being the emitter position vector and for simplicity we denote: $\tilde{r} = \bar{r} - r^\circ$.
The integration of the PSF over the pixel area A_k results:

$$E(\tilde{r}) = \iint_{x,y\in A_k} h(\tilde{r})dxdy$$

The expected photon count in the k_{th} pixel is denoted as:

$$\mu_{k,p} = \sum_{e=1}^{E} \theta_{I_e} P_p(\phi_p(r^\circ))E_{k,e}(\tilde{r}) + \frac{\theta_{bg}}{\mathcal{P}}, \tag{3-16}$$

the background intensity θ_{bg} is assumed to be uniformly distributed over the ROI and temporally independent, so approximately constant from frame-to-frame.

$$E_{k,e}(\tilde{r}) = E_{x_{k,e}}(u)E_{y_{k,e}}(v)$$
$$E_{x_{k,e}}(u) = \frac{1}{2}\Big(erf(\frac{u+\frac{\Delta x}{2}}{\sqrt{2}\sigma}) - erf(\frac{u-\frac{\Delta x}{2}}{\sqrt{2}\sigma})\Big), \qquad E_{y_{k,e}}(v) = \frac{1}{2}\Big(erf(\frac{v+\frac{\Delta_y}{2}}{\sqrt{2}\sigma}) - erf(\frac{v-\frac{\Delta y}{2}}{\sqrt{2}\sigma})\Big)$$

For SIMFLUX a sinusoidal illumination pattern is considered [9]:

$$P(\phi) = \frac{1}{\mathcal{P}}(1 + m\cos\phi) \tag{3-17}$$

with m being the modulation depth. In case of achieving perfect modulation ($m = 1$), we find:

$$P(\phi) = \frac{1}{\mathcal{P}}(1 + \cos\phi) = \frac{2}{\mathcal{P}}\cos(\frac{\phi}{2})^2$$

The different illumination patterns are divided into equidistant phases. By taking into account that the modulation depth and the intensity of the illumination patterns can vary with direction of the illumination patterns:

$$P_p(\phi) = \frac{1}{\mathcal{P}}(1 + m_p\cos\phi)$$

Hence, the expected photon count on the k_{th} pixel is denoted as:

$$\mu_{k,p} = \sum_{e=1}^{E} \theta_{I_e} P_p(\phi_p(r^\circ))E_{k,e}(\tilde{r}) + \eta_p\theta_{bg}, \tag{3-18}$$

where η_p represents the normalized relative intensity factor, such that $\sum_{p=1}^{\mathcal{P}} \eta_p = 1$, nominally $\eta_p = \frac{1}{\mathcal{P}}$

Structured Illumination Microscopy - SIM

In this section, the image formation procedure in SIM is shortly clarified, subsequently in Chapter 4 expanded further for SMLM applications. Making use of structured illumination results in modulation of the spatial frequencies of sample details, making normally unobservable frequencies accessible by down-modulation into conventionally observable space. Displaced information can be computationally identified and restored to the proper place in the image space. By applying the Fourier transform to the microscope's PSF the characteric OTF of the optical system is obtained. To refresh it briefly, the Fourier transform inherently performs a mapping operation from the real space to the frequency space, such that a signal is described by a series of frequencies with respective amplitudes and phases. The Forward- and Inverse Fourier transform are depicted below as FFT and IFT respectively:

$$\text{FFT:} \quad F(k) = \int_{-\infty}^{\infty} f(x) e^{-2\pi k x i} dx, \qquad \text{IFT:} \quad f(x) = \int_{-\infty}^{\infty} F(k) e^{2\pi k x i} dk$$

With increasing spatial frequencies, the amplitude of the OTF decreases, until it reaches zero, which is typically referred to as the cut-off frequency. Finer structures, thus higher spatial frequencies, become unobservable. This can be compared with the case of two emitters with a separation distance smaller than the diffraction limit, where the fact whether the observed intensity is coming from one or two emitters can not be decided. The Moiré effect occurs when two relatively high frequency patterns are similar in structure but slightly shifted or displaced with respect to each other (see Figure 2-4b). Resulting in the creation of a third pattern with lower frequency, which changes as the relative position of the two patterns change. A typically used illumination pattern is a sinusoidal structured illumination pattern, $P_p = \frac{1}{2}(1 + \cos(2\pi k_s r + \phi_p))$. Suppose that the structured illumination pattern has a frequency of k_s, then when it passes over the specimen structures with frequency k, Moiré patterns are created at $k \pm k_s$. By constructing the illumination patterns such that, $k \pm k_s < k_0$, where k_0 is the magnitude of the maximum observable spatial frequency, spatial frequencies beyond the cut-off frequency become accessible. To maximize the performance of SIM, the frequency of the illumination patterns should be made as close as possible to k_0 in order to achieve the theoretical limit of $2k_0$. The OTF in the lateral direction is typically depicted as a circle as illustrated in Figure 3-1 (a), whereby low-frequency information lies closer to the center and towards the periphery of the circle the frequency increases. Under appropriate assumptions, the system can be assumed to be shift-invariant, such that the convolution, $Image = Specimen \circledast PSF$, which describes the blurring effect, can be described by:

$$g(x,y) = f(x,y) \circledast PSF(x,y), \qquad whereby \quad f(x,y) = P(x,y)O(x,y)$$

with $f(x,y)$ being the captured fluorescence signal (the modulated object), and where $O(x,y)$ denotes the imaged object and $P(x,y)$ the illumination pattern. By applying the Fourier transform:

$$g(x,y) = f(x,y) \circledast PSF(x,y) = P(x,y)O(x,y) \circledast PSF(x,y) \xrightarrow{\mathscr{F}} \tilde{G}(k) = \tilde{P}(k) \circledast \tilde{O}(k)OTF(k)$$

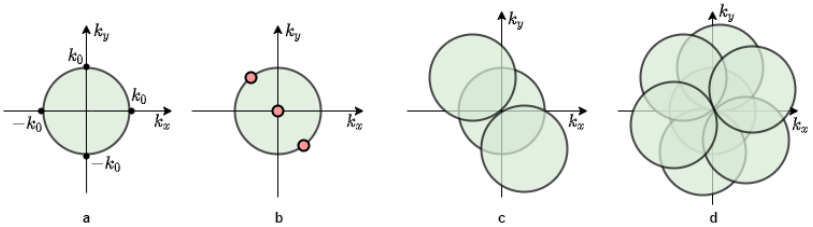

Figure 3-1: The principle of the resolution improvement obtained by SIM. **(a)** The OTF support region. The magnitude of the finest observable frequency, along the edge of the support region, is denoted by $k_0 \approx \frac{2NA}{\lambda}$. **(b)** Structured illumination of frequency k_0 results in the creation of harmonics at $\pm k_0$, denoted by the three red points. **(c)** Extended OTF support regions are created centered at these points. **(d)** The illumination is rotated in different orientations to expand the OTF support region with approximately twice the diameter, resulting in an improvement factor of two.

Chapter 4

Manuscript

In this chapter, the main findings of my thesis are presented and discussed in the form of a paper-draft. Furthermore, there are some references for supplementary notes and figures for more in-depth clarifications and observations.

"At the end of the day, you can't control the results;
you can only control your effort level and your focus."
- Ben Zobrist

Modulation enhanced multi-emitter fitting for high active density localization microscopy

Multi-emitter fitting with structured illumination patterns for high active imaging density super-resolution localization microscopy

AHMED ZAHRAN[1], JELMER CNOSSEN[1,2] AND CARLAS S. SMITH [1,2,3]

[1] *Delft Center for Systems and Control, Delft University of Technology, Delft, The Netherlands*
[2] *Department of Imaging Physics, Delft University of Technology, Delft, The Netherlands*
[3] *Department of Engineering Science, University of Oxford, Oxford, United Kingdom*
[*] *opex@osa.org*

Abstract: Single-molecule localization microscopy (SMLM) methods achieve spatial resolution beyond the diffraction limit through sequential activation and localization of individual active fluorophores. However, the analysis of conventional SMLM methods requires sparse activation to minimize overlap between active fluorophores. Recently, several multi-emitter methods have been developed which are able to analyze higher density data, while allowing partial overlap between emitters. Here, we propose a, maximum likelihood-based, modulation enhanced SMLM method able to localize multiple active emitters within a single region of interest (ROI). The algorithm is designed to provide high recall rates for high active imaging density, while minimizing localization precision deterioration. The performance of the algorithm has been evaluated and validated under a wide range of realistic imaging conditions. As theoretically expected, our approach significantly outperforms conventional $2D$-Gaussian SMLM with a twofold improvement factor in terms of localization precision for various acive emitter densities and intensities. At higher active emitter imaging densities, the extension from single to multi-emitter showed a clear improvement in recall fraction.

1. Introduction

Super-resolution imaging techniques, such as stimulated emission depletion (STED)[1;2], (saturated) structured illumination microscopy ((S)SIM)[3;4;5], (fluorescence) photo-activated localization microscopy ((F)PALM)[6;7], and stochastic optical reconstruction microscopy (STORM)[6;8;9] have revolutionized fluorescence light microscopy. The observation of, previously limited and unclear, cellular structures has demonstrated the great promise of super-resolution fluorescence microscopy in the perception of biological processes at the cellular level. It has enabled the study of cellular structure details and dynamics. The methods STED and SIM make use of patterned illumination to increase the localization precision. The PALM and STORM techniques, often referred to as single-molecule localization microscopy (SMLM) methods, are currently one of the broadly used super-resolution imaging techniques. Inherently, SMLM is based on acquiring a large number of diffraction-limited images consisting of sparsely distributed emitting fluorophores, whereby just a small fraction of emitters are put into their active state to prevent fluorescence emissions of individual fluorophores to overlap. This limitation on the number of active fluorophores in a given frame, surely does affect the acquisition time negatively. Next, precise and accurate estimates of the spatial coordinates of the fluorophores, placed on the structures of interest, are made with a precision exceeding the diffraction limit. A super-resolution image is then reconstructed from these localizations. Since only imaging frames with well-isolated non-overlapping emitters are considered in the analysis, a lot of data is being rejected.

One of the most crucial questions in SMLM applications concerns the precision with which the position of a single molecule can be determined. The Cramér–Rao lower bound (CRLB) is used to quantify the estimation performance in terms of localization precision. Recently, several modulation enhanced localization microscopy (meLM) methods have shown resolution improvement by combining patterned illumination with SMLM techniques, such as MINFLUX[10] and SIMFLUX[11]. The challenging part is that the analysis of images by these methods requires sparse activation regions to prevent overlap between active emitters. During spot identification, the conventional and the extended (with illumination patterns) SMLM algorithms quickly lose both their precision and accuracy, when too many emitters are concurrently active in the imaging frame. Several, localization fitting techniques have been developed aiming for exploiting all available fluorescence data, consequently leading to resolution improvement at high molecular densities and the ability of resolving overlapping emitters, while minimizing the computational effort, e.g. 3B[12], FALCON[13], BAMF[14] and MFA[15].

Here, we propose a modulation enhanced single-molecule localization microscopy maximum likelihood-based method, which is an extension of the current SIMFLUX[11] approach, able to localize multiple emitters simultaneously within a single region of interest (ROI). The mathematical framework of the algorithm is comprehensively built up throughout this work and the expected theoretical improvement is elucidated and validated with realistic simulations. We refer to the novel multi-emitter modulation enhanced method as Multi-SIMFLUX (and just SIMFLUX interchangeably).

The remainder of this manuscript is structured as follows. In Section 2, the considered image formation model is presented, the theoretical limit is described and the algorithm setup is explicated. Then in Section 3, the expected theoretical improvement factor of SIMFLUX over SMLM is derived and the numerical performance evaluation results are shown and briefly commented. We evaluate the theoretical and numerical performance of the Multi-SIMFLUX algorithm against single-SIMFLUX and standard 2D-Gaussian SMLM (single and multi approach) on simulated data. To asses the performance of SIMFLUX, several simulations were performed under a wide range ofrealistic imaging conditions. This involves various active-emitter densities, different emitter- and background intensities, numerous emitter configurations, a multitude of ROI-sizes and point spread function widths. for different active emitter densities and various emitter and background intensities. Lastly in Section 4, the main obtained results from the manuscript are emphasized and discussed.

2. Methods

2.1. Image Formation Model

The point spread function (PSF) describes the impulse response of a microscope to a point source of light. In the absence of aberrations, for conceptual simplicity and computational efficiency, the PSF can be approximated sufficiently well by a $2D$ Gaussian[16;17] centered at the emitter's position:

$$PSF(x,y) = \frac{1}{2\pi\sigma^2} e^{-\frac{(x-\theta_x)^2+(y-\theta_y)^2}{2\sigma^2}} \tag{1}$$

where σ denotes the standard deviation of the 2D Gaussian PSF and (θ_x, θ_y) the emitter position in the x and y direction, respectively. As in SIMFLUX[11], we consider standing wave intensity patterns with three controllable spatial phase shifts in two orthogonal orientations, which makes it a total of six illumination patterns captured by six frames. For generalizing purposes, the total number of illumination patterns is denoted as $\mathcal{P}$. The sequence $p = 1, 2, \ldots, \mathcal{P}$ illumination patterns, with the intensity profile $P(\phi)$ as a function of pattern phase ϕ, displaced according to phase offsets ψ_p such that:

$$\sum_{p=1}^{\mathcal{P}} P_p(\phi_p(x,y)) = 1, \qquad 0 \le P_p(x,y) \le 1, \quad \forall p \in \{1, 2, \ldots, \mathcal{P}\} \tag{2}$$

The different illumination per orientation patterns are divided into equidistant phases. By taking into account that the modulation depth (m) and the intensity of the illumination patterns can vary with direction of the illumination patterns, we obtain the following:

$$P_p(\phi_p(x,y)) = \frac{1}{\mathcal{P}}(1 + m_p \cos\phi_p)$$

$$P_p(\phi_p(x,y)) = \begin{cases} \frac{1}{\mathcal{P}}(1 + m_p \cos(q_{p,x} - \psi_p)) & \text{for } p \le \frac{\mathcal{P}}{2} \\ \frac{1}{\mathcal{P}}(1 + m_p \cos(q_{p,y} - \psi_p)) & \text{for } p > \frac{\mathcal{P}}{2} \end{cases}$$

$$\text{Spatial frequency vector:} \qquad (q_{p,x}, q_{p,y}) = \frac{1}{\mathsf{p}}(\cos\beta_x, \sin\beta_y)$$

where $\beta_x = \pi + \beta_0$, $\beta_y = \frac{\pi}{2} + \beta_0$, with β_0 being the global angular offset and p is the pitch.

The phase offset in both directions: $\psi_p = [\underbrace{0, \frac{2\pi}{3}, \frac{4\pi}{3}}_{x\text{-offset}}, \underbrace{0, \frac{2\pi}{3}, \frac{4\pi}{3}}_{y\text{-offset}}], \qquad for \;\; p = 1, 2, \ldots, \mathcal{P}$

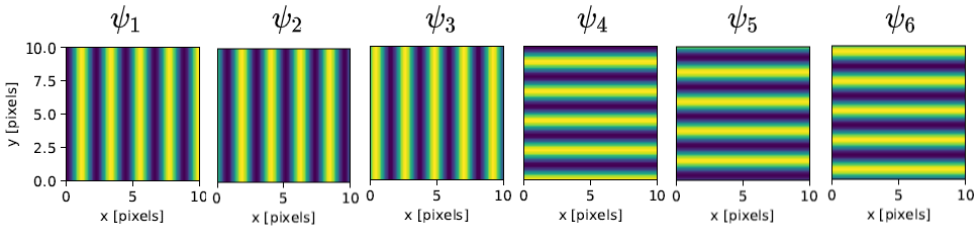

Figure 1. Standing wave illumination is used in two orthogonal orientations (x,y) with three equidistant phase shifts between 0 and 2π, captured by a total of six frames.

Throughout this work, we neglect sensor read-out noise and assume only shot noise to be present in the recorded images, i.e. Poisson distributed data. The expected photon count, in the k_{th} pixel for the p_{th} frame from all existing emitters E, can hence be written in the following compact notation (a detailed derivation of this model is included in Supplementary Note B):

$$\mu_{k,p}(u,v) = P_p(\theta_x, \theta_y, \phi_p) \sum_{e=1}^{E} \theta_{I_e} E_{x_{k,e}}(u) E_{y_{k,e}}(v) + \eta_p \theta_{bg} \tag{3}$$

with the parameter θ_{I_e} being the total photon count expected from the e_{th} emitter, θ_{bg} is the background intensity in $photons/pixel$ and where $u = x - \theta_x$ and $v = y - \theta_y$. Further, η_p represents the normalized relative intensity factor, such that $\sum_{p=1}^{\mathcal{P}} \eta_p = 1$, nominally $\eta_p = \frac{1}{\mathcal{P}}$. The explicit expressions for $E_{x_{k,e}}(u)$ and $E_{y_{k,e}}(v)$ are denoted as:

$$E_{x_{k,e}}(u) = \frac{1}{2}\Big(erf(\frac{u + \frac{\Delta_x}{2}}{\sqrt{2}\sigma}) - erf(\frac{u - \frac{\Delta_x}{2}}{\sqrt{2}\sigma})\Big), \qquad E_{y_{k,e}}(v) = \frac{1}{2}\Big(erf(\frac{v + \frac{\Delta_y}{2}}{\sqrt{2}\sigma}) - erf(\frac{v - \frac{\Delta_y}{2}}{\sqrt{2}\sigma})\Big)$$

where Δ_x and Δ_y are the pixel sizes in the x and y direction, respectively. Furthermore, the detector grid is assumed to have no dead space between the pixels.

2.2. Theoretical Precision Limit

In order to give an representative photon count model description, the parameters θ_{x_e}, θ_{y_e}, θ_{I_e} per emitter and θ_{bg} for the total considered pixel area have to be accurately estimated. The aim is to maximize the amount of information that can be extracted from the data x about the estimation of the parameter θ. This can be achieved by maximizing the log-likelihood function of the obtained data $|l'(x|\theta)|$ (or equivalently $l'(x|\theta)^2$). The likelihood function, for an image with K pixels and parameter vector θ is defined as:

$$\mathcal{L}(n|\mu(\theta)) = \prod_{k=1}^{K} P(n_k|\mu_k(\theta)) \tag{4}$$

and the log-likelihood:

$$l(x|\theta) = \sum_{k=1}^{K} \Big(x_k \ln(\mu_k) - \ln(x_k!) - \mu_k\Big)$$

where $n = \{n_1, n_2, \ldots, n_K\}$ and $\mu = \{\mu_1, \mu_2, \ldots, \mu_K\}$ are the observed and expected intensities, respectively. The information in the data regarding the estimation of the parameter vector θ can be quantified by the Fisher information matrix $\mathcal{I}(\theta)$ [16;18;19]:

$$\mathcal{I}(\theta) = \mathbb{E}\left[\left(\frac{\partial l(x|\theta)}{\partial \theta}\right)^2\right] = -\mathbb{E}\left[\frac{\partial^2 l(x|\theta)}{\partial \theta^2}\right] \tag{5}$$

Theoretically, the best-possible solution for an unbiased parameter estimation problem is bounded by the Cramér-Rao lower bound (CRLB), which is basically the limiting lower bound of the variance for any unbiased parameter estimator. Being able to place such a lower bound on the variance has proven to be extremely useful, since it shows us the theoretical impossibility of finding an unbiased estimator, whose variance is less than this bound. Besides, it provides a benchmark against which the performance achieved by unbiased estimator can be compared.

The Fisher information per element is denoted as (for more details see Supplementary Note B.2):

$$\mathcal{I}_{i,j}(\theta) = \sum_{k=1}^{K} \sum_{p=1}^{\mathcal{P}} \frac{1}{\mu_{k,p}} \frac{\partial \mu_{k,p}}{\partial \theta_i} \frac{\partial \mu_{k,p}}{\partial \theta_j}, \qquad \forall\, i, j \in \{1, \ldots, T\} \tag{6}$$

whereby $T = 3E + 1$, for E being the number of emitters. However, for the multi-emitter case ($E > 1$) the Fisher information matrix can become singular due the occurrence of $\{\theta_{x_i}, \theta_{y_i}\} = \{\theta_{x_j}, \theta_{y_j}\}$ [15]. Near this singular point, the Fisher Information matrix can not be used to correctly determine the theoretical estimator precision, CRLB [20]. For this reason we consider the pseudo-inverse [21]:

$$Var(\hat{\theta}) \geq \mathcal{I}^{\dagger}(\theta)$$

whereby † denoted the pseudo-inverse, which is defines as:

$$\mathcal{I}^{\dagger}(\theta) = (\mathcal{I}^{\top}\mathcal{I})^{-1}\mathcal{I}^{\top}$$

hence the theoretical precision limit becomes:

$$\sigma_{\hat{\theta}} \geq \sqrt{(\mathcal{I}^{\top}\mathcal{I})^{-1}\mathcal{I}^{\top}} \tag{7}$$

2.3. Algorithm Setup

Performing the 2D localization (x, y), emitter- and background intensity estimation can be formulated as a numerical optimization problem. Whereby we explore the multi-emitter parameter space, i.e. $\theta \in \mathbb{R}^T$, for the optimal parameters which minimize the objective function. There are many algorithms available for solving numerical optimization problems. In this work, for the numerical implementation of the Maximum likelihood estimation (MLE) problem for the estimation of the parameter vector θ, the Levenberg-Marquardt (LM) algorithm is considered. The LM algorithm is a commonly used algorithm in localization microscopy [22], which is based on varying between two minimization methods: the gradient descent and the Gauss-Newton method [23]. In the gradient descent method, the sum of the squared errors is reduced by updating the parameter vector θ in the steepest-descent direction. The Gauss-Newton method is based on a local quadratic approximation of the objective function. The LM method acts more like a gradient-descent method when the parameters are far from their optimal value, and acts more like the Gauss-Newton method when the parameters are close to their optimal value. A schematic representation of the steps performed during the multi-emitter algorithm is displayed in Supplementary Figure A.3.

Generally, for nonlinear non-convex minimization problems, as it is the case for our algorithm, there are many local minima and not every local minimum will be the global minimum. A local minimum is also the global minimum, if it is the only minimum in the optimization landscape or there are many local minima all having the same depth. Therefore, in practice we cannot be sure that the obtained solution is indeed the global minimum, i.e. provides the best localization. It is generally known that the problem of finding the global minimum is a computationally hard problem, in the sense that trying to obtain the exact global optimum may require an excessive amount of computational effort. Therefore, in practice methods are used that, although convergence to the global optimum cannot be guaranteed, will yield "good" satisfying results.

- **Pre-Processing and Detection - ROI extraction**
  This pre-processing and detection procedure is adopted from the MFA approach[15].

$$\textbf{1)} \quad F_1 = uniform[I, S_{F_1}] - uniform[I, 2 \times S_{F_1}]$$

  First, the images are offset and gain corrected to convert pixel intensity values to photon counts. Then, to reduce Poisson shot noise and minimize the influence of background on the identification of potential emitter locations, some filters are applied. The first filtering step is calculated from the original image I as follows: where $uniform[I, S_F]$ represents a uniform filtering process with a square kernel size $S_F \times S_F$ performed on the image I. This filter acts as a smoothing filter, by reassigning the value of each pixel with the average kernel pixel value. The analysis is not strongly dependent on the smoothing filter, the uniform filter is mainly chosen for speed[15]. The second filtering step, performed on the first filtered image F_1, is a maximum filtering process used to obtain local maximum values in order to make a distinction between random background noises and real fluorophore emissions as follows:

$$\textbf{2)} \quad F_2 = max[F_1, S_{F_2}]$$

  wereby the size of the square kernels are chosen to be:

$$S_{F_1} = 2\sigma_{PSF} + 1, \qquad S_{F_2} = 5\sigma_{PSF}$$

  Next, a pixel-wise comparison is performed to identify the center pixels of regions of interest:

$$\textbf{3)} \quad F_3 = \begin{cases} 0 & if F_1 \neq F_2 \\ 1 & if F_1 = F_2 \end{cases}$$

  The ROIs (size = 20×20 $pixels$, pixel size: $\Delta_x = \Delta_y = \Delta = 0.1$ μm) centered at pixels where $F_3 = 1$ are selected for further analysis.

- **Localization and emitter counting**
  The fundamental idea behind the algorithm is to fit a 2D Gaussian at the estimated locations, then subtract the fit image from the original image to obtain a residual image. Then, the residual image is examined to check whether the maximum intensity is above the user-specified threshold I_0 and that the maximum number of emitters in the ROI is not reached yet, i.e. $e < E_{MAX}$. If this is the case, a new emitter is added, and then fit simultaneously with the emitters identified in previous cycles.

  - **For** $e = 1$
    The CoM of the ROI is used as the initial position estimate for the $2D$ Gaussian fits, as denoted in Equation 13.
  - **For** $1 < e < E_{max}$
    The found position estimates in the previous cycle(s) are used as initial position estimates for these specific emitters. The remaining initial position estimate of the added emitter is found by calculating the CoM of the residual image, which is obtained by the subtraction of the fit model from previous residual (original image for the first cycle). The ROI is padded with a border size $b = 2$, to make sure that the captured photons are most likely to be coming from an emitter within the ROI. This process is repeated until there is no further indication of undetected emitters in the residual image, which in essence means that the maximum intensity is below the user-specified threshold I_0 or that the maximum number of emitters in the ROI is reached $e = E_{MAX}$.

- **Parameter estimation - MLE**

The MLE method is considered to be one of the most powerful statistically based methods used for parameter estimation, since it generally provides accurate estimation results[24]. Its outcome is defined to be the value of the parameter vector θ that maximizes the probability of observing data n, i.e. the value that maximizes the likelihood function of θ given n. The parameter values $\hat{\theta}$ are found such that they maximize the likelihood such that, the process described by the model, produced the data that were actually observed. The MLE is known to be asymptotically unbiased and efficient. When the PDF of the data $p(n|\theta)$ satisfies some regularity conditions (Appendix 7B[18]), the MLE of the unknown parameter θ is asymptotically normally distributed according to:

$$\hat{\theta}_{MLE} \sim \mathcal{N}\big(\theta^*, \mathcal{I}^{-1}(\theta)\big)$$

with the mean being the true parameter value θ^* and it attains the CRLB ($\mathcal{I}^{-1}(\theta)$) as the variance. The likelihood function, for an image with K pixels, for parameter θ is defined as:

$$\mathcal{L}(n|\mu(\theta)) = \prod_{k=1}^{K} P(n_k|\mu_k(\theta)) \tag{8}$$

We continue with the simpler log-likelihood instead of the original likelihood. Due to the fact that, logarithms are monotonically increasing functions, this manipulation can be performed. After maximization, the obtained $\hat{\theta}$ that maximizes the manipulated function, is the same $\hat{\theta}$ that maximizes the original function . To ease the computations further, it is common to normalize the likelihood function by dividing by the maximum possible likelihood $\mathcal{L}(n|n)$ (i.e. when $\mu_k = n_k$) and minimize twice the negative logarithm of this ratio in order to change the repeated products into sums[25]. The obtained function to be minimized is then defined as:

$$\mathcal{F}(\theta) = -2 \ln \left[\frac{\mathcal{L}(n|\mu(\theta))}{\mathcal{L}(n|n)} \right] \tag{9}$$

The following set of parameters per ROI is estimated with the Levenberg-Marquard algorithm:

$$\theta = [\theta_{bg}, \theta_{x_1}, \theta_{y_1}, \theta_{I_1}, \theta_{x_2}, \theta_{y_2}, \theta_{I_2}, \ldots, \theta_{x_E}, \theta_{y_E}, \theta_{I_E}], \qquad \in \mathbb{R}^T \tag{10}$$

In some cases, the inversion of the Hessian matrix may become numerically ill-conditioned if the Hessian matrix is almost singular. For this reason, the diagonal elements of the matrix α are augmented by an adaptive parameter λ such that: $\hat{\alpha} = \alpha(I + I\lambda)$, whereby the identity matrix $I \in \mathbb{R}^{T \times T}$. The iteration step is defined as (see Supplementary Note B.4):

$$\theta_{t+1} = \theta_t + \hat{\alpha}^{-1}\beta \tag{11}$$

whereby matrix $\alpha \in \mathbb{R}^{T \times T}$ and vector $\beta \in \mathbb{R}^T$ are defined as:

$$\alpha_{i,j} = \sum_{k=1}^{K} \frac{\partial \mu_k}{\partial \theta_i} \frac{\partial \mu_k}{\partial \theta_j} \frac{n_k}{\mu_k^2}, \qquad \beta_i = -\sum_{k=1}^{K} \left(1 - \frac{n_k}{\mu_k}\right) \frac{\partial \mu_k}{\partial \theta_i} \tag{12}$$

- **Parameter Initialisation**
  Having a good initial estimate for the parameters is important to get fast and reliable fits. A good initial estimate will require less iterations to converge. An initial estimate that is too far from the real parameters can cause the optimization algorithm to get stuck in a local minimum since the optimization problem is a highly non-convex one. Therefore, a method to get reliable initial estimates for position, intensity and background is required. First, the background is calculated as the modus intensity, i.e. the intensity that is most frequent through out the image (the mean intensity provided roughly the same results). For the initial estimate of the position $\{x_0, y_0\}$ the CoM of the ROI is considered, then processed using the conventional SMLM pipeline:

$$\hat{x} = COM_x = \frac{\sum_{k=1}^{K} n_k x_k}{\sum_{k=1}^{K} n_k}, \qquad \hat{y} = COM_y = \frac{\sum_{k=1}^{K} n_k y_k}{\sum_{k=1}^{K} n_k} \tag{13}$$

- **Constraints**
  For any real world problem, the parameters are bounded based on the physical characteristics and limitations of the system. The parameter vector is constraint such that $\theta \in \Theta$:

  ◦ Lower bound of θ: $\theta_l = \begin{bmatrix} \theta_{bg_{min}} & \underbrace{\theta_{x_{min}} \quad \theta_{y_{min}} \quad \theta_{I_{min}}}_{\theta^*_{min}} \end{bmatrix}^\mathsf{T} = \begin{bmatrix} \theta_{bg_{min}} & \theta^*_{min} \end{bmatrix}^\mathsf{T} \in \mathbb{R}^4$

  ◦ Upper bound of θ $\theta_u = \begin{bmatrix} \theta_{bg_{max}} & \underbrace{\theta_{x_{max}} \quad \theta_{y_{max}} \quad \theta_{I_{max}}}_{\theta^*_{max}} \end{bmatrix}^\mathsf{T} = \begin{bmatrix} \theta_{bg_{max}} & \theta^*_{max} \end{bmatrix}^\mathsf{T} \in \mathbb{R}^4$

$$\tilde{\theta}_l = \begin{bmatrix} \theta_{bg_{min}} & e_E \otimes \theta^*_{min} \end{bmatrix}^\mathsf{T} \in \mathbb{R}^T, \qquad \tilde{\theta}_u = \begin{bmatrix} \theta_{bg_{max}} & e_E \otimes \theta^*_{max} \end{bmatrix}^\mathsf{T} \in \mathbb{R}^T$$

with

$$e_E = \begin{bmatrix} 1 & \dots & 1 \end{bmatrix}^\mathsf{T} \in \mathbb{R}^E$$

Typically we set:

$$\begin{aligned} &\theta_{x_{min}} = \theta_{y_{min}} = b * \Delta, && \theta_{x_{max}} = \theta_{y_{max}} = \Delta * (K - b), \\ &\theta_{bg_{min}} = 0, && \theta_{bg_{max}} = [100 - 250] \\ &\theta_{I_{min}} = \theta_{bg_{max}}, && \theta_{I_{max}} = 10^4 \end{aligned}$$

for b being the border size in pixels (typically 2).

- **General problem formulation**

$$\hat{\theta}_{MLE} = arg\max_{\theta\in\Theta} \mathcal{L}(n|\mu(\theta)) = arg\min_{\theta\in\Theta} \; 2\sum_{k=1}^{K}\big(\mu_k(\theta) - n_k\big) - 2\sum_{\substack{k=1\\ n_k\neq 0}}^{K} n_k \ln\big(\frac{\mu_k(\theta)}{n_k}\big) \quad (14)$$

$$subject\ to\ \ \tilde{\theta}_l \leq \theta \leq \tilde{\theta}_u$$

- **Chi-squared $\mathcal{X}^2$-test**
  After parameter estimation, we still have to decide at what point the estimate is good enough. The Chi-squared test, $\mathcal{X}^2$-test, is used to determine whether there is a statistically significant difference between the expected and the observed model. This is the case when the LM algorithm is stuck in a local minimum, which does not satisfy the $\mathcal{X}^2$-test. The $\mathcal{X}^2$-test is defined as:

$$\mathcal{X}^2_{MLE} = \sum_{k=1}^{K} \frac{(n_k - \mu_k(\hat{\theta}_{MLE}))^2}{\mu_k(\hat{\theta}_{MLE})} \quad (15)$$

  Since the measured values are produced by a Poisson process, the expected value and standard deviation for the $\mathcal{X}^2$ value are given by:

$$E\big[\mathcal{X}^2\big] = K, \qquad \sigma\big[\mathcal{X}^2\big] = \sqrt{2K + \sum_{k=1}^{K}\frac{1}{\mu_k}} \quad (16)$$

  The critical value set to express the level of confidence (95%) we have in the observed with respect to the expected value is:

$$\mathcal{X}^2_{threshold} = K + 2\sqrt{2K + \sum_{k=1}^{K}\frac{1}{\mu_k}} \quad (17)$$

- **Initialisation and user settings**
  - Set intensity threshold I_0: a user-specified minimum peak intensity. If the maximum intensity in the (residual) image is below this value, then exit the algorithm and execute the $\mathcal{X}^2$-test.
  - Set the number of max emitters within a ROI E_{max}
  - Set error threshold ϵ (see Figure 2)
  - Set the number of initial estimates S
  - Set the LM optimization algorithm parameters: λ and max number of iterations
- **Running parameters**
  - Current number of emitter e
  - Current initial estimate $\theta_{init,s} \in \Theta \ \ for\ s = \{1, 2, \ldots, S\}$
  - Fraction of accepted ROIs:

$$\eta_{\mathcal{X}^2} = \frac{\text{Accepted ROIs}}{\text{Total ROIs}}$$

- **Filtering and Model Selection**
  We select S starting points in the feasible set ($\theta_{init,s} \in \Theta \;\; for \;\; s = \{1, 2, \ldots, S\}$), and for each starting point, we run the optimization algorithm, where it will probably get stuck in a close local minimum. From the set of returned solutions, we select the one that yields the lowest value for the objective function, and thus with the highest likelihood. Although this method is widely used in practice, it is not always very efficient. However, if based on physical insights or on additional (prior) information about the problem, it is possible to select our initial points in a specific region or in a specific way, causing the process to be much more efficient. In our case, we center the S starting points around the CoM of the ROI. To add an extra layer of control, we perform the χ^2-test to check whether there is a statistical significant difference between the expected and the observed measurements. If all the S starting points do not pass the χ^2-test, the respective ROI is dismissed. A presumable explanation for this could be that the cross-sectional area of the global minimum, at which the ground true parameters are located, is relatively small compared to its surrounding local minima, causing the optimization approach to get stuck in neighbouring minima before it could reach the global minimum, see Supplementary Note A.1. To investigate whether an increase of the number of initial estimates S, would improve the amount of used data, i.e. increase the fraction of acceptable ROIs (η_{χ^2}) with an acceptable χ^2-test, the estimation procedure was repeated S times ($S \geq 1$) for each ROI. The position with the highest likelihood was selected as the final estimate for that ROI. However, this was found to be computationally demanding; for this reason a small adjustment is made. Upon the total set of detected ROIs, the estimator is executed with the CoM as the initial estimate. The set of rejected ROIs undergoes the whole procedure again but with the next initial estimate in the set. The stopping criteria is set to be if $\eta_{\chi^2} >= 90\%$ or all the S initial points do not pass the χ^2-test.

- **Performance Evaluation**
  The performance evaluation is performed based on both quantitative and qualitative metrics. The aim is to obtain a refined understanding of the resolution and quantification capability of the algorithm and how it performs in comparison to state-of-the-art SMLM algorithms.

  - **Qualitative metrics:**
    The foremost consideration for the localization algorithm is how accurately it finds the position of labelled molecules. This was quantified as the root-mean-square error (RMSE) between the estimated molecule position and the ground truth, in the lateral position, also referred to as the localization accuracy. Hence, accuracy is a measure of the systematic error or bias in measurements, not to confuse with precision, which is a measure of the error spread of an estimator. The evaluation of localization accuracy was based on calculating the distances between the algorithm's localizations of each recognized emitter and the nearest true position of an emitter (within ϵ). The RMSE and the precision are defined as:

$$RMSE = \sqrt{\frac{\sum_{m=1}^{M} (\hat{\theta}_{x_m} - \theta_{x_m})^2 + (\hat{\theta}_{y_m} - \theta_{y_m})^2}{M}}, \qquad Precision \;\; \sigma = \sqrt{\sigma_x^2 + \sigma_y^2} \tag{18}$$

    whereby, $\sigma_x = \sqrt{\frac{\sum_{m=1}^{M} (\hat{\theta}_{x_m} - \bar{\theta}_x)^2}{M-1}}, \qquad \sigma_y = \sqrt{\frac{\sum_{m=1}^{M} (\hat{\theta}_{y_m} - \bar{\theta}_y)^2}{M-1}}$

    for M number of measurements.

- **Quantitative metrics:**
  Besides localization accuracy and precision, the algorithm performance also depends on the ability to successfully detect fluorescent emitters. It is crucial to accurately detect a large fraction of molecules in a dataset, and minimize false localizations. For every detected ROI, we identified the localizations that are close enough to a ground-truth position as true-positives (TP), error $< \epsilon$. The localizations were the error $> \epsilon$ are indicated as false-positives (FP) and the undetected positions are referred to as false-negatives (FN). The threshold ϵ, is the Euclidian distance between the fitted and ground-truth positions, unless mentioned otherwise we set $\epsilon = 0.2\ \mu m$. A visualization is provided in Figure 2.

  – Recall Fraction: $r = \frac{TP}{FN+TP}$, describes the overlap between the true fluorophores positions and the detected positionsi.e it provides the fraction of positions that are correctly identified of the total number of emitters.
  – Jaccard Index: $JAC = \frac{TP}{FP+TP+FN}$, same as recall fraction but takes the FNs in consideration.

- **If** $\mathcal{X}^2_{MLE} <= \mathcal{X}^2_{threshold} \rightarrow$ **ACCEPTED** $\rightarrow Calculate\ error$
  Determine the number of TPs, FPs and FNs.

- **Else if** $\mathcal{X}^2_{MLE} > \mathcal{X}^2_{threshold} \rightarrow$ **REJECTED** $\rightarrow$ Reset emitter count $e = 0$, grap the next initial estimate in $\theta_{init,s}$ and repeat procedure.
- **Results**
  Return list of localizations.

A schematic representation of this procedure is included in Supplementary Figure A.3.

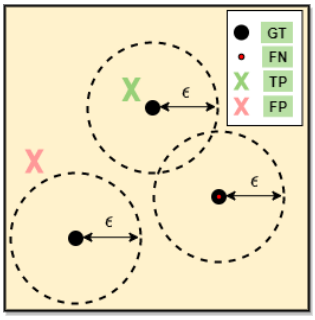

Figure 2. Localization classification - Ground true (GT): the true emitter location; True positive (TP): the successfully localized positions (difference between estimated location and ground true position $\leq \epsilon$); False positives (FP): difference between estimated location and ground true position $> \epsilon$; False negatives (FN): non-localized ground true positions.

It is commonly known that the quantitative and qualitative metrics are reversely related. If we only permit well isolated bright emitters and set a small successful detection distance threshold ϵ, this will result in good localization precision and accuracy but in a bad recall fraction. Conversely, allowing poorly fitted emitter localizations (increasing ϵ), results in precision and accuracy deterioration but improves the recall fraction. The optimal value for ϵ is therefore application-specific.

3. Results

In this section, we present the theoretical and numerical performance evaluation results of the Multi-SIMFLUX algorithm against standard 2D-Gaussian SMLM on simulated data. To asses the performance of SIMFLUX, several simulations were done for different active emitter densities and various emitter and background intensities. The localization performance of multi-SIMFLUX for various active emitter densities is compared against single-SIMFLUX, single-SMLM and multi-SMLM ($E = 5$). These simulations explore the effect of different realistic imaging conditions on the recall fraction, Jaccard index, localization precision and accuracy achieved by the algorithm. The use of simulated data has the advantage of the imaging conditions being known and more in control, e.g. the true emitter positions and intensities are known a priori, and no assumptions for variables like background intensities and PSF shapes have to be made. However, experimental measurements like for cell imaging, can contain a non-negligible amount of background noise; therefore, it is also of great importance to asses the performance of the localization algorithm if used on noisy image data.

We assume Poisson distributed data and neglect the read-out noise of the sensor, i.e. we assume only the shot noise to be present in the images. For all simulations the considered ROI-size is 20×20 $pixels$, the pixel size was set to $\Delta_x = \Delta_y = \Delta = 0.1$ μm and PSF width $\sigma_{PSF} = 1.3\Delta$ (unless mentioned otherwise). We matched detected emitters to the ground truth emitters with a lateral threshold of 2Δ, i.e successful detection distance $\epsilon = 2\Delta = 200$ nm. The matching procedure went as follows; the Euclidean distance between the ground true and the estimated positions is determined. Then, if the minimal distance is $\leq \epsilon$, it is considered as an TP localization, and both coordinates (from the true- and the estimated list) are pulled out. However, if the minimal distance $> \epsilon$, the localization is considered as a FP localization, and it is not considered in the recall fraction. Finally, if the list of estimations is empty, while they still are unmatched ground true positions, they are considered as FNs. See figure 2 for clarification.

3.1. Localization Performance

In this section, we investigate the expected theoretical improvement for SIMFLUX over SMLM and investigate whether our MLE implementation approaches it. Furthermore, we evaluate the effect of emitter photon count and background intensity on the localization precision and accuracy, for visualization see Supplementary Figure A.1.
The Fisher information in the x-direction of the ith emitter for $i \in [1, \dots, E]$ is denoted as:

$$\mathcal{I}_{x_i,x_i}(\theta) = \sum_{k=1}^{K}\sum_{p=1}^{\mathcal{P}}\sum_{e=1}^{E} \theta_{I_e} P_p(\theta_x, \theta_y, \phi_p) E_{x_{k,e}}(u) E_{y_{k,e}}(v) \Big(\frac{\partial \ln \mu_{k,p}}{\partial \theta_{x_i}}\Big)^2 \tag{19}$$

For the single emitter case, $E = 1$:

$$\mathcal{I}_{x_1,x_1}(\theta) = \sum_{k=1}^{K}\sum_{p=1}^{\mathcal{P}} \theta_{I_1} P_p(\theta_x, \theta_y, \phi_p) E_{x_{k,e}}(u) E_{y_{k,e}}(v) \Big(\frac{x-\theta_x}{\sigma} + \frac{2\pi q_{p,x} m_p \sin(\phi_p)}{1 + m_p \cos(\phi_p)}\Big)^2$$

Since $\sum_{k=1}^{K}\sum_{p=1}^{\mathcal{P}} \theta_{I_1} P_p(\theta_x, \theta_y, \phi_p) E_{x_{k,1}}(u) E_{y_{k,1}}(v) \approx \sum_{k=1}^{K} \theta_{I_1} E_{x_{k,1}}(u) E_{y_{k,1}}(v) \approx \theta_{I_1}$, approximating the pixel summation with the integration results in:

$$\mathcal{I}_{x_1,x_1}(\theta) \approx \frac{\theta_{I_1}}{\sigma^2} + 4\pi^2 \theta_{I_1} \sum_{p=1}^{\mathcal{P}} q_{p,x}^2 \underbrace{\eta_p m_p^2 \frac{\sin^2(\phi_p)}{1 + m_p \cos(\phi_p)}}_{Q_p}$$

For the multi emitter case, $E > 1$:

$$\mathcal{I}_{x_i,x_i}(\theta) = \sum_{k=1}^{K}\sum_{p=1}^{\mathcal{P}}\sum_{e=1}^{E} \theta_{I_e} P_p(\theta_x, \theta_y, \phi_p) E_{x_{k,e}}(u) E_{y_{k,e}}(v) \Big(\frac{\partial \ln \mu_{k,p}}{\partial \theta_{x_i}}\Big)^2 \approx \frac{N}{\sigma^2} + 4\pi^2 \theta_{I_e} \sum_{p=1}^{\mathcal{P}} q_{p,x}^2 Q_p$$

for N being the total number of photons captured from E emitters i.e. $N = \sum_{e=1}^{E} \theta_{I_e}$. The obtained improvement factor, for the two considered orthogonal orientations (x, y), and for perfect modulation $m = 1$, can then be expressed as (Supplementary Note B.3):

$$\mathcal{I}_{x,x}(\theta) = \mathcal{I}_{y,y}(\theta) = \frac{N\mathsf{p}^2 + 2\pi^2 N\sigma^2}{\sigma^2 \mathsf{p}^2} \quad \rightarrow \quad \sigma_{x,x}(\theta) = \sigma_{y,y}(\theta) = \frac{\sigma}{\sqrt{N}} \frac{1}{\sqrt{1 + \frac{2\pi^2\sigma^2}{\mathsf{p}^2}}}$$

Therefore, the improvement factor (I_f) for N emitters is equal to:

$$I_f = \frac{\sigma_{SMLM}}{\sigma_{SIMFLUX}} = \frac{\frac{\sigma}{\sqrt{N}}}{\frac{\sigma}{\sqrt{N}} \frac{1}{\sqrt{1 + \frac{2\pi^2\sigma^2}{\mathsf{p}^2}}}} = \sqrt{1 + 2\pi^2 \big(\frac{\sigma}{\mathsf{p}}\big)^2}$$

Which shows that for SIMFLUX with respect to SMLM the theoretical improvement factor $I_f \geq 1 \; \forall \; \mathsf{p}, \sigma$. However, the assumption of perfect modulation contrast ($m = 1$) cannot be guaranteed in practise. For $m < 1$, the localization precision will become worse and dependent on the illumination pattern phase, whereby a lower improvement factor can be expected. This results in the localization precision being non-uniform and anisotropic to some extend.
This means that there are small variations in localization precision depending on the position of the molecule with respect to the minima of the illumination patterns (see Figure A.7 to A.9).

In the simulations, we used a pitch to spot-width ratio $\frac{\sigma}{p} \approx 0.5 - 0.6$ and a modulation depth $m \approx 0.95$, whereby SIMFLUX should theoretically achieve an improvement factor in the range of ~ 2.3 with respect to conventional SMLM. To validate this, a data stack consisting of $3.2 \cdot 10^4$ identically sized ROIs is generated, in which the emitters are placed as shown in Figure A.2 and the results are shown in Figure 3. Note that a deviation of $\pm$ 1.5 $pixel$ for each emitter location is allowed. The considered emitter intensities during the simulations, ranged from $10^2 - 10^5$ $photons$ and the background intensity from $5 - 50$ $photons/pixels$. For each considered emitter- and background intensity, 1000 five-emitter images were generated. After the generation of the data stack, Poisson noise is applied to the images. This data stack is analyzed by both algorithms, which return the estimated positions, emitter intensities and background. The CRLB is calculated for each emitter and compared with the obtained results in Figure 3.

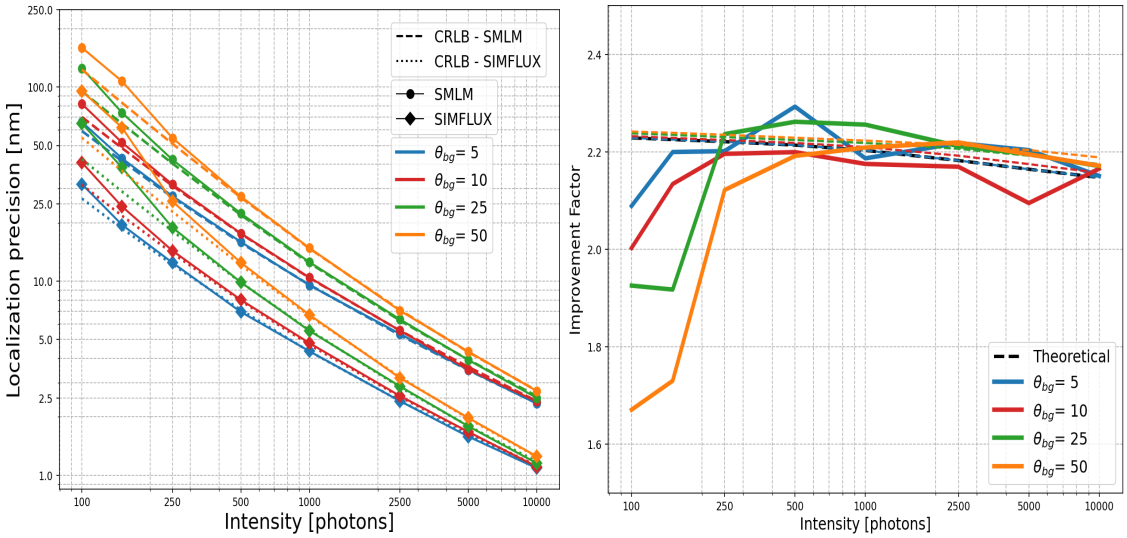

Figure 3. A data stack consisting of $3.2 * 10^4$ identically sized ROIs is generated in which five emitters are placed at the constant locations shown in Supplementary Figure A.2. **(a)** Impact of signal photon count on the localization precision of SIMFLUX in comparison to standard SMLM for different background intensities. **(b)** Improvement factor of SIMFLUX over SMLM in terms of localization precision. A precision improvement factor > 1.6 is realized over the whole considered emitter intensity range, and at intensities higher than 250 $photons$ an improvement factor of ~ 2.2 is achieved.

In case of placing the emitters at constant locations, both methods achieve the minimal possible estimation uncertainty, i.e highest localization precision, as given by their respective CRLB over a wide range of emission and background intensities as can be seen in Figure 3. These findings are consistent with our theoretical expectations, which was having a loss in localization precision by increasing levels of background intensities, since the presence of noise leads to an increase in the uncertainty of the emitter's location. In Figure 3-b, it can be seen, that at emitter intensities greater than 250 $photons$, the theoretical improvement factor of ~ 2.2 is reached. Also, the fact that the theoretical improvement factor slightly increased for higher background intensities can be noticed, which indicates the superiority of SIMFLUX in handling noisy images.

Next, the algorithms are tested on a simulated data set, where emitters were placed at random positions such that $\theta_x, \theta_y \in [b, K-b]$, with K being the number of pixels and b border size in pixels (typically 2). The expected photon count per emitter is selected from a normal distribution with $\theta_I \sim \mathcal{N}(1000, 250)$ and the background intensity θ_{bg} is set to 10 $photons/pixel$. The obtained results, in terms of measured localization precision in x and y direction, of SIMFLUX and SMLM in comparison with their respective average CRLB are depicted in Figure 4. A precision improvement factor of approximately ~ 2.0 is achieved for both the single and multi emitter case. For a visualisation of the effect of the active emitter density and background intensity on the two-dimensional localization accuracy of both algorithms, see Figure A.5.

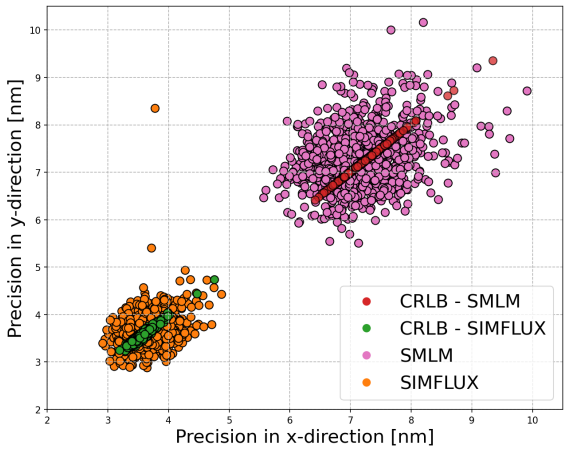

Figure 4. Comparison of localization precision and CRLB for multi-emitter fitting. A data stack is generated where four emitters are placed at random locations. The expected photon count per emitter is selected from a normal distribution with $\theta_I \sim \mathcal{N}(1000, 250)$, and the background intensity of the image θ_{bg} is set to 10 $photons/pixel$. The measured localization precision in x and y direction, of SIMFLUX and SMLM in comparison with their respective average CRLB. A precision improvement factor of ~ 2 is achieved.

To examine the effect of emitter and background intensity on the estimator's localization accuracy, we considered histograms of the error of the total set of localizations and their cumulative distribution functions. Histograms give a good visualisation of the localised points relative to the true molecular positions, whereby the negative and positive localization errors indicate an estimation to the left or to the right of the ground-true position, respectively. The cumulative distribution function of the localization error provides insightful characteristics, since it gives the possibility to extract the probability of finding a localization error less or greater than a certain value. Also, the steepness of the slope gives an indication of the spread of the localization error. In Figure 5, the cumulative distribution function is given for various emitter- and background intensities. It demonstrates the effect of emitter- and background intensity on the estimator accuracy. As expected, the steepness increases with higher emitter intensity and decreases with higher background intensities. The slopes for SIMFLUX are steeper than SMLM, which gives an inidication that the spread of localizations for SIMFLUX is narrower than SMLM, which is in line with the results obtained in Figure A.4.

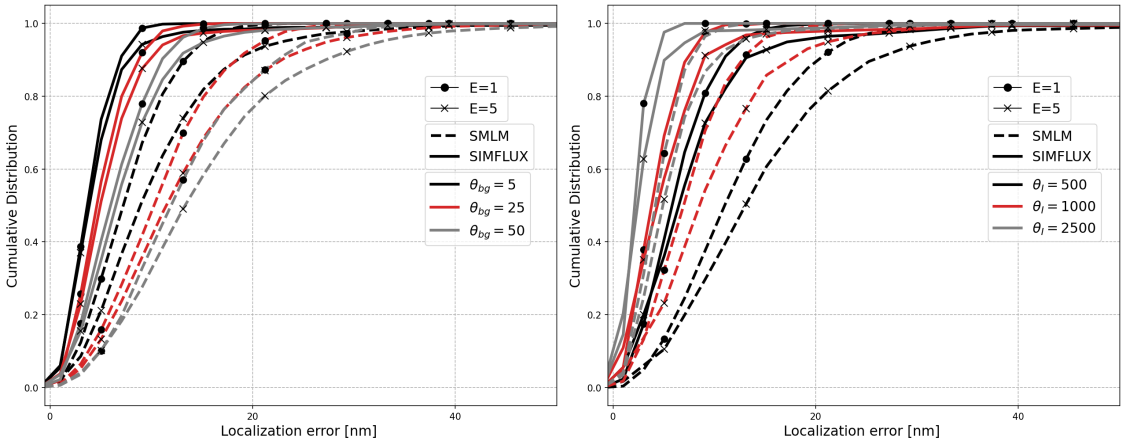

(a) Emitter Intensity $\theta_I \sim \mathcal{N}(1000, 250)$ Constant background intensity **(b)** $\theta_{bg} = 5$

Figure 5. Cumulative distribution of the obtained localization error (RMSE) by SMLM and SIMFLUX for random emitter positions. SIMFLUX outperforms SMLM for various emitter- and background intensities, for single- and multi-emitter case. **(a)** Impact of background intensity on the localization accuracy of SMLM and SIMFLUX, for single ($E = 1$) and multi emitters ($E = 5$). **(b)** Impact of emitter intensity on the localization accuracy, of SMLM and SIMFLUX, for single and multi emitters.

3.2. Probability Error

In some detection problems, it is reasonable to express a prior belief in the likelihood, by assigning probabilities to the various possible hypotheses. We consider the case where we wish to distinguish between M hypotheses $\{H_0, H_1, \ldots, H_{M-1}\}$. Such a problem arises in case of the classification of the number of emitters, i.e. deciding how many active emitters there are within a certain ROI. The hypothesis H_0, suggests that there are no active emitters in a given ROI (just background noise), H_1 suggests that there is one active emitter, and so on. For decision optimization, commonly the minimum probability error P_e criterion or its generalization, the Bayes risk, is employed[18]. The expected cost or Bayes risk is denoted as:

$$\mathcal{R} = \sum_{i=0}^{M-1} \sum_{j=0}^{M-1} C_{i,j} P\left(H_i \middle| H_j\right) P\left(H_j\right) \tag{20}$$

The cost (loss in performance) assigned to the decision to choose H_i when H_j is true, is denoted by $C_{i,j}$. We aim to choose the hypothesis (number of emitters) that minimizes the cost, hence optimizes performance. Let R_i be the set of values in R^M which map into the decision H_i. So in essence $R_i = \{x : \ decide\ H_i\}$, where $i = 0, 1, \ldots, M-1$, partitions the decision space such that:

$$\mathcal{R} = \sum_{i=0}^{M-1} \int_{R_i} \sum_{j=0}^{M-1} C_{i,j} P\left(H_j \middle| x\right) P\left(x\right) dx$$

The goal is to decide H_i for which the expected cost is minimum. Since $P(x)$ is common to all terms and it is reasonable to assign equal probabilities to prior probabilities of the respective hypotheses, i.e. $P(H_i) = \frac{1}{M} \;\; \forall\, i = \{0, 1, \ldots, M-1\}$, we get:

$$\hat{H} = arg\min_i \frac{1}{M} \sum_{j=0}^{M-1} C_{i,j} P(x|H_j)$$

We define the probability of error P_e as:

$$P_e = \sum_{i=0}^{M-1} \sum_{\substack{j=0 \\ j\neq i}}^{M-1} P(x|H_j)P(H_j) = \frac{1}{M} \sum_{i=0}^{M-1} \sum_{\substack{j=0 \\ j\neq i}}^{M-1} P(x|H_j) \tag{21}$$

The probability of a correct decision is then defined as $P_c = 1 - P_e$. We consider the log-likelihood ratio between two hypotheses H_i, H_j, whereby the true parameters are considered to be known:

$$ln\ \left(LR_{i,j}\left(x\right)\right) = \ ln\left(\frac{p\left(H_l|H_i\right)}{p\left(H_l\middle|H_j\right)}\right)$$

The log-likelihood ratio tends to be normally distributed, as the number of data points goes to infinity ($x \to \infty$). The expected value μ and variance σ^2 are computed under the conditional H_i, i.e. the one assumed to be true:

$$\mu_{i,j,l} = \sum_k^K \mu_k^l \ln(\frac{\mu_k^i}{\mu_k^j}) - \mu_k^i + \mu_k^j, \qquad\qquad \sigma_{i,j,l}^2 = \sum_k^K \mu_k^l \ln(\frac{\mu_k^i}{\mu_k^j})$$

To evaluate this, the algorithms are tested on a simulated data consisting of $7.5 * 10^3$ ROIs per emitter configuration and emitter- and background intensity combination. For the emitter configurations with $E > 1$, the emitters are equidistantly separated with a radius r with respect to the center of ROI. The emitter intensity θ_I per emitter is selected from a normal distribution with $\sim \mathcal{N}(\theta_I, 0.2 * \theta_I)$, after which a background intensity of θ_{bg} is added. For ROIs visualisation, see Supplementary Figures A.11 to A.14.

The overlap, between the true-likelihood function and between the other likelihood functions, is considered as an indication for the probability of making an emitter quantification error. We noticed that the normal distribution did underestimate the log-likelihood distribution (specially for lower emitter number, see Figure A.15), causing a small overestimation of the P_e. Therefore, we estimated the distribution and resorted to numerical integration to approximate the value of overlapping area (Simpson's rule). The effect of separation distance, emitter- and background intensity on the probability error is shown in Figure 7, A.11 and A.12 respectively.

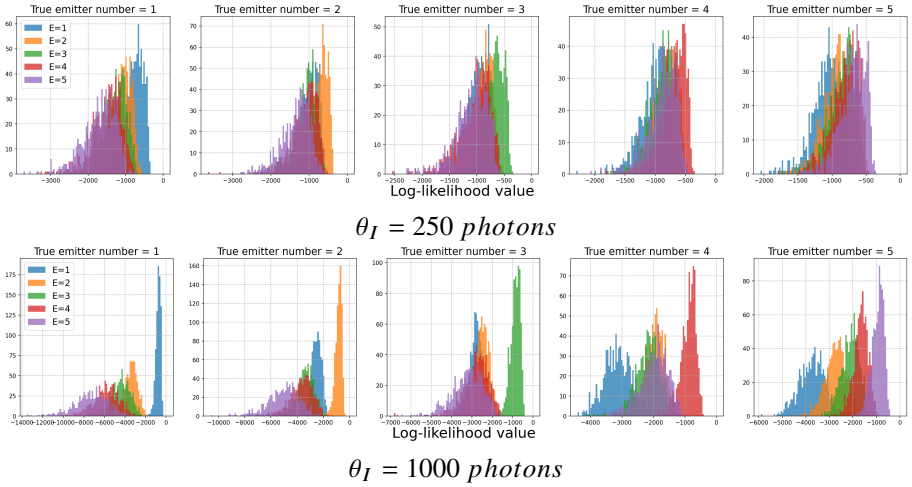

Figure 6. Multi-emitter log-likelihood results for different number of emitters, constant normalized distance w.r.t. ROI-center $\frac{r}{\sigma_{PSF}} = 2.5$ and background intensity $\theta_{bg} = 5\ photons/pixel$. For instance, in the second column of the top row, with emitter intensity $\theta_I = 250\ photons$, there is an overlap between the true-likelihood function of $E = 2$ and between other likelihood functions, indicating the probability of making an emitter quantification error. In the bottom row, with emitter intensity $\theta_I = 1000\ photons$, the overlap is almost zero, which corresponds to a low probability error.

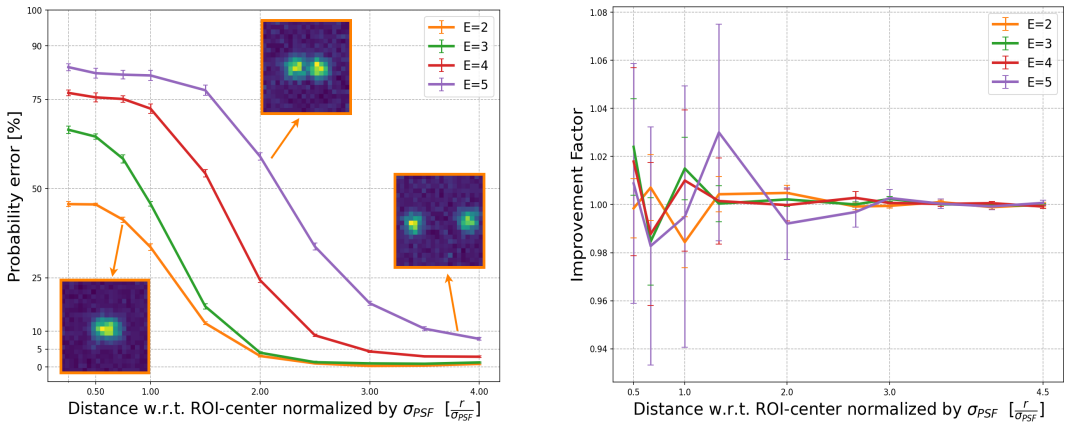

(a) **(b)**

Figure 7. **(a)** The effect of separation distance between emitters on the probability error, under constant emitter and background intensity, $\theta_I = 750\ photons$ and $\theta_{bg} = 5\ photons/pixel$, respectively. Note that at constant $(\frac{r}{\sigma_{PSF}})$ the probability error P_e increases with the number of emitters E within a ROI. A visualisation of the separation distance is shown for $E = 2$, see Supplementary Figure A.14 for further visualisation. **(b)** The ratio between the probability of making the correct decision of SIMFLUX and SMLM $(\frac{P_{c,SIMFLUX}}{P_{c,SMLM}})$ at different normalized separation distances. At small normalized separation distances $(\frac{r}{\sigma_{PSF}} \leq 2)$, the improvement factor w.r.t. SMLM alternates between between $\sim [-2, 3]\%$, while at greater separation distances the performance in terms of correct decision is roughly the same. SIMFLUX does not provide significant improvement over SMLM in terms of P_c for the different simulated separation distances.

3.3. Separation Distance

In this section, we evaluate the ability of the algorithm to distinguish two nearby emitters with different separation distances. The expected photon count for two emitters, equivalent in intensity $\theta_{I_1} = \theta_{I_2} = \theta_I$, separated by a separation distance d in x-direction ($E_{y_{k,1}} = E_{y_{k,2}} = E_{y_k}$) is:

$$\begin{aligned}
\mu_k &= \sum_{k=1}^{K} \theta_{I_1} E_{x_{k,1}}(u - \frac{d}{2}) E_{y_{k,1}}(v) + \theta_{I_2} E_{x_{k,2}}(u + \frac{d}{2}) E_{y_{k,2}}(v) + \theta_{bg} \\
&= \theta_I \sum_{k=1}^{K} E_{y_k} \Big(E_{x_{k,1}}(u - \frac{d}{2}) + E_{x_{k,2}}(u + \frac{d}{2}) \Big) + \theta_{bg} \\
&= \theta_I \sum_{k=1}^{K} E_{y_k} \Big(E_{x_{k,1}}(-\frac{d}{2}) + E_{x_{k,2}}(\frac{d}{2}) \Big) + \theta_{bg}
\end{aligned}$$

For the Fisher information, with separation distance $d = \theta_{x_1} - \theta_{x_2}$, we get:

$$\begin{aligned}
\mathcal{I}_d(\theta) &= \sum_{k=1}^{K} \frac{1}{\mu_k} \Big(\frac{\partial \mu_k}{\partial d} \Big)^2 = \sum_{k=1}^{K} \frac{1}{\mu_k} \Big(\frac{\partial \mu_k}{\partial \theta_{x_1}} - \frac{\partial \mu_k}{\partial \theta_{x_2}} \Big)^2 \\
&= \sum_{k=1}^{K} \frac{\Big(\theta_I E_{y_k} \big(\frac{\partial E_{x_{k,1}}(-\frac{d}{2})}{\partial \theta_{x_1}} - \frac{\partial E_{x_{k,2}}(\frac{d}{2})}{\partial \theta_{x_2}} \big) \Big)^2}{\theta_I E_{y_k} \Big(E_{x_{k,1}}(-\frac{d}{2}) + E_{x_{k,2}}(\frac{d}{2}) \Big) + \theta_{bg}} \\
&= \theta_I \sum_{k=1}^{K} \frac{E_{y_k}^2 \Big(\frac{\partial E_{x_{k,1}}(-\frac{d}{2})}{\partial \theta_{x_1}} - \frac{\partial E_{x_{k,2}}(\frac{d}{2})}{\partial \theta_{x_2}} \Big)^2}{E_{y_k} \Big(E_{x_{k,1}}(-\frac{d}{2}) + E_{x_{k,2}}(\frac{d}{2}) \Big) + \frac{\theta_{bg}}{\theta_I}} \\
&= \frac{\theta_I}{2\pi\sigma^2} \sum_{k=1}^{K} \frac{E_{y_k} \Big(\big(e^{\frac{-(-\frac{d}{2} + \frac{\Delta x}{2})^2}{2\sigma^2}} - e^{\frac{-(-\frac{d}{2} - \frac{\Delta x}{2})^2}{2\sigma^2}} \big) - \big(e^{\frac{-(\frac{d}{2} + \frac{\Delta x}{2})^2}{2\sigma^2}} - e^{\frac{-(\frac{d}{2} - \frac{\Delta x}{2})^2}{2\sigma^2}} \big) \Big)^2}{E_{x_{k,1}}(-\frac{d}{2}) + E_{x_{k,2}}(\frac{d}{2}) + \frac{\theta_{bg}}{\theta_I E_{y_k}}}
\end{aligned}$$

We know that the localization precision is bounded by:

$$\begin{aligned}
Var(\hat{\theta}) &\geq \mathcal{I}(\theta)^{-1} \\
\sigma_{\hat{\theta}} &\geq \sqrt{\mathcal{I}(\theta)^{-1}}
\end{aligned}$$

As the overlap between the two sources increases, i.e. for $d \to 0$, we get:

$$\lim_{d \to 0} \mathcal{I}_d(\theta) = 0 \quad \to \sigma_{\hat{\theta}} \to \infty$$

In case of $d \to \infty$, i.e. totally no overlap between the two sources so that the cross-terms become zero, we get the following:

$$\lim_{d \to \infty} \mathcal{I}_d(\theta) = \frac{\theta_I}{2\pi\sigma^2} \sum_{k=1}^{K} \frac{E_{y_k} \Big(\big(e^{\frac{-(-\frac{d}{2} + \frac{\Delta x}{2})^2}{2\sigma^2}} - e^{\frac{-(-\frac{d}{2} - \frac{\Delta x}{2})^2}{2\sigma^2}} \big)^2 + \big(e^{\frac{-(\frac{d}{2} + \frac{\Delta x}{2})^2}{2\sigma^2}} - e^{\frac{-(\frac{d}{2} - \frac{\Delta x}{2})^2}{2\sigma^2}} \big)^2 \Big)}{E_{x_{k,1}}(-\frac{d}{2}) + E_{x_{k,2}}(\frac{d}{2}) + \frac{\theta_{bg}}{\theta_I E_{y_k}}}$$

This, in fact, is equivalent to the individual Fisher information sum for the two emitters sources.

To demonstrate how the separation distance d affects the Fisher information, a series of simulated images of two emitters, with increasing separation distances between their centers, were generated for different values of σ_{PSF}. The emitter and background intensities were held constant at $\theta_I = 1000\ photons$ and $\theta_{bg} = 5\ photons/pixel$, respectively. The results are shown in Figure 8, where it can be seen that at a separation distance of approximately $d \approx 7\sigma_{PSF}$ the amount of Fisher information does not increase anymore for the different PSF widths. Note that the Fisher information is normalized.

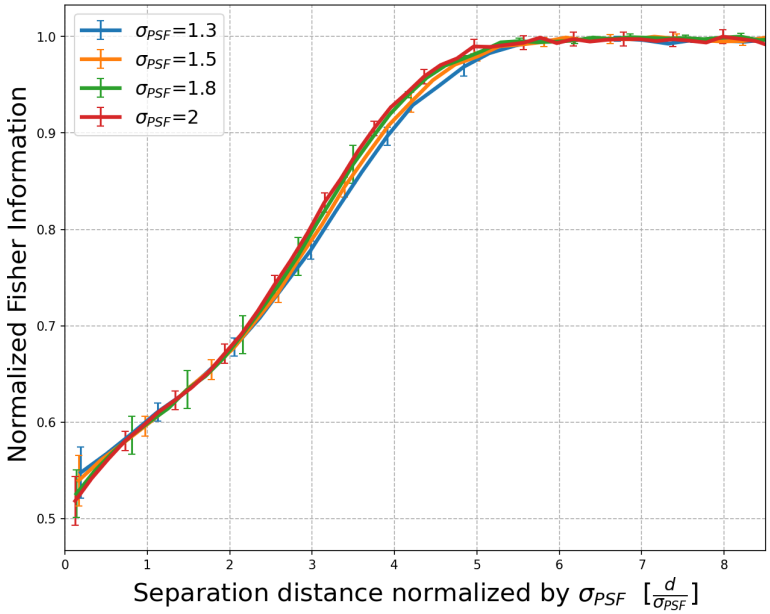

Figure 8. The impact of the separation distance between two emitters on the Fisher information for different values of σ_{PSF}. At a separation distance of approximately $d \approx 7\sigma_{PSF}$ the amount of Fisher information does not increase anymore for the different PSF widths.

Again, a series of images of two emitters with increasing separations between their centers were generated. The separation distance ranged from $0.025\ \mu m\ to\ 1.0\ \mu m$ ($\approx 7\sigma_{PSF}$), for visualisation see Supplementary Figure A.17. For each separation distance, for different background intensities $\theta_{bg} = \{5, 25, 50\}$ and different emitter photon counts $\theta_I = \{250, 500, 1000\}$, 5000 ROIs were generated. Poisson noise is applied to the images, then fitted by the SMLM and SIMFLUX algorithm. This was performed to analyse the ability of both algorithms in distinguishing between two nearby emitters at different separation distances.

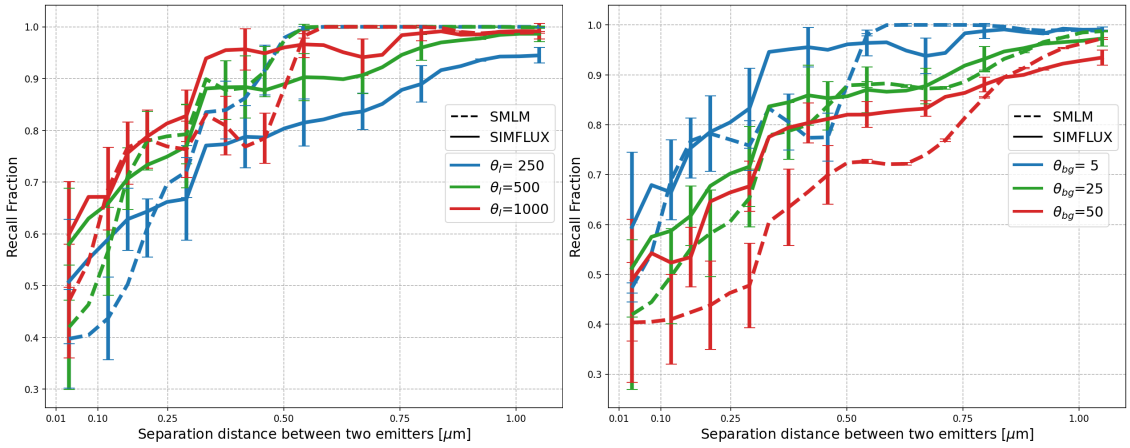

(a) **(b)**

Figure 9. The successful detection distance threshold is set to $\epsilon = 2.5$. **(a)** Impact of separation distance on the recall fraction of SIMFLUX in comparison to SMLM for different signal photon counts with a constant background intensity $\theta_{bg} = 5\ photons/pixel$. **(b)** Impact of separation distance on the recall fraction of SIMFLUX in comparison to SMLM for different background intensities with a constant emitter intensity of $\theta_I = 750$ photons.

From the simulations performed, for varying emitter and background intensities, it is clearly visible that SIMFLUX outperforms SMLM. The impact of separation distance on the localization precision for emitter and background intensities is displayed in Supplementary Figure A.7 and A.8, respectively. Furthermore, they show that the introduction of illumination pattern results in a spatially varying CRLB. The deterioration of localization precision, for lower emitter photon counts and/or higher background intensities, for SIMFLUX is less compared to SMLM. For the evaluated emitter- and background intensities, SIMFLUX is able to maintain an average localization precision improvement factor of ~ 2.

Figure 9 shows that the detection rate is also affected by the emitter intensity and background noise, since single molecules with lower emission rates and/or deeper axial positions are harder to detect. As theoretically expected, the recall fraction for both algorithms increases with larger separation distances, higher emitter intensities and lower background intensities. For instance in Figure 9a, at a separation distance of 0.1 μm for emitter intensity $\theta_I = 500$ SIMFLUX identified $\sim 65 \pm 4.3\%$ of the emitters correctly, while SMLM found $\sim 52 \pm 6.5\%$. For the same emitter intensity, at the same separation distance, the CRLB is $\sim 5\ nm$ for SIMFLUX and 10.5 nm for SMLM (Figure A.7). At very small separation distances ($\sim\leq 1.5\ pixel = 0.15\ \mu m$), for both algorithms the recall fraction is in the range of $\sim 40 - 60\%$, which has to do with the fact that the algorithms "see" the two emitters as just one emitter with double the intensity. In cases, where the optimization landscape displays distinct two minima (instead of merging them into one minimum), the algorithm is able to distinguish between the two emitter at such low separation distances, an example is illustrated in Supplementary Figure A.17. For separation distances greater than 0.5 μm, both algorithms achieve recall fraction $\geq 80\%$, SMLM even slightly higher due to its smoother optimization landscape, see Figure A.27.

3.4. *Active Emitter Density*

In this section, we demonstrate the superiority of multi-emitter approaches at high active emitter densities. The active emitter densities were controlled by placing a certain number of active emitters within the imaging frame area of $0 \times 150\ \mu m^2$. Note that each active emitter density is simulated 100 times with different random configurations. The expected photon count per emitter was selected from a normal distribution with $\theta_I \sim \mathcal{N}(1000, 250)$ and a background intensity θ_{bg} of 5 $photons/pixel$ was added, then the image was corrupted with Poisson noise. Various ROI-sizes, ranging from $5\sigma_{PSF}$ to $8\sigma_{PSF}$ for single-emitters and $8\sigma_{PSF}$ to $20\sigma_{PSF}$ for multi-emitter, were evaluated in the terms of recall fraction, Jaccard Index, localization precision and accuracy (RMSE).

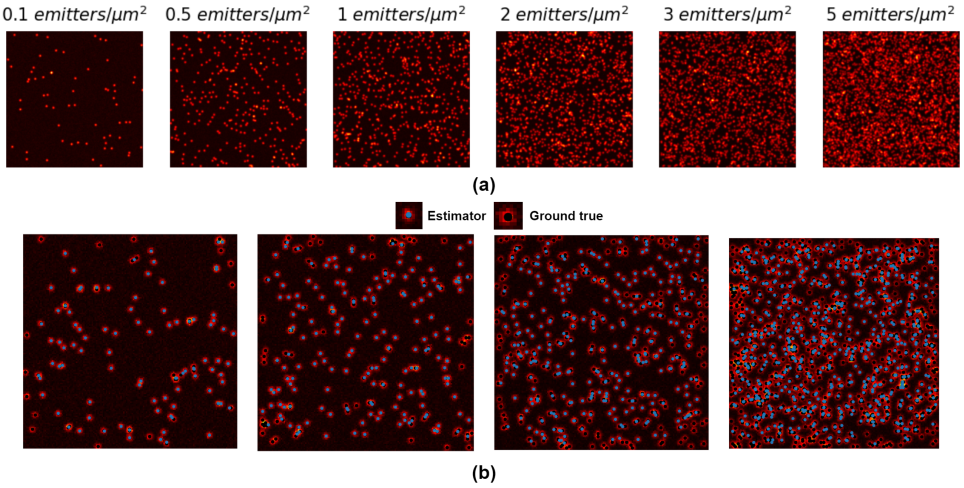

Figure 10. **(a)** Visualisation of various active emitter densities ranging from 0.1 *to* 5 $emitters/\mu m^2$. **(b)** Eamples of results with the obtained results for $E = 5$ at different active emitter densities (0.5, 1, 2 and 5 emitters/μm^2). The true positions are indicated with black circles and the positions identified by the SIMFLUX estimator with blue circles.

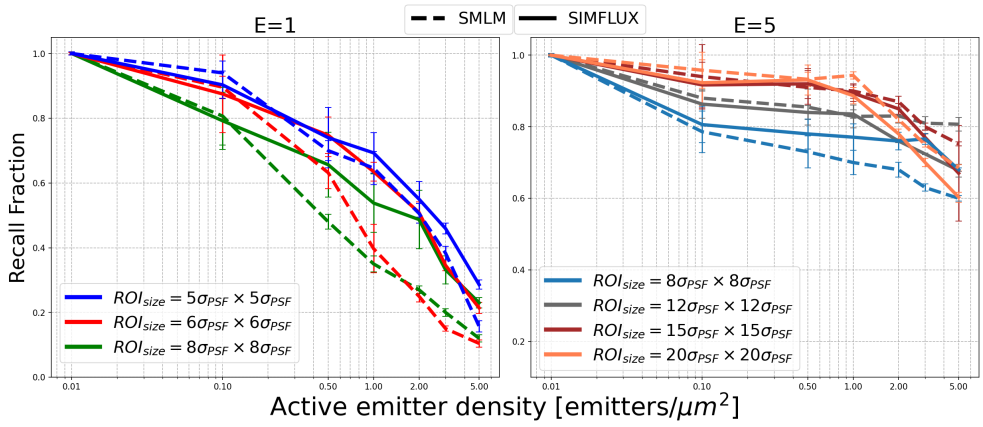

Figure 11. The impact of active emitter density on the recall fraction for single and multi emitters for different ROI sizes.

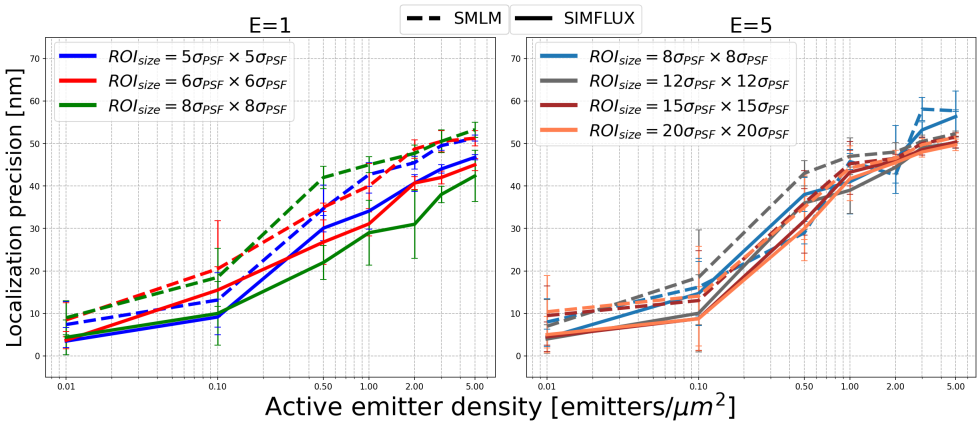

Figure 12. The impact of active emitter density on the localization precision for single and multi emitters for different ROI sizes.

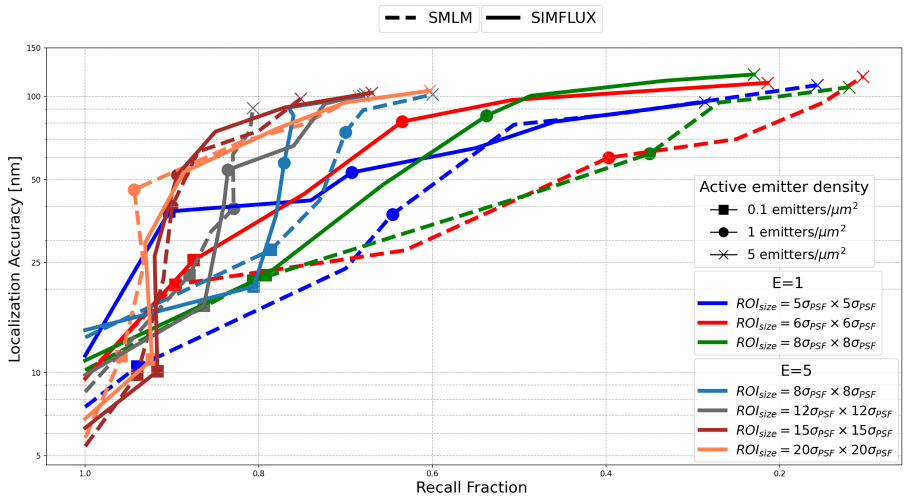

Figure 13. The relation between localization accuracy and recall fraction for each tested algorithm at different active emitter densities. The significant improvement of recall fraction compared with a slight improvement in localization accuracy, achieved by the multi-emitter over single emitter cases is cleary visible.

Some of the detected and localized ROIs can be seen in Supplementary Figure A.24. From Figures 11 and A.18, we see that the multi-emitter case, for both algorithms, at high active emitter densities (5 $emitters/\mu m^2$) is able to approximately double the recall fraction and Jaccard Index. The obtained recall fractions for the single emitter case at high active emitter densities are in the range of $\sim 10-35\%$, while the obtained recall fractions for the multi-emitter case are in the range of $\sim 60-80\%$. At the same active emitter density, the localization precision for single-emitter was determined to be $\sim 40-50$ nm vs. $\sim 50-60$ nm for multi-emitter, as can be seen in Figure 12. Also, in terms of localization accuracy at higher densities, the multi-emitter is case able to outperform the single-emitter approach. Again, at an active emitter density of 5 $emitters/\mu m^2$ the RMSE for single-emitter was determined to be $\sim 95-120$ nm vs. $\sim 85-105$ nm for multi-emitter, see figure A.19. Hence, with the multi-emitter approach we are able to averagely double the recall fraction, with only a slight deterioration in precision, approximately $\sim 20\%$.

3.5. Pattern Fitting

Ring Fitting

In this section, the performance of SMLM and SIMFLUX on the reconstruction of the three-ring structure, shown in Supplementary Figure A.21, is investigated . The aim is to benchmark the performance of both algorithms in their accuracy and the continuity of the obtained structures for varying ring radi and increasing active emitter frame density. The following frame and ring dimensions has been chosen $w = h = 10\ \mu m$, $R_1 = 3\ \mu m, R_2 = 1.5\ \mu m, R_3 = 0.5\ \mu m$, as can be seen in Figure A.21 a. The same procedure is applied under three different activate emitter densities, referred to as low, mid and high density. Examples of the simulated frames for SMLM and SIMFLUX are shown in Figure A.22 and A.23, respectively.

- Low-density: with an average density of is ~ 20 active $emitters/frame$.
- Mid-density: with an average density of is ~ 50 active $emitters/frame$.
- High-density: with an average density of is ~ 100 active $emitters/frame$.

For the following simulations, the considered ROI-size for $E = 1$ is $10 \times 10\ pixels$ and for $E = 5$ is $20 \times 20\ pixels$. The expected photon count per emitter is selected from a normal distribution with $\theta_I \sim \mathcal{N}(1000, 250)$ and the background intensity of the image θ_{bg} is set to $5\ photons/pixel$. Furthermore, we set a successful detection distance of $\epsilon = 100\ nm$,

Recall Fraction				
		Low	**Mid**	**High**
SMLM	E = 1	69.7 ± 5.13%	45.4 ± 4.63%	17.4 ± 4.52%
SIMFLUX	E = 1	64.3 ± 2.71%	39.7 ± 4.89%	19.6 ± 5.56%
SMLM	E = 5	92.3 ± 1.56%	82.2 ± 2.43%	65.6 ± 3.13%
SIMFLUX	E = 5	89.2 ± 1.93%	80.4 ± 4.82%	66.3 ± 3.25%

Table 1. Recall fraction three-ring structure.

Localization Precision				
		Low	**Mid**	**High**
SMLM	E = 1	24.9 ± 2.56 *nm*	26.8 ± 3.43 *nm*	28.1 ± 4.14 *nm*
SIMFLUX	E = 1	12.3 ± 2.24 *nm*	16.5 ± 3.67 *nm*	24.7 ± 3.32 *nm*
SMLM	E = 5	26.4 ± 3.77 *nm*	27.6 ± 4.11 *nm*	29.2 ± 4.82 *nm*
SIMFLUX	E = 5	13.8 ± 2.86 *nm*	18.7 ± 2.46 *nm*	25.3 ± 5.58 *nm*

Table 2. Localization precision three-ring structure.

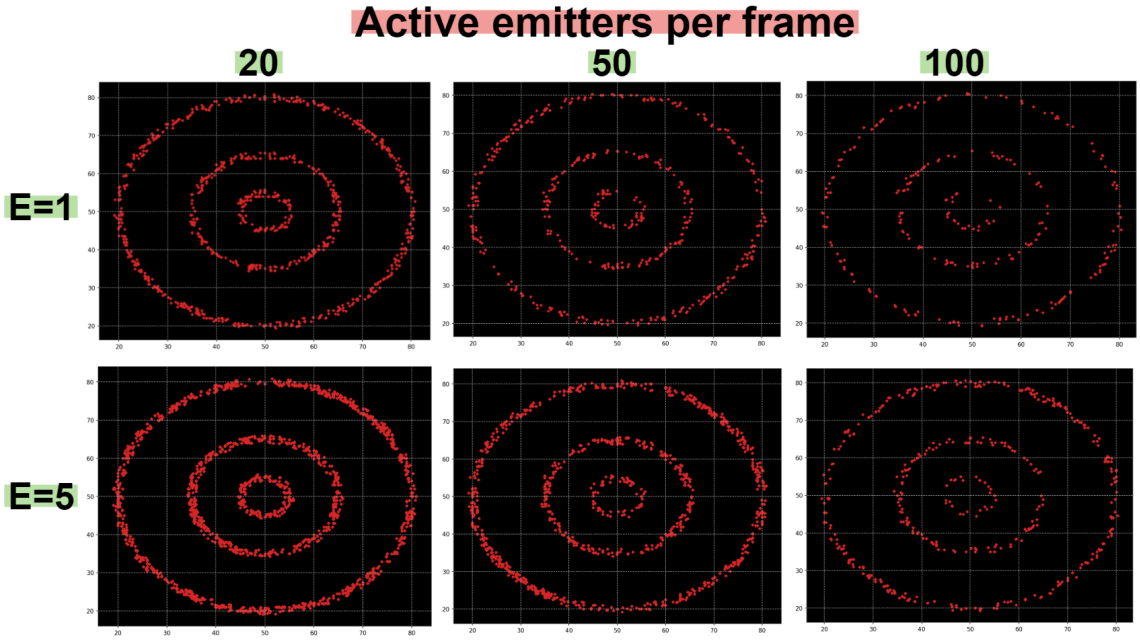

(a) SMLM

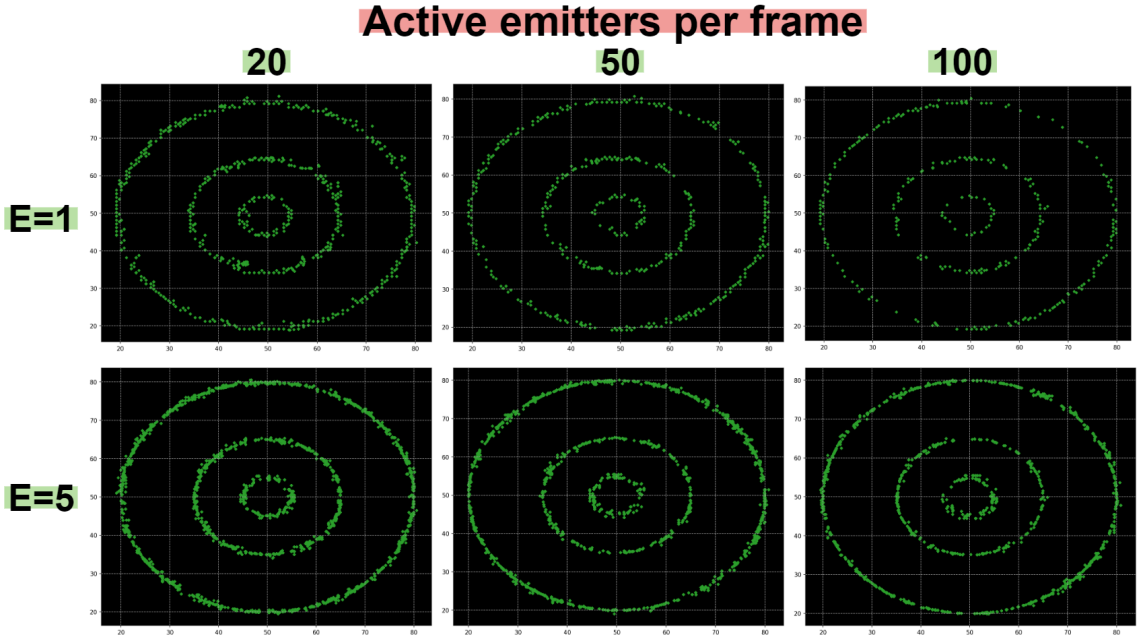

(b) SIMFLUX

Figure 14. Three-ring structure fitting results for SMLM **(a)** and SIMFLUX **(b)**, for single and multi emitter, at the following active emitter densities = 20, 50 and 100 emitters/frame. The increase in emitter recall rate and structure continuity, due to the extension form single to multi emitter approach is clearly visible. The achieved localization precision improvement factor of SIMLFLUX over SMLM decreases with increasing active emitter density. Throughout the considered frame densities the localization improvement factor stays in the range of $\sim 1.1 - 2.0$.

Siemens Star Fitting

In this section, we evaluate the resolving capability of SIMFLUX method against SMLM using simulated images with the Siemens star pattern. The synthetic Siemens star image series has 50 non-empty regions, a radius of 5 μm and a total number of 1.25^5 $emitters$. The active emitter densities were controlled by placing different number of emitters within the active area in the image. For the following simulations we set $\epsilon = 100$ nm

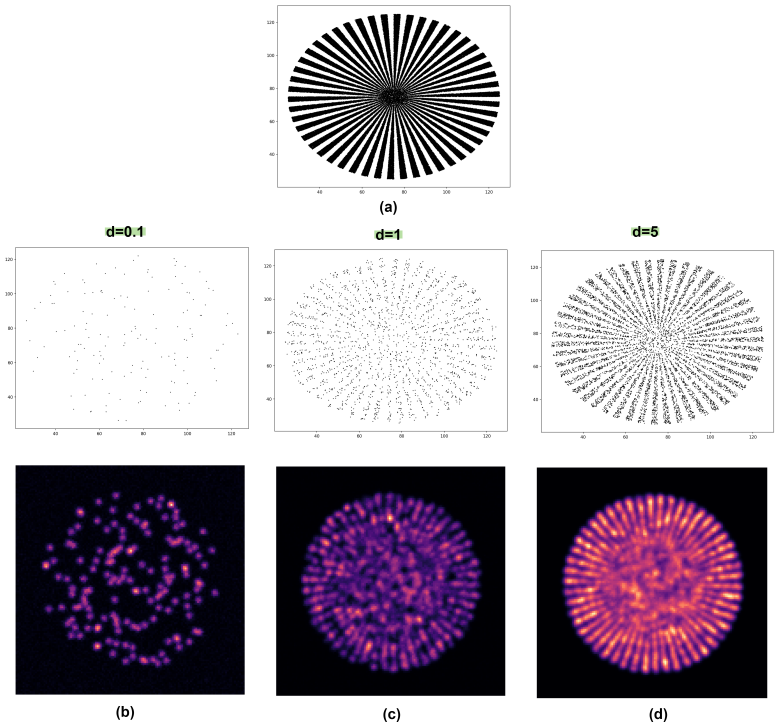

Figure 15. **(a)** The Siemens star ground true pattern. Siemens star object has been simulated for different active emitter densities under constant emitter and background intensity, $\theta_I = 750$ $photons$ and $\theta_{bg} = 5$ $photons/pixel$ respectively. **(b)** Active emitter density of 0.1 $emitters/\mu m^2$, **(c)** 1 $emitters/\mu m^2$, and **(d)** 5 $emitters/\mu m^2$.

Recall Fraction				
		d = 0.1	**d = 1**	**d = 5**
SMLM	E = 1	79.4 ± 2.16%	18.4 ± 2.35%	5.10 ± 0.81%
SIMFLUX	E = 1	73.6 ± 3.19%	16.6 ± 3.69%	4.89 ± 1.25%
SMLM	E = 5	89.2 ± 6.64%	68.3 ± 4.43%	31.4 ± 1.72%
SIMFLUX	E = 5	91.0 ± 5.49%	65.2 ± 5.25%	34.1 ± 1.65%

Table 3. Recall fraction Siemens star

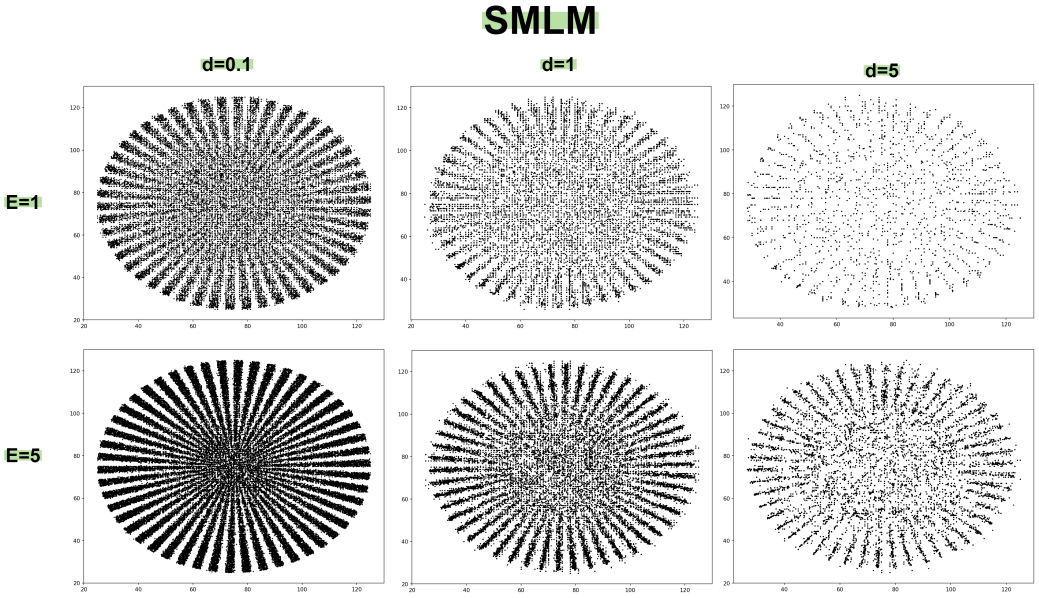

(a)

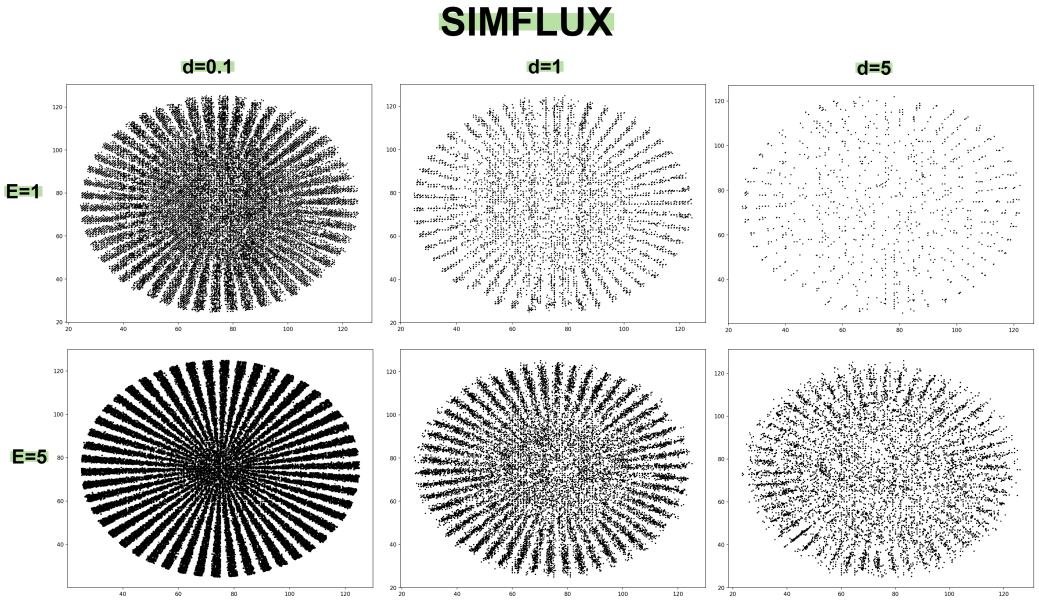

(b)

Figure 16. Siemens stars fits for SMLM **(a)** and SIMFLUX **(b)**, for single and multi emitter, at the following active emitter densities = 0.1, 1 and 5 emitters/μm^2. The increase in emitter recall rate and structure continuity, due to the extension form single to multi emitter approach is evidently visible.

By visual inspection and analysis of the obtained results of Siemens star and three-ring fitting, it clearly shows that at high active emitter densities, the features of the structure can be better resolved with the multi-emitter methods. The achieved recall fractions are approximately the same.

4. Discussion

We presented Multi-SIMFLUX, a novel multi-emitter maximum likelihood based structured illumination localization microscopy algorithm. Multi-SIMFLUX performs exceptionally well for the various simulated imaging conditions for sparse as well as for dense active emitter data.

In section 3.1, analytical expressions for the expected theoretical improvement factor are defined and validated by numerical simulations. The effect of emitter photon count and background intensity on localization performance in terms of precision, accuracy and recall fraction is evaluated. The considered emitter intensities during the simulations, ranged from $10^2 - 10^5$ $photons$ and the background intensity from $5 - 50$ $photons/pixels$. The obtained findings are consistent with our theoretical expectations, which was having a loss in localization precision by increasing background intensities, since the presence of noise leads to an increase in the uncertainty of the emitter's location. As theoretically expected, a significant improvement of SIMFLUX over SMLM is observed. SIMFLUX outperforms normal SMLM, in terms of localization precision and accuracy, for various emitter densities and intensities, with an improvement factor of approximately ~ 2, as can be seen from Figures 3 to 5 and Supplementary Figures A.4 to A.6.

In section 3.2, we considered multi-hypothesis testing, to evaluate the theoretical probability of making an emitter quantification error. We considered the case where we wish to distinguish between six hypotheses $\{H_0, H_1, \ldots, H_5\}$. Such a problem arises in case of the classification of the number of emitters, i.e. deciding how many active emitters there are within a certain ROI. The hypothesis H_0, suggests that there are no active emitters in a given ROI (i.e. only background noise), H_1 suggests that there is one active emitter, and so on. It is noticed that the probability error P_e increases with the number of emitters E within a ROI for the three different imaging cases: increasing separation distances, different emitter- and background intensities. As theoretically expected and confirmed by simulations, increasing the emitter intensity and/or separation distance decreased the P_e, while increasing background intensity increased the P_e. The obtained results for the three cases are shown in the Figures 7, A.11 and A.12, respectively. We found that based on overlap between log-likelihood density functions, SIMFLUX did not provide significant improvement over SMLM in terms of probability of correct decision P_c.

In section 3.3, we demonstrated how the separation distance d affects the Fisher information. A series of simulated images of two emitters, with increasing separation distances between their centers, were generated for different values of σ_{PSF}. The results are shown in Figure 8, where it can be seen that at a separation distance of approximately $d \approx 7\sigma_{PSF}$, the amount of Fisher information does not increase anymore for the different PSF widths. Then, we evaluated the ability of the algorithms to distinguish two nearby emitters, equivalent in intensity, with increasing separations between their centers. The impact of separation distance on the theoretical localization precision (CRLB) for different signal photon counts and background intensities are displayed in Supplementary Figures A.8 to A.9. Note that due to imperfect modulation the localization precision of SIMFLUX is position dependent. The obtained recall fraction results are shown in Figure 9. As theoretically expected, the recall fraction for both algorithms increases with larger separation distances, higher emitter intensities and lower background intensities. At very small separation distances ($\leq 0.15\ \mu m \approx \sigma_{PSF}$), for both algorithms the recall fraction is in the range of $\sim 40 - 60\%$. This has to do with the fact that the algorithms "see" the two emitters as just one emitter with double the intensity. For these small separation distances ($\leq \sigma_{PSF}$), SIMFLUX achieves a slightly higher recall fraction for the different evaluated emitter- and background intensities, compared to SMLM. However, at larger separation distances the performance is equal or even slightly more in favor of SMLM.

In section 3.4, we evaluated the localization performance of multi-SIMFLUX on simulated data for various active emitter densities and compared its performance against SMLM. Various ROI-sizes, ranging from $5\sigma_{PSF}$ to $8\sigma_{PSF}$ for single-emitters and $8\sigma_{PSF}$ to $20\sigma_{PSF}$ for multi-emitter, were evaluated in the terms of recall fraction, Jaccard Index, localization precision and accuracy (RMSE). By evaluating the algorithms for different ROI-sizes, slight differences were noticed. Smaller ROI-sizes perform better on the quantitative metrics (recall fraction and Jaccard Index) for single-emitter cases, while larger ROI-sizes tend to give more accurate and precise results, i.e. better qualitative results. For the multi-emitter case, smaller ROI-sizes showed a loss in quantitative and qualitative. After taking both qualitative and quantitative metrics into consideration, we found that for the single-emitter case a ROI-size of $6\sigma_{PSF}$ shows the best performance, while for the multi-emitter case a ROI-size of $15\sigma_{PSF}$ resulted in the best compromise between both metrics (Figure 13). With the multi-emitter SIMFLUX approach, we certainly outperformed both single-emitter approaches at higher active emitter densities. We were able to averagely double the recall fraction, increase the localization accuracy with $\sim 10\%$ while suffering from a slight degradation in precision, approximately $\sim 20\%$.

In section 3.5, the performance of SMLM and SIMFLUX on the reconstruction of the three-ring structure (Figure A.21) and Siemens star (Figure 15) is investigated. The aim is to benchmark the performance of both algorithms against each other in terms of recall fraction, accuracy and the continuity of the obtained structures for varying active emitter frame densities. From tables 1 to 3 and Figures 14 and 16, we can conclude that with the multi-emitter approach we are able to averagely double the recall fraction for mid densities and triple it (or even more) for high densities, with only a slight deterioration in localization precision, compared to single emitter approaches. In terms of localization precision SIMFLUX outperforms SMLM for all the considered frame densities, for the single- and multi-emitter case. The achieved localization precision improvement factor of SIMLFLUX over SMLM decreases with increasing active emitter density. Throughout the considered frame densities the localization improvement factor stays in the range of $\sim 1.1-2.0$. In terms of recall fraction SMLM slightly outperforms SIMFLUX for low and mid densities; however, for high densities SIMFLUX shows a slight advantage.

Author Contributions

C. Smith, J. Cnossen and A. Zahran developed the SIMFLUX multi-emitter method. J. Cnossen wrote the largest chunk of the processing pipeline code for SIMFLUX and the $2D$-Gaussian approach, A. Zahran extended it to the multi-emitter approach and wrote some code for the performed simulations and data analysis. C. Smith and J. Cnossen directed and supervised the research. A. Zahran wrote the paper with support and comments received from all authors.

5. Conclusion

The Multi-SIMFLUX method we have developed, enhances super-resolution reconstructions by improving the detection rate while averagely maintaining the localization precision compared to single molecule localization techniques. It is able to double the localization precision in comparison with conventional $2D$ Gaussian multi-emitter SMLM algorithms at low active emitter densities and maintains a slight localization precision improvement at higher densities. Our approach has shown to perform well in theory and on simulations. We foresee a bright future for its implementation on real experimental data. Higher density imaging permits shorter acquisition times, however it results in more computational complexity in analysis and a huge dependence on hard- and software tools.

References

[1] S. W. Hell and J. Wichmann, *Breaking the diffraction resolution limit by stimulated-emission—stimulated emission- depletion fluorescence microscopy* (Opt. Lett. 19, 780–782., 1994).

[2] M. D. A. E. Thomas A. Klar, Stefan Jakobs and S. W. Hell, *Fluorescence microscopy with diffraction resolution barrier broken by stimulated emission* (Proceedings of the National Academy of Sciences, vol. 97, pp. 8206–8210, 2000).

[3] *Nonlinear structured-illumination microscopy: wide-field fluorescence imaging with theoretically unlimited resolution* (Proc. Natl. Acad. Sci. USA, PubMed: 16141335, 2005).

[4] M. G. L. Gustafsson, *Surpassing the lateral resolution limit by a factor of two using structured illumination microscopy* (HORT COMMUNICATION," Journal of Microscopy, vol. 198, pp. 82–87, 2000).

[5] F. Ströhl and C. F. Kaminski, *Frontiers in structured illumination microscopy* (Optica, vol. 3, p. 667, 2016).

[6] B. E. et al., *Imaging intracellular fluorescent proteins at nanometer resolution* (PubMed, 2006).

[7] H. Shroff, H. White, and E. Betzig, *Photoactivated Localization Microscopy (PALM) of Adhesion Complexes* (NCBI PMC, 2013).

[8] B. Huang, M. Bates, and X. Zhuang, *Super resolution fluorescence microscopy* (NCBI PMC, 2014).

[9] M. J. Rust, M. Bates, and X. Zhuang, *Sub-diffraction-limit imaging by stochastic optical reconstruction microscopy (STORM)* (Nat. Methods 3, 793, 2006).

[10] F. Balzarotti, Y. Eilers, K. Gwosch, A. Gynnå, V. Westphal, F. Stefani, J. Elf, and S. Hell, *Nanometer resolution imaging and tracking of fluorescent molecules with minimal photon fluxes* (Science.;355(6325):606-612 [PubMed], 2016).

[11] J. Cnossen, T. Hinsdale, R. Thorsen, F. Schueder, R. Jungmann, C. S. Smith, B. Rieger, and S. Stallinga, *Localization microscopy at doubled precision with patterned illumination* (BioRxiv, 2019).

[12] S. Cox, E. Rosten, J. Monypenny, T. Jovanovic-Talisman, D. T. Burnette, J. Lippincott-Schwartz, G. E. Jones, and R. Heintzmann, *Bayesian localisation microscopy reveals nanoscale podosome dynamics* (Nature Methods, 9, 2, 195-200, 2012).

[13] J. Min, C. Vonesch, H. Kirshner, L. Carlini, N. Olivier, S. Holden, S. Manley, J. C. Ye, and M. Unser, *FALCON: fast and unbiased reconstruction of high-density super-resolution microscopy data* (Scientific Reports, 4, 4577, 2014).

[14] M. Fazel, M. J. Wester, H. Mazloom-Farsibaf, M. B. M. Meddens, A. S. Eklund, T. Schlichthaerle, F. Schueder, R. Jungmann, and K. A. Lidke, *Bayesian Multiple Emitter Fitting using Reversible Jump Markov Chain Monte Carlo* (Scientific Reports 9, 13791 doi:10.1038/s41598-019-50232-x, 2019).

[15] F. Huang, S. L. Schwartz, J. M. Byars, and K. A. Lidke, *Simultaneous multiple-emitter fitting for single molecule super-resolution imaging* (OSA Publishing, 2016).

[16] C. S. Smith, N. Joseph, B. Rieger, and K. A. Lidke, *Fast, Single-Molecule Localization that Achieves Theoretically Minimum Certainty* (Nature Methods, 2010).

[17] S. Stallinga and B. Rieger, *Accuracy of the Gaussian Point Spread Function model in 2D localization microscopy* (Optics Express Vol. 18, Issue 24, pp. 24461-24476, 2010).

[18] S. M.Kay, *Fundamentals of statistical signal processing: estimation theory* (Prentice-Hall, Englewood Cliffs, NJ, USA, 1998).

[19] R. J. Ober, S. Ram, and E. Ward, *Localization Accuracy in Single-Molecule Microscopy* (Biophys., 2004).

[20] P. Stoica and T. L. Marzetta, *Parameter Estimation Problems with Singular Information Matrices* (IEEE TRANSACTIONS ON SIGNAL PROCESSING, VOL. 49, NO. 1, 2001).

[21] Y.-H. Li and P.-C. Yeh, *An Interpretation of the Moore-Penrose Generalized Inverse of a Singular Fisher Information Matrix* (EEE Transactions on Signal Processing, vol. 60, no. 10, pp. 5532-5536, 2010).

[22] T. A. Laurence and B. A. Chromy, *Efficient maximum likelihood estimator fitting of histograms* (Nature, 2010).

[23] W. H. Press, S. A. Teukolsky, W. T. Vetterling, and B. P. Flannery, *Numerical Recipes in C, The Art of Scientific Computing* (Cambridge University Press, second edition,, 1992).

[24] C. C.Ford and J. Eisenfeld, *Some unresolved questions pertaining to the mathematical analysis of fluorescence decay data* (Applied nonlinear analysis, 1979).

[25] P. MucCullagh and J. Nelder, *Generalized linear models. 2nd Edition* (Chapman and Hall, 1989).

[26] H. Deschout, F. C. Zanacchi, M. Mlodzianoski, A. Diaspro, J. Bewersdorf, S. T. Hess, and K. Braeckmans, *Precisely and accurately localizing single emitters in fluorescence microscopy* (Nature Methods 11, 253, 2014).

[27] R. P. N. Bernd Reiger and S. Stallinga, *Image Processing and Analysis for Single-Molecule Localization Microscopy* (IEEE Signal Processing Magazine, V. 32, I. 1, 49 - 57, 2014).

[28] B. Zhang, J. Zerubia, and J.-C. Olivo-Marin, *Gaussian approximations of fluorescence microscope point-spread function models* (OSA Publishing Applied Optics Vol. 46, Issue 10, pp. 1819-1829, 2007).

A. Supplementary Figures

A.1 Examples of simulated single-molecule ROIs as used in simulations with varying background intensity on the horizontal axis and varying emitter intensity on the vertical axis. . . . 33
A.2 Example of a ROI with 5 emitters at constant positions . . . 33
A.3 Multi-emitter optimization schematic representation of the multi initial estimate approach described in Section 2.3, from the imaging frames as input and results as output. . . . 34
A.4 Histograms of the obtained localization errors in the x-direction for SMLM and SIMFLUX . . . 35
A.5 The effect of the active emitter density and background intensity on the two-dimensional localization accuracy of the SMLM and SIMFLUX algorithm. . . . 36
A.6 Cumulative distribution of the obtained localization error by SMLM and SIMFLUX for random emitter positions. . . . 37
A.7 Impact of separation distance on the theoretical localization precision (CRLB) for different signal photon counts. . . . 38
A.8 Impact of separation distance on the localization precision for different background intensities. . . . 38
A.9 A map of the position dependence of SIMFLUX and SMLM in terms of recall fraction, precision and accuracy. . . . 39
A.10 The effect of emitter intensity on probability error of SIMFLUX, for single and multi emitters. . . . 40
A.11 Examples of ROIs for different numbers of emitters and emitter intensities. . . . 40
A.12 Impact of background intensity on probability error. . . . 41
A.13 Examples of ROIs for different numbers of emitters and background intensities. 41
A.14 Examples of ROIs for different numbers of emitters and for separation distances w.r.t. ROI-center. . . . 42
A.15 Multi-emitter log-likelihood fit results for different number of emitters. . . . 42
A.16 ROI fitting visualisation for 2 to 4 emitters. . . . 43
A.17 The effect of separation distance between emitters on the fitting results of SMLM and SIMFLUX. . . . 44
A.18 The impact of active emitter density on the Jaccard Index for single and multi-emitters for different ROI sizes. . . . 45
A.19 The impact of active emitter density on the RMSE for single and multi-emitters for different ROI sizes. . . . 45
A.20 The improvement factor of SIMFLUX over $2D$ Gaussian SMLM, for localization precision and accuracy (RMSE), as a function of active emitter density. . . . 46
A.21 Three-ring frame configuration . . . 47
A.22 Examples of simualted ring frames for normal $2D$ SMLM at different frame densities. . . . 47
A.23 Examples of simulated ring frames for SIMFLUX at different frame densities. . 47
A.24 Examples of detected and fitted ROIs for different active emitter densities. . . . 48
A.25 Impact of the LM parameter λ on the localization precision for SMLM and SIMFLUX. . . . 49
A.26 Impact of the LM parameter λ on the χ^2- test and localization precision for SMLM and SIMFLUX. . . . 49
A.27 $3D$ Visualisation of the maximum likelihood estimation optimization landscape 50
A.28 Estimator localization convergence. . . . 51

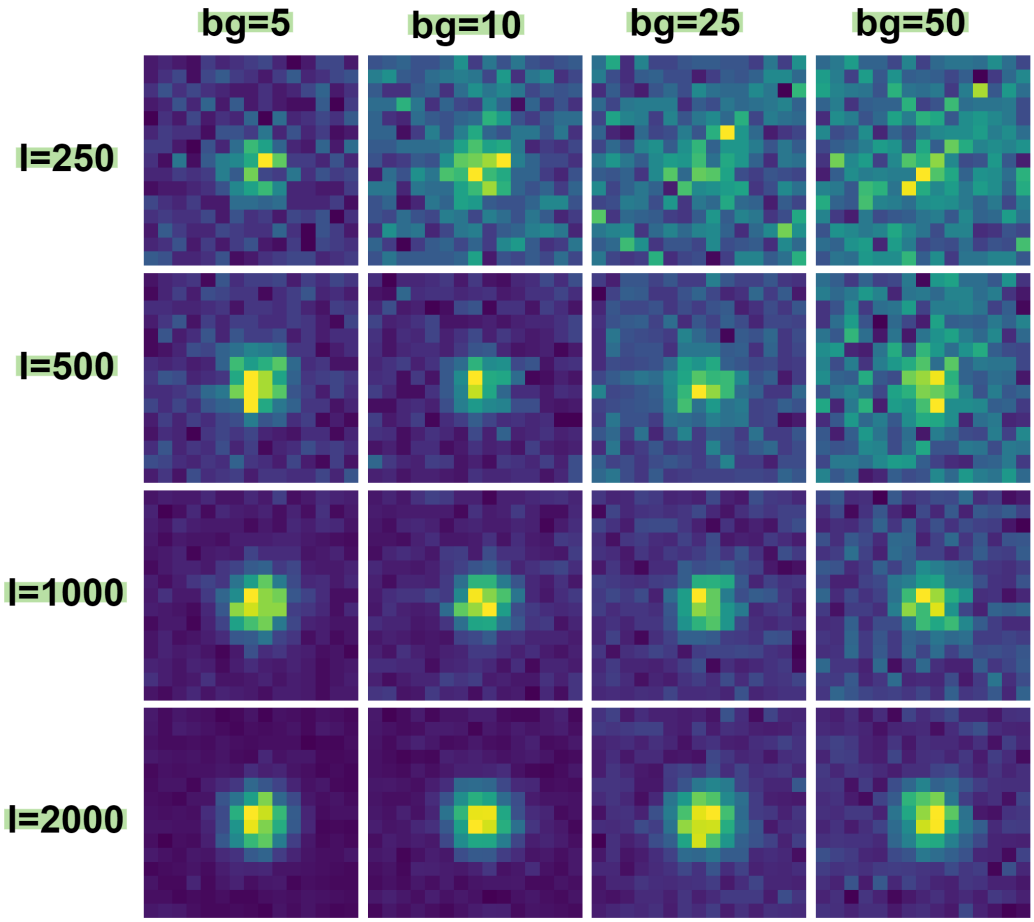

Figure A.1. Examples of simulated single-molecule ROIs as used in simulations with varying background intensity on the horizontal axis and varying emitter intensity on the vertical axis.

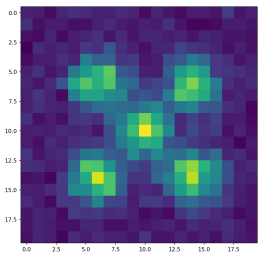

Figure A.2. Example of a ROI with 5 emitters at constant positions $[\theta_{x_1}, \theta_{y_1}, \theta_{x_2}, \theta_{y_2}, \theta_{x_3}, \theta_{y_3}, \theta_{x_4}, \theta_{y_4}, \theta_{x_5}, \theta_{y_5}]^\intercal = [\frac{ROI_{size}}{2}, \frac{ROI_{size}}{2}, \frac{ROI_{size}}{2} + d, \frac{ROI_{size}}{2} + d, \frac{ROI_{size}}{2} - d, \frac{ROI_{size}}{2} - d, \frac{ROI_{size}}{2} + d, \frac{ROI_{size}}{2} - d, \frac{ROI_{size}}{2} - d, \frac{ROI_{size}}{2} + d]^\intercal$, for d being equal to 3 pixels. Note that an deviation of ± 1.5 *pixel* for each emitter location is allowed.

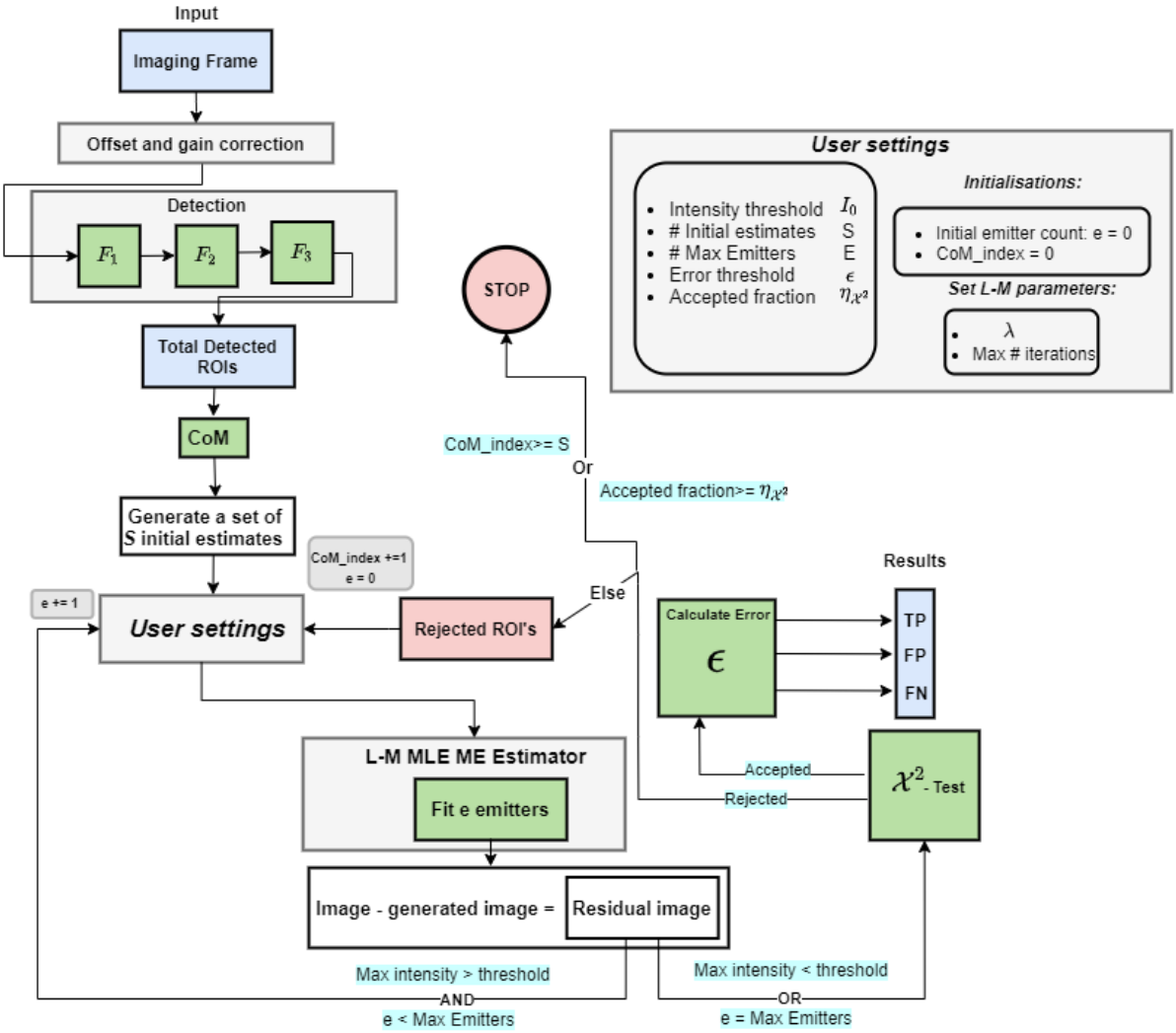

Figure A.3. Multi-emitter optimization schematic representation of the multi initial estimate approach described in Section 2.3, from the imaging frames as input and results as output.

In some cases, the localization precision is expressed by the full-width at half maximum (FWHM) of the distribution of measured position coordinates, which is defined as follows[26]:

$$FWHM_x = 2\sigma_x\sqrt{2ln(2)}$$

The same expression holds for the position coordinates of the y-direction. Only the localization error in the x-direction is included here, since the localization precision in both directions was roughly the same.

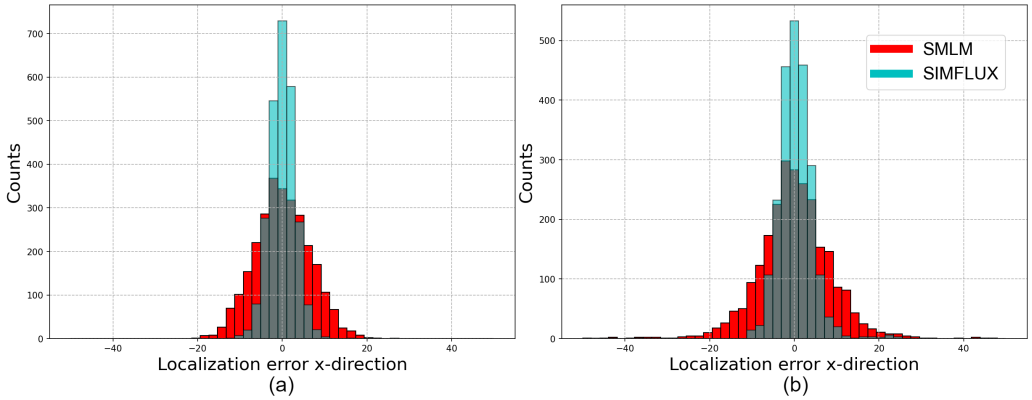

Figure A.4. Histograms of the obtained localization errors in the x-direction for SMLM and SIMFLUX for emitter and background intensity $\theta_I = 1000\ photons$ and $\theta_{bg} = 5\ photons/pixel$, respectively. **(a)** For single emitters (E=1) SMLM achieved an $FWHM_x$ of $14.7 \pm 0.9\ nm$, while SIMFLUX achieved $7.3 \pm 0.2\ nm$, indicating an improvement factor of ~ 2. **(b)** For multi emitters (E=4) SMLM achieved an $FWHM_x$ of $25.4 \pm 1.6\ nm$, while SIMFLUX achieved $13.9 \pm 0.6\ nm$, indicating an improvement factor of ~ 1.8.

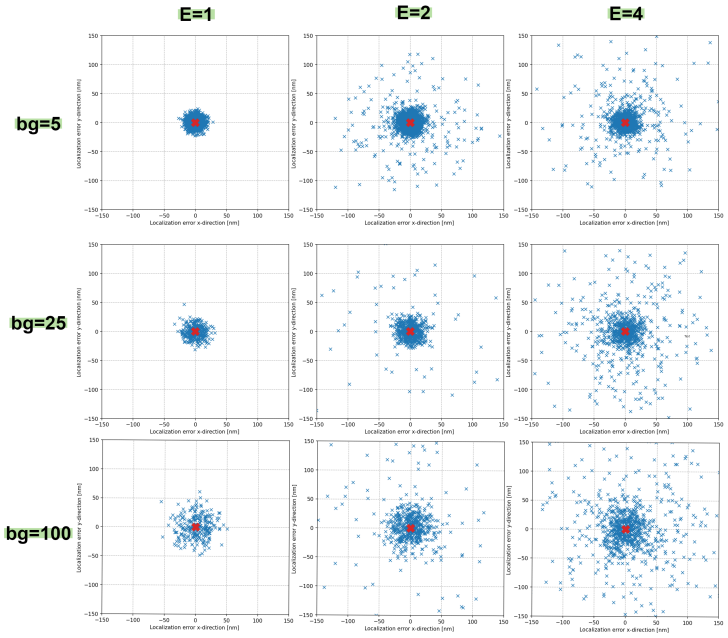

(a)

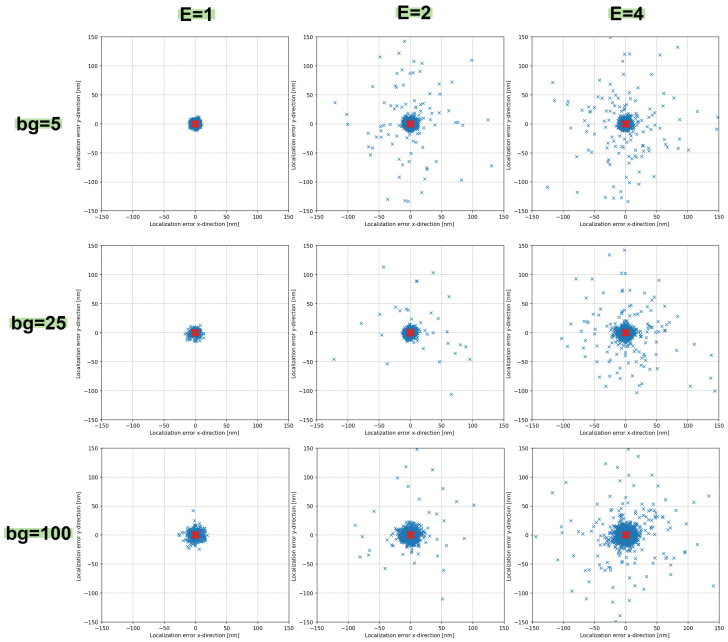

(b)

Figure A.5. The effect of the active emitter density and background intensity on the two-dimensional localization accuracy of the SMLM algorithm **(a)** and SIMFLUX **(b)**. The emitter density per ROI increases from left to right, while the background intensity increases from top to bottom. The active emitter density and background intensity, do clearly affect the localization accuracy. Higher emitter density affects the accuracy more negatively than increasing background intensity does. For instance keeping the background intensity at $\theta_{bg} = 25\ photons/pixel$, while increasing the number of emitters (second row), results in a greater performance loss compared to the scenario of keeping the number of emitters constant at $E = 1$ and increasing the background intensity (first column). It can also be notated that the performance deterioration, due to higher background intensity and/or higher active emitter density, is less for SIMFLUX.

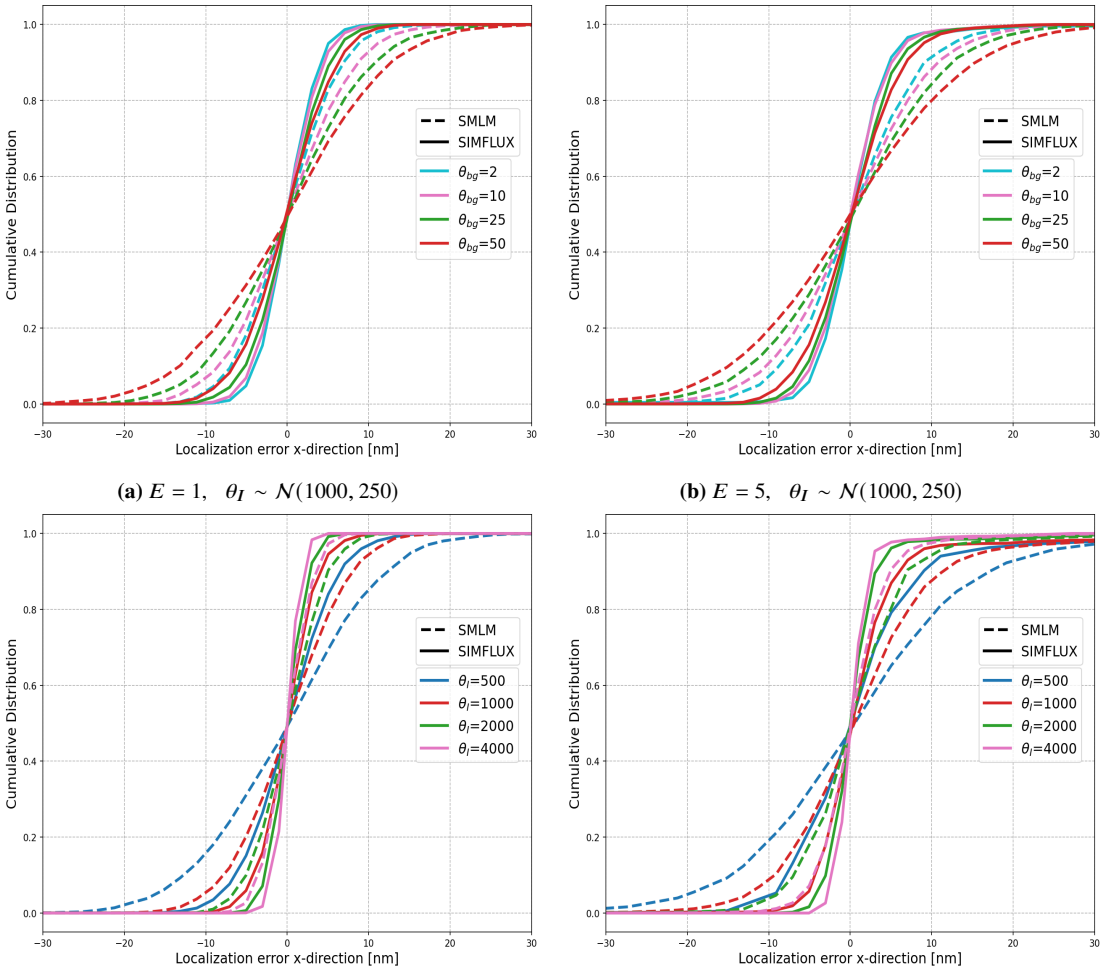

(a) $E = 1, \quad \theta_I \sim \mathcal{N}(1000, 250)$

(b) $E = 5, \quad \theta_I \sim \mathcal{N}(1000, 250)$

(c) $E = 1, \quad \theta_{bg} = 5\ photons/pixel$

(d) $E = 5, \quad \theta_{bg} = 5\ photons/pixel$

Figure A.6. Cumulative distribution of the obtained localization error (x-direction) by SMLM and SIMFLUX for random emitter positions. SIMFLUX outperforms SMLM for various emitter- and background intensities, for both single and multi emitters. **(a-b)** Impact of background intensity on the localization error , of SMLM and SIMFLUX, for single ($E = 1$) and multi emitters ($E = 5$). **(c-d)** Impact of emitter intensity on the localization error, of SMLM and SIMFLUX, for single and multi emitters.

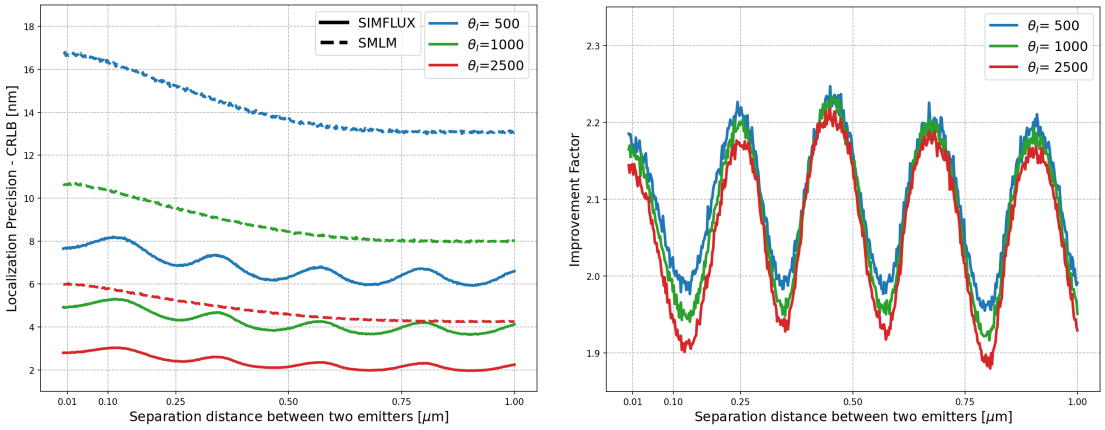

(a) **(a)**

Figure A.7. **(a)** Impact of separation distance on the theoretical localization precision (CRLB) for different signal photon counts. Note that due to imperfect modulation the localization precision of SIMFLUX is position dependent. SIMFLUX achieves slightly better localization precision at the center of the illumination pattern maximum. **(b)** Improvement factor of SIMFLUX over SMLM as a function of separation distance for different emitter intensities, indicating an improvement factor in the range of $\sim 1.9 - 2.25$. Note that the average improvement factor slightly increases for lower signal photon counts.

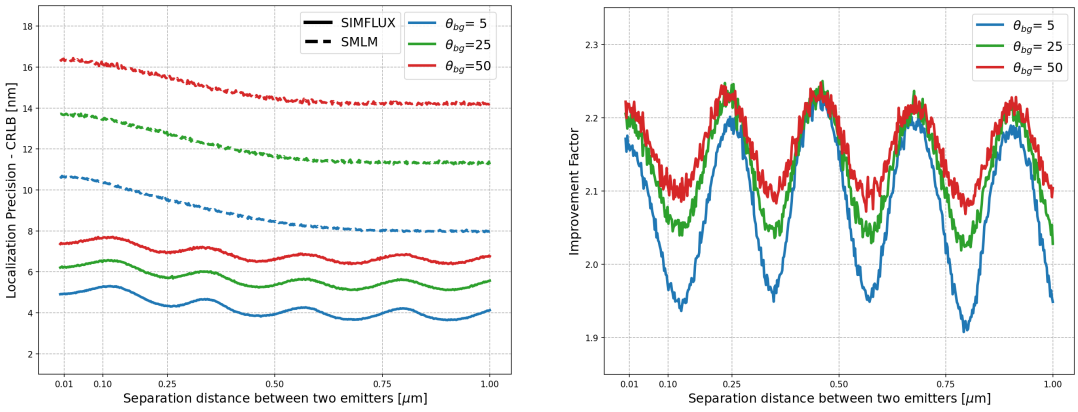

(a) **(b)**

Figure A.8. **(a)** Impact of separation distance on the localization precision for different background intensities. **(b)** Improvement factor of SIMFLUX over SMLM as a function of separation distance for different background intensities, indicating an improvement factor in the range of $\sim 1.95 - 2.25$. Note that the average improvement factor slightly increases for increasing background intensities.

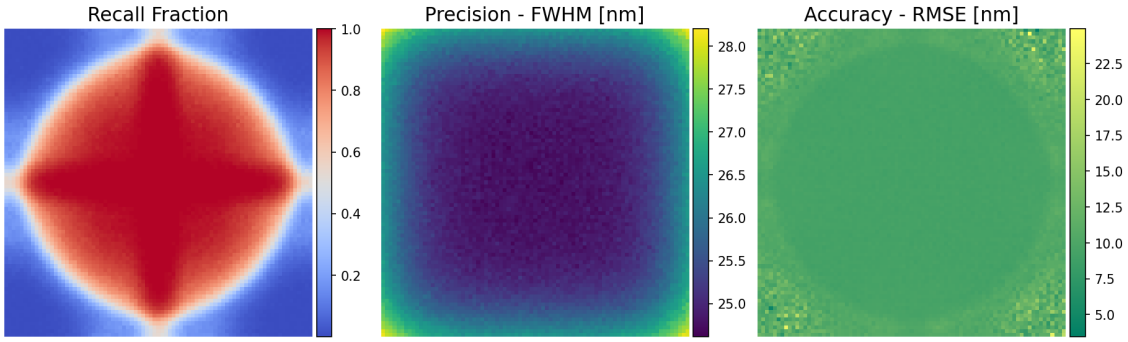

(a) SMLM

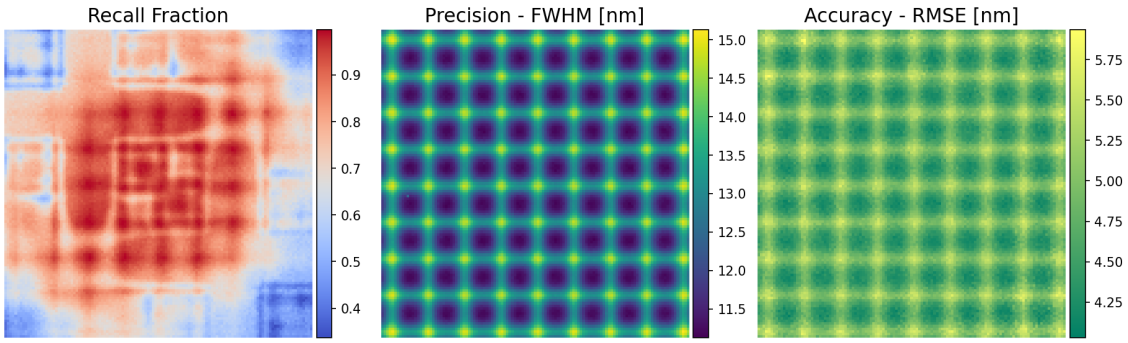

(b) SIMFLUX

Figure A.9. A map of the position dependence of SIMFLUX and SMLM in terms of Recall fraction, precision (FWHM) and accuracy (RMSE). The ROI-size is held constant at $8\sigma_{PSF} \times 8\sigma_{PSF}$. The expected photon count per emitter is selected from a normal distribution with $\theta_I \sim \mathcal{N}(1000, 250)$ and the background intensity of the image θ_{bg} is set to 5 $photons/pixel$. Note that the recall fraction is higher in the center of the ROI, with some non-uniformity for SIMFLUX due tot multiple local minima. Furthermore, SMLM achieves high localization precision n the center, while for SIMFLUX the precision is dependent on the position w.r.t. the illumination patterns.

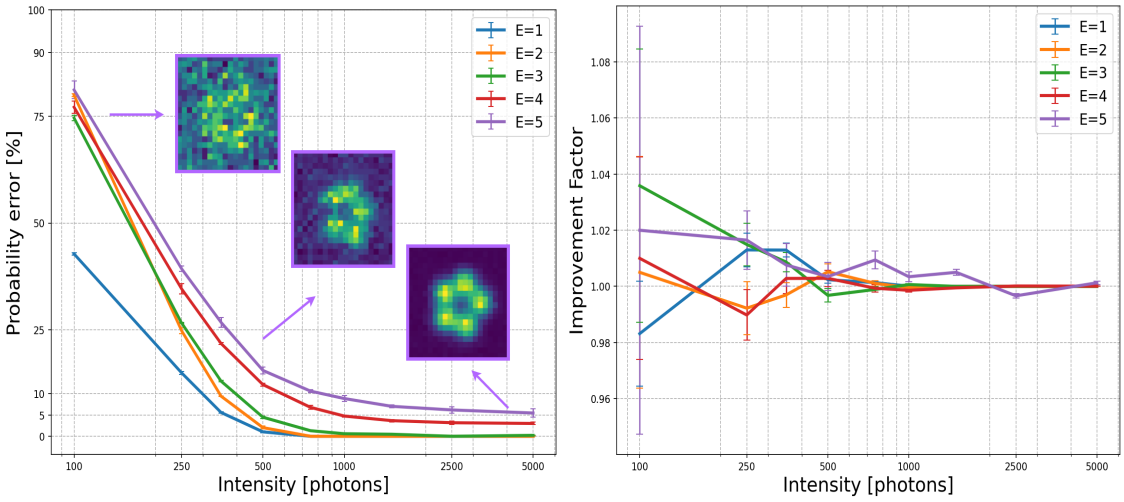

(a) **(b)**

Figure A.10. **(a)** The effect of emitter intensity on probability error of SIMFLUX, for single and multi emitters, under constant background intensity $\theta_{bg} = 5\ photons/pixel$ and a constant normalized separation distance $\frac{r}{\sigma_{PSF}} = 2.5$. Note that at constant θ_I the probability error P_e increases with the number of emitters E within a ROI. A visualisation is shown for $E = 5$, see Figure A.11 for further visualisation. **(b)** The ratio between SIMFLUX and SMLM in the probability of making the correct decision $(\frac{P_{c,SIMFLUX}}{P_{c,SMLM}})$ at different emitter intensities. At low photon counts ($\leq 500\ photons$), the improvement factor compared to SMLM alternates between $\sim [-2, 4]\%$, while at higher photon counts the performance in terms of correct decision is roughly the same. SIMFLUX does not provide significant improvement over SMLM in terms of P_c for the evaluated range of emitter intensities.

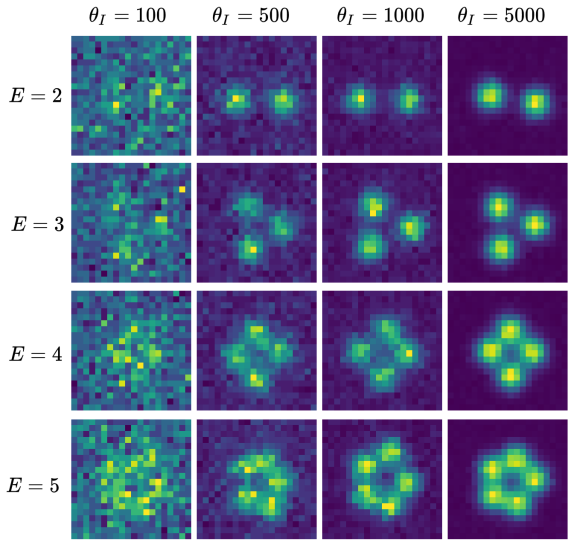

Figure A.11. Examples of ROIs for different numbers of emitters E, different emitter intensities θ_I, constant background intensity $\theta_{bg} = 5\ photons/pixel$ and a constant distance w.r.t. ROI-center normalized by $\sigma_{PSF}\ \frac{r}{\sigma_{PSF}} = 2.5$.

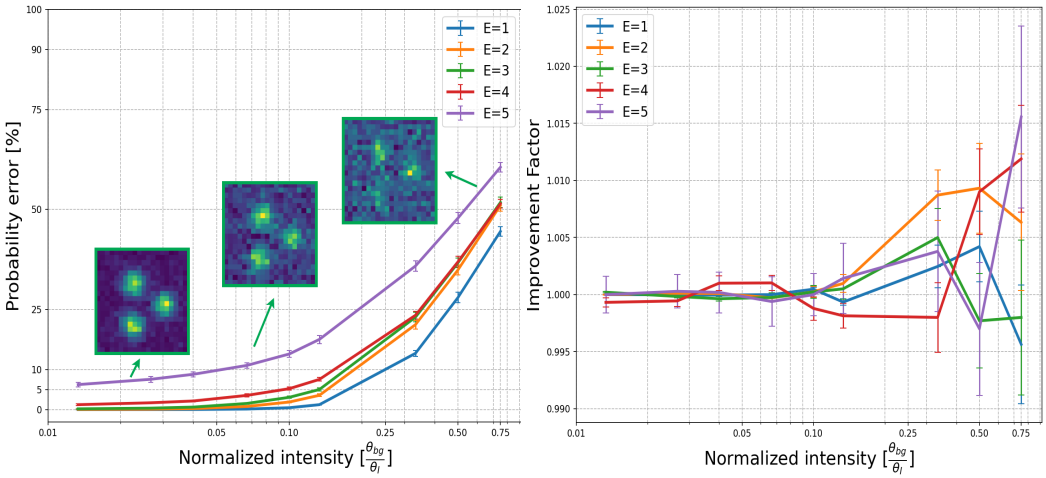

(a) **(b)**

Figure A.12. **(a)** Impact of background intensity on probability error under constant emitter intensity $\theta_I = 750\ photons$ and constant normalized separation distance $\frac{d}{\sigma_{PSF}} = 3$. Note that at constant $\frac{\theta_{bg}}{\theta_I}$ the probability error P_e increases with the number of emitters E within a ROI. A visualisation of the effect of background intensity on the ROI is shown for $E = 3$, see Supplementary Figure A.13 for further visualisation. **(b)** The ratio between the probability of making the correct decision of SIMFLUX and SMLM $\frac{P_{c,SIMFLUX}}{P_{c,SMLM}}$ at different background intensities. The obtained improvement factor is $\sim 1 \pm 1\%$. SIMFLUX does not provide significant improvement over SMLM in terms of P_c for the different evaluated background intensities.

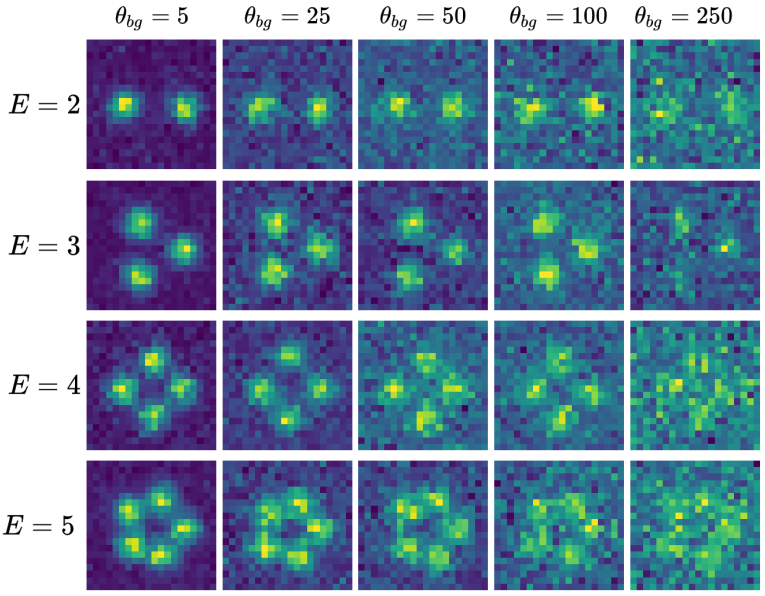

Figure A.13. Examples of ROIs for different numbers of emitters E, different background intensities θ_{bg}, constant emitter intensity $\theta_I = 750\ photons/pixel$ and a constant distance w.r.t. ROI-center normalized by σ_{PSF} $\frac{r}{\sigma_{PSF}} = 3$.

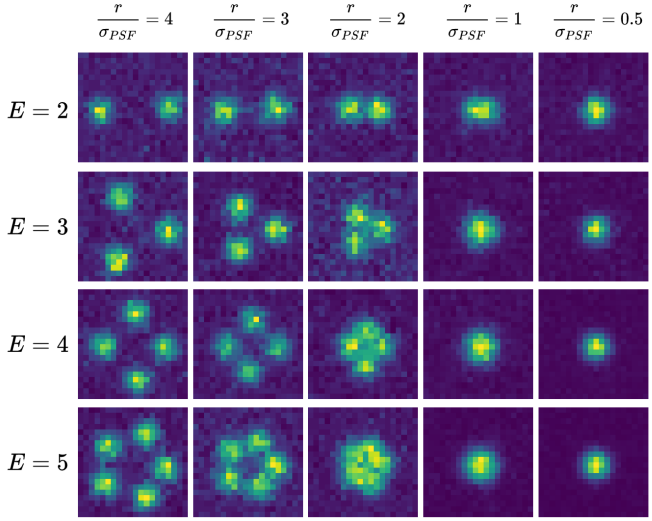

Figure A.14. Examples of ROIs for different numbers of emitters E, for different distances w.r.t. ROI-center normalized by σ_{PSF} ($\frac{r}{\sigma_{PSF}}$), a constant emitter and background intensity $\theta_I = 750\ photons/pixel$, $\theta_{bg} = 5\ photons/pixel$, respectively.

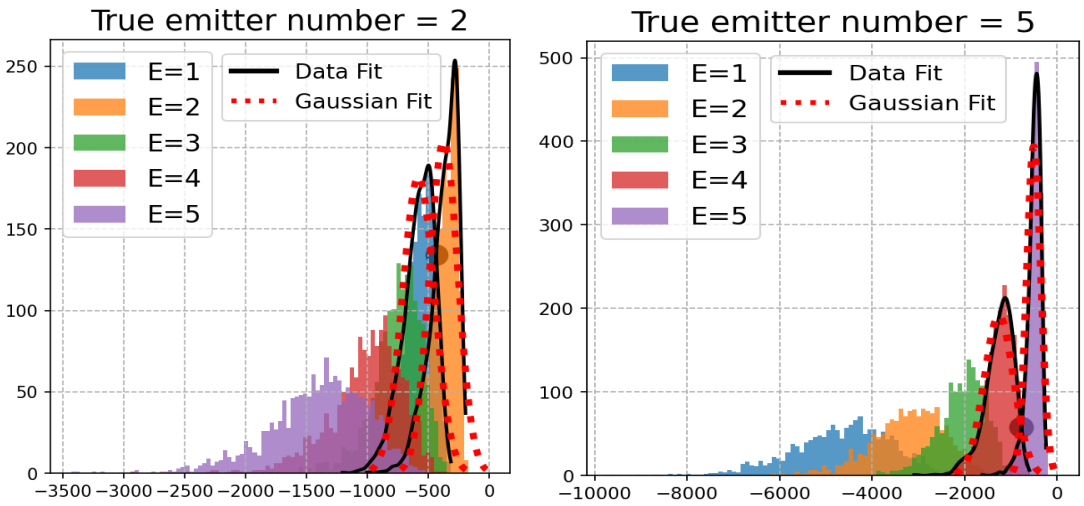

(a) **(b)**

Figure A.15. Multi-emitter log-likelihood fit results for different number of emitters. The Gaussian fit resulted in a small underestimation of the PDF, resulting in a relatively larger overlap area (i.e. higher probability error P_e). **(a)** Constant normalized distance w.r.t. ROI-center $\frac{r}{\sigma_{PSF}} = 1.5$, a constant emitter and background intensity $\theta_I = 500\ photons/pixel$, $\theta_{bg} = 5\ photons/pixel$, respectively. **(b)** Constant normalized distance w.r.t. ROI-center $\frac{r}{\sigma_{PSF}} = 2.5$, and a constant emitter and background intensity $\theta_I = 750\ photons/pixel$, $\theta_{bg} = 5\ photons/pixel$, respectively.

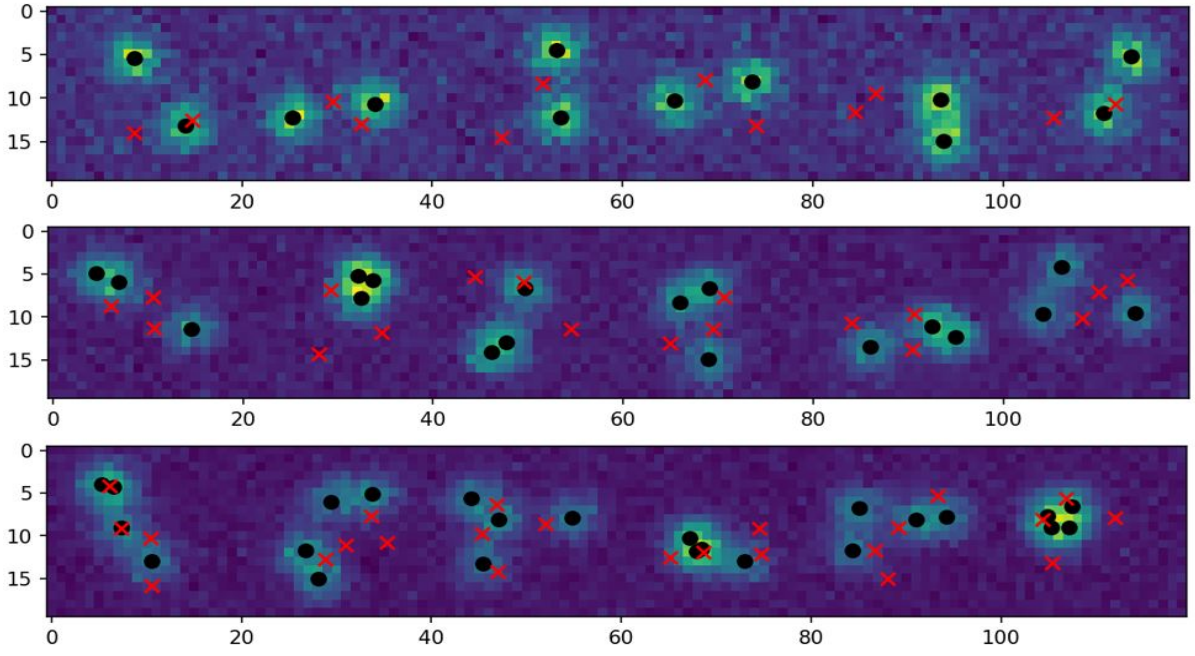

(a)

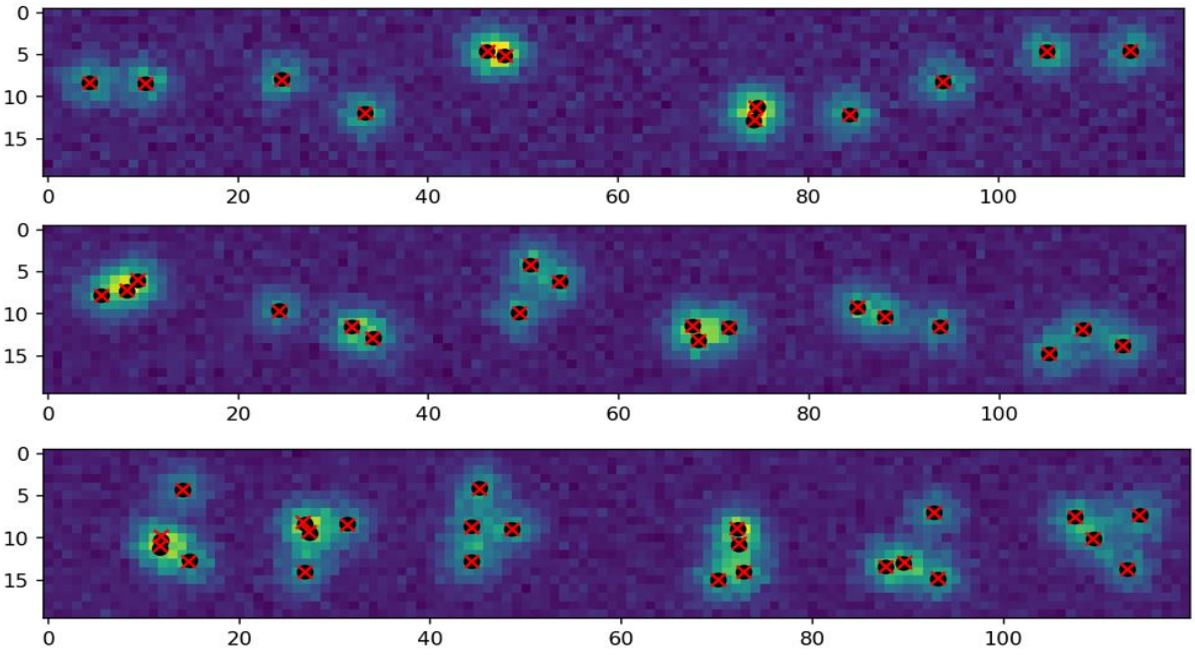

(b)

Figure A.16. ROI fitting visualisation for 2 to 4 emitters. **(a)** Examples of bad fitted ROIs - χ^2-test rejected ROIs. **(b)** Examples of good fitted ROIs - χ^2-test accepted ROIs.

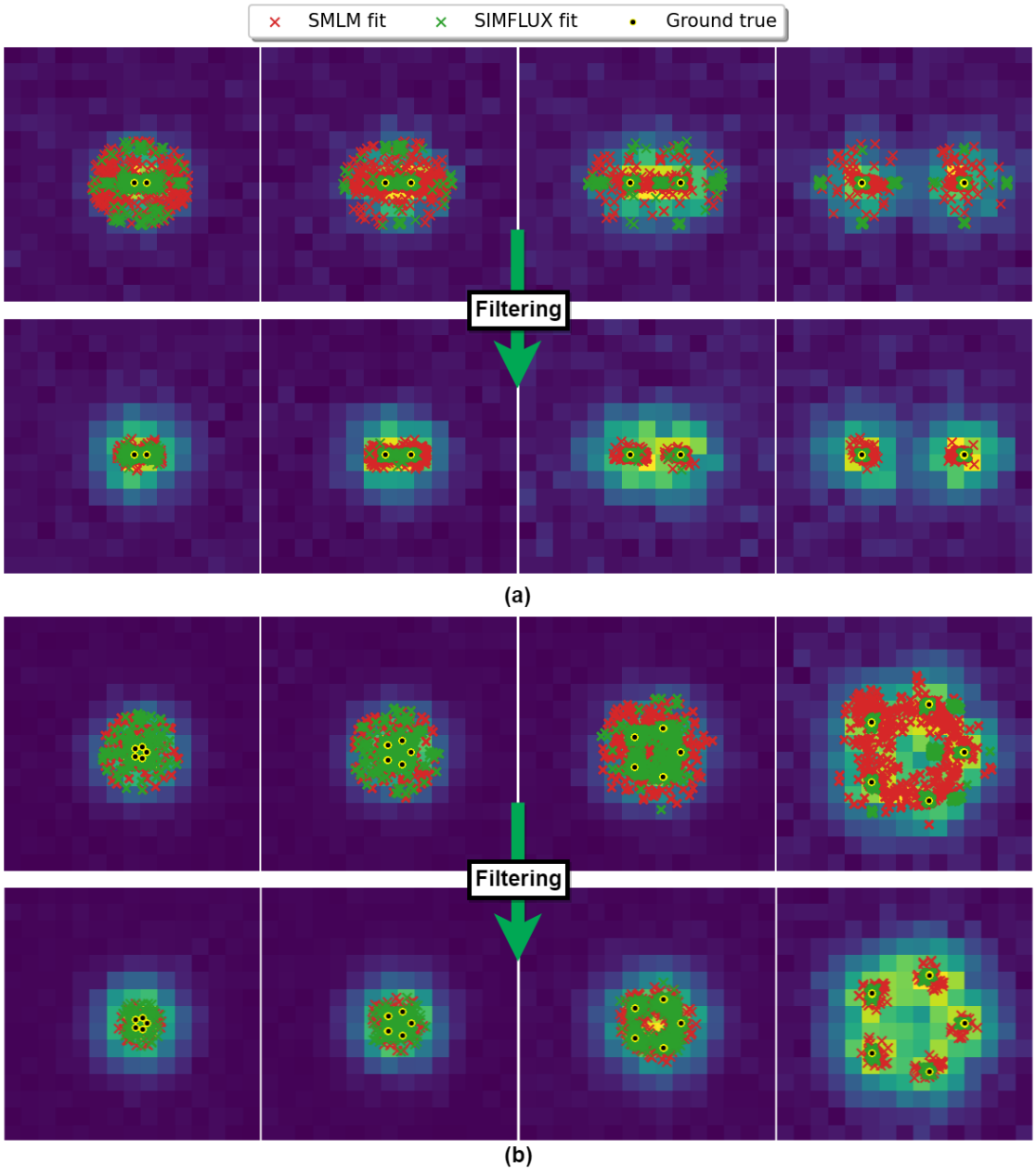

Figure A.17. A series of a total of 10^4 emitters is simulated with increasing separation distances w.r.t. the ROI-center ranging from $\{\frac{\sigma_{PSF}}{2}\ to\ 3\sigma_{PSF}\}$. The expected photon count per emitter is selected from a normal distribution with $\theta_I \sim \mathcal{N}(1000, 250)$, the background intensity of the image θ_{bg} is set to 5 $photons/pixel$. Note the obtained results are shown, then filtered where for fitting results with a localization error $\leq 0.1\ \mu m$ are regarded as good fits. **(a)** Fitting results for $E = 2$. **(b)** Fitting results for $E = 5$. The achieved localization precision improvement factor for SIMFLUX over SMLM is ~ 2.

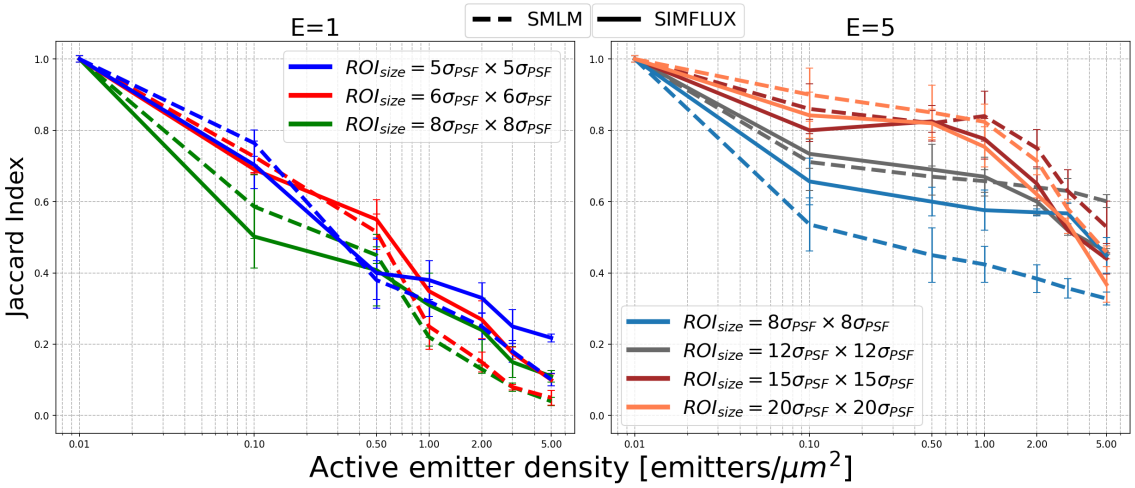

Figure A.18. The impact of active emitter density on the Jaccard Index for single and multi-emitters for different ROI sizes.

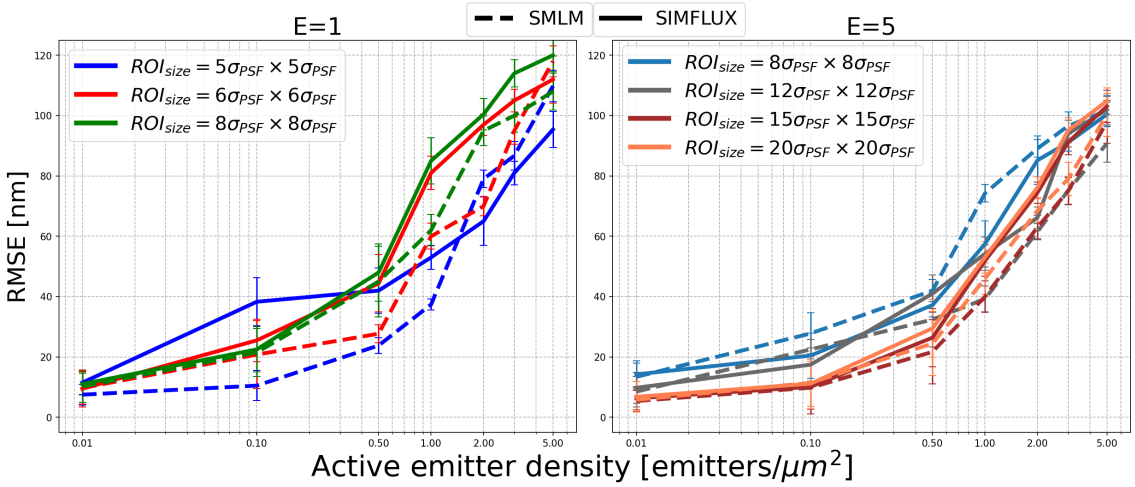

Figure A.19. The impact of active emitter density on the RMSE for single and multi-emitters for different ROI sizes.

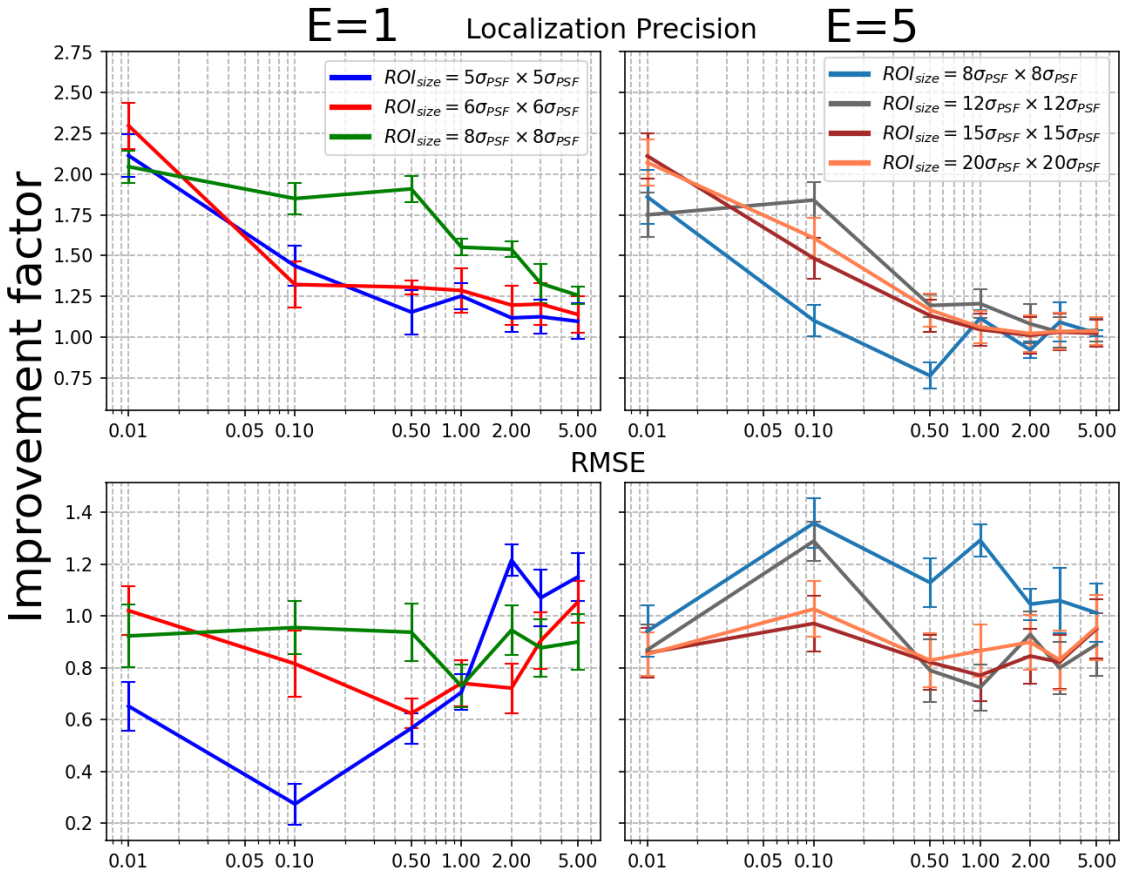

Figure A.20. The improvement factor of SIMFLUX over 2*D* Gaussian SMLM, for localization precision and accuracy (RMSE), as a function of active emitter density. **Top row:** at low active emitter densities SIMFLUX algorithm is able to double the localization precision compared to conventional SMLM algorithm. The localization improvement factor decreases with higher densities. For the single emitter case, SIMFLUX is still able to preserve an improvement factor of $\sim$ 20%, while for the multi-emitter case the localization precision is approximately the same.
Bottom row: for single emitters SMLM is slightly better than SIMFLUX in terms of accuracy, i.e. the bias between the estimated and true position is smaller($\sim$ 10%).

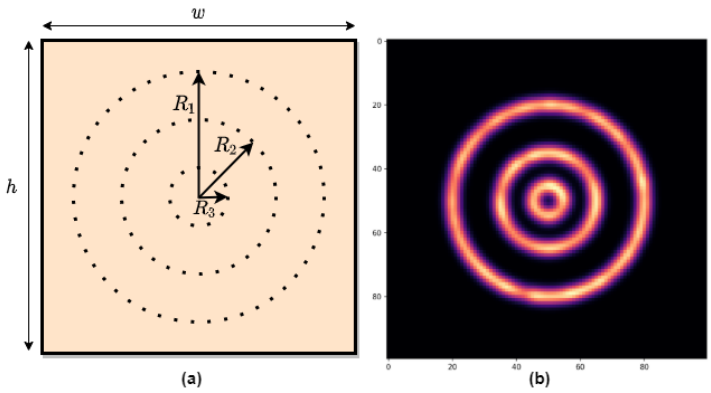

Figure A.21. Rings fitting frame. **(a)** Ring frame configuration. **(b)** Frame width = heigth$w = h = 10\ \mu m$, $R_1 = 3\ \mu m$, $R_2 = 1.5\ \mu m$, $R_3 = 0.5\ \mu m$.

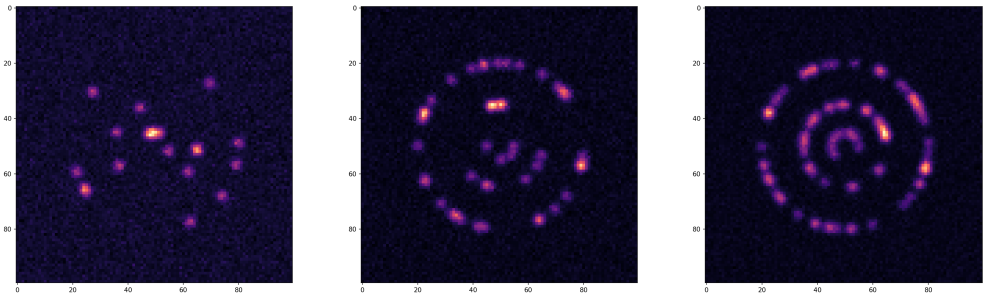

Figure A.22. Examples of simulated ring frames for normal SMLM - **Left:** $\sim$ 20 active emitters/frame. **Mid:** $\sim$ 50 active emitters/frame. **Right:** $\sim$ 100 active emitters/frame

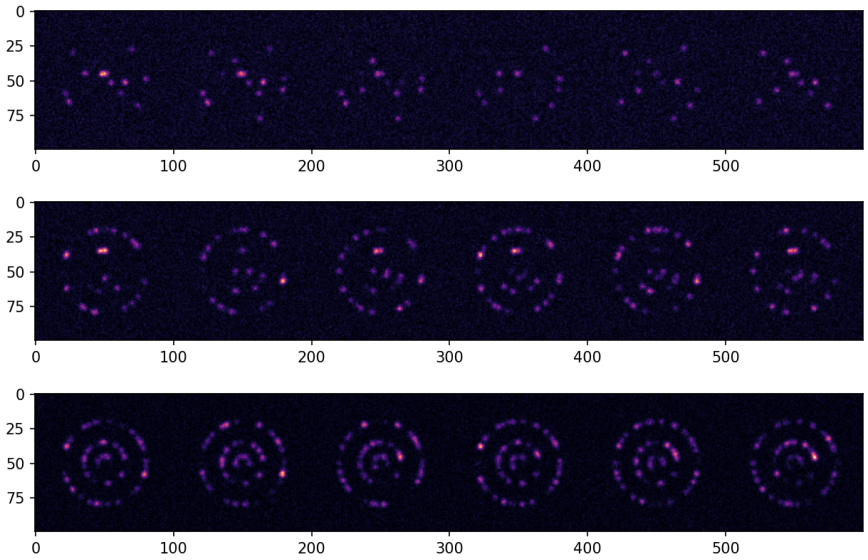

Figure A.23. Examples of simulated ring frames for SIMFLUX - **Top:** $\sim$ 20 active emitters/frame. Mid: $\sim$ 50 active emitters/frame. **Bottom:** $\sim$ 100 active emitters/frame.

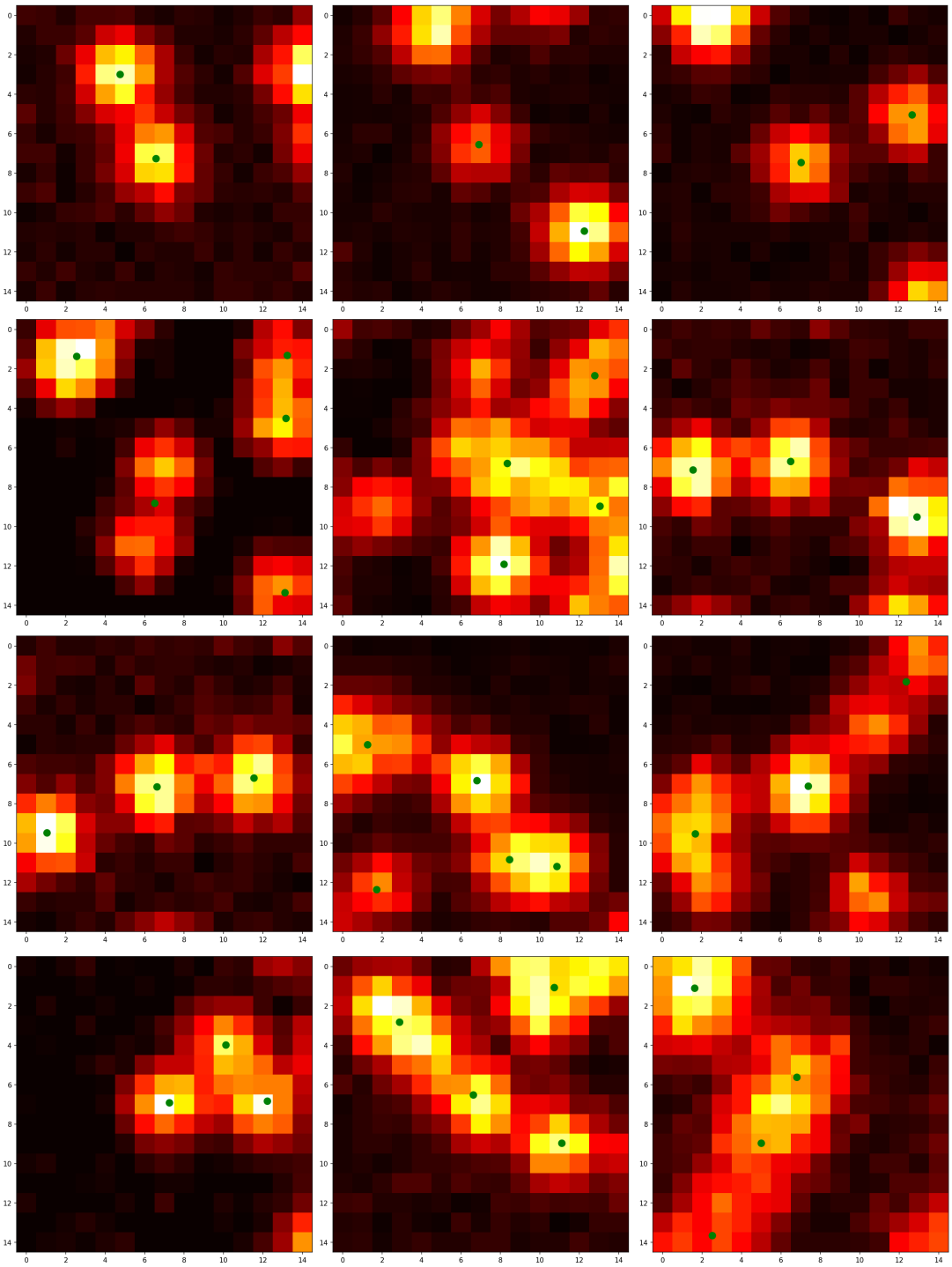

Figure A.24. Examples of detected and fitted ROIs for different active emitter densities with the respective obtained localizations marked with green dots. ROI-size is 15×15 $pixels$.

A.1. Selection Procedure of LM-parameter λ

Here, there is looked at the effect of λ on the localization precision for both SMLM and SIMFLUX, while holding the emitter and background intensity constant ($\theta_I = 1000\ photons$, $\theta_{bg} = 5\ photons/pixel$).

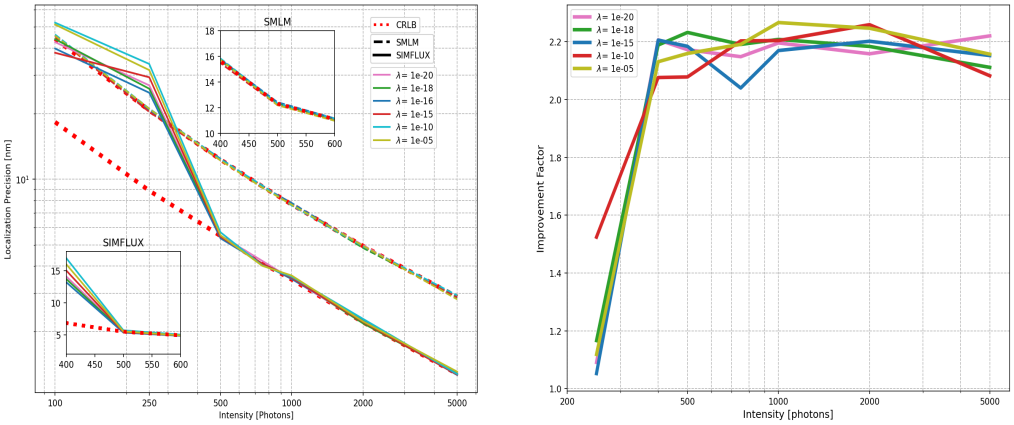

(a) **(b)**

Figure A.25. **(a)** Impact of the LM parameter λ on the localization precision for SMLM and SIMFLUX. **(b)** Improvement factor of SIMFLUX over SMLM in terms of localization precision. Improvement factor of SIMFLUX over SMLM in independent of the LM parameter λ.

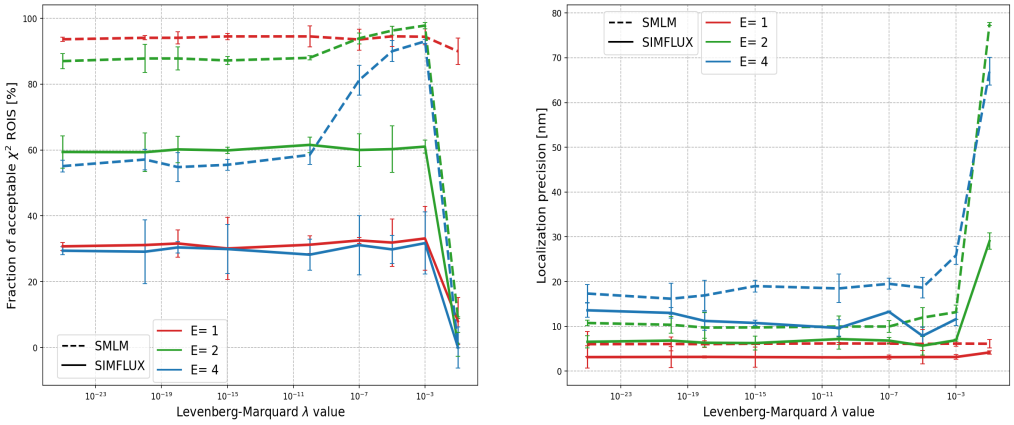

(a) **(b)**

Figure A.26. Impact of the LM parameter λ on the $\mathcal{X}^2$- test **(a)** and localization precision **(b)** for SMLM and SIMFLUX for single and multiple emitters while holding the emitter and background intensity constant at $\theta_I = 1000\ photons$ and $\theta_{bg} = 5\ photons/pixels$, respectively.

By looking at the effect of λ on the localization precision, improvement factor of SIMLFUX over SMLM and $\mathcal{X}^2$- test, no clear winner could be obtained. Since the value range $\lambda \sim [1 * 10^{-18} - 1 * 10^{-15}]$ do lead to slightly better results at low intensities $\leq 500\ photons$, we kept it in this range.

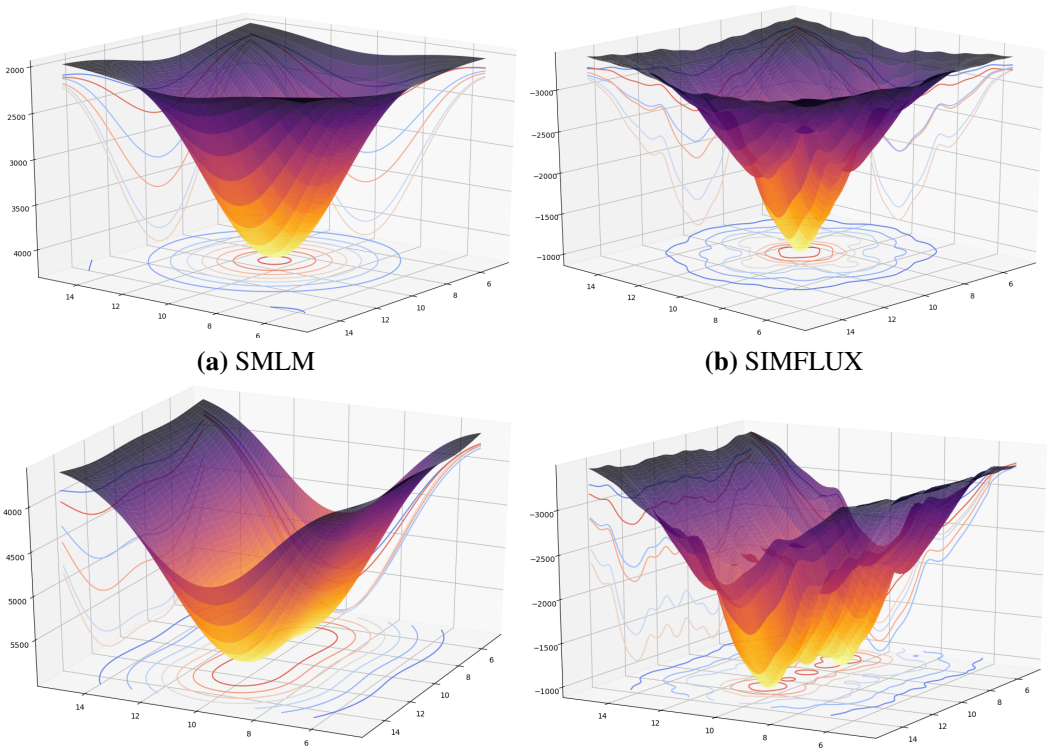

(a) SMLM **(b)** SIMFLUX

(c) SMLM **(d)** SIMFLUX

Figure A.27. **(a-b)** $3D$ Visualisation of the maximum likelihood estimation optimization landscape $E = 1$ and **(c-d)** $E = 2$. The true emitter and background intensities are considered to be known, the positions estimates are moved around the true position values. The optimization landscape of SIMFLUX contains multiple local minima and it gets worse for higher emitter numbers, while for SMLM has a smooth convex surface.

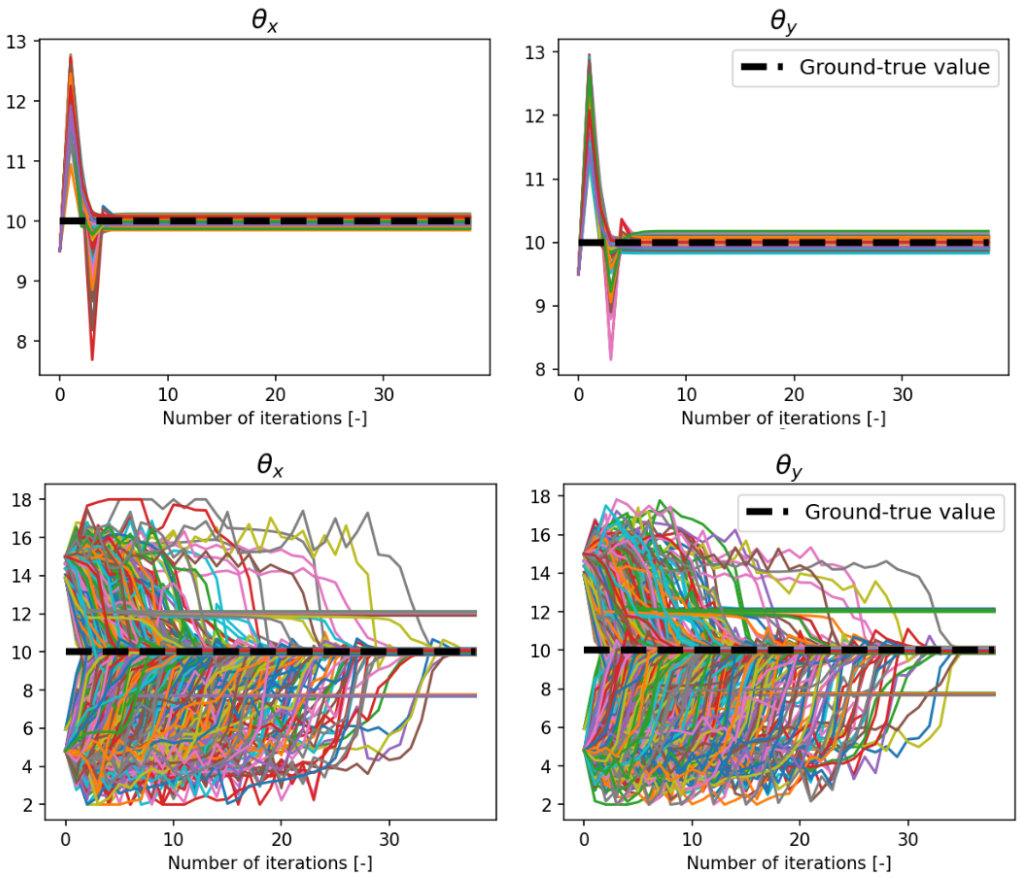

Figure A.28. The first and second row show the estimator convergence results for SMLM and SIMFLUX, respectively. Note: only estimator results which satisfy a final localization error ≤ 2 are displayed. The SMLM estimator shows "nice" smooth convergence, while the highly non-convex optimization landscape of SIMFLUX can strongly be seen in the estimator behaviour. SIMFLUX has multiple local minima, causing the estimator to get stuck in there (two local minima can be seen here in each direction). For the correctly converged results, SIMFLUX does show the expected localization precision factor of two.

B. Supplementary Notes

In this section, the image formation model will be derived for SMLM applications.

B.1. Image Formation Model - SMLM

We consider each flourophore as a point emitter with a specific $2D$ location (θ_x, θ_y) and intensity θ_I. Such an emitter can be described by a Dirac delta function as follows: $\theta_I \delta(x-\theta_x, y-\theta_y)$. To obtain the object image we consider the following convolution between the captured fluorescence signal $f(x,y)$ and the point spread function of the optical system $PSF(x,y)$:

$$f(x,y) \circledast PSF(x,y) = g(x,y)$$

with

$$f(x,y) = P(x,y)\big(\theta_I \delta(x_i - \theta_x, y_j - \theta_y) + \theta_{bg}\big)$$

where $\circledast$ is the $2D$ convolution operator, (x_i, y_j) the pixel coordinates $\forall\ i,j \in [1,K]$, θ_{bg} background intensity in $photons/pixel$ and $P(x)$ is the position-dependent unitless illumination power factor, such that $0 \leq P(x,y) \leq 1$.

For simplicity (x_i, y_j) will be denoted as just (x,y) from now on. By defining $u = x - \theta_x$ and $v = y - \theta_y$ and under the assumption that the area under $PSF(x,y)$ sums up to 1, the obtained camera image can then be described as:

$$\begin{aligned} g(x,y) &= PSF(x,y) \circledast f(x,y) = PSF(x,y) \circledast P_p(x,y)\big(\theta_I \delta(u,v) + \theta_{bg}\big) \\ &= \iint_{-\infty}^{\infty} PSF(\tau,\gamma) P_p(x-\tau, y-\gamma)\big(\theta_I \delta(u-\tau, v-\gamma) + \theta_{bg}\big) d\tau d\gamma \\ &= \theta_I \iint_{-\infty}^{\infty} PSF(\tau,\gamma) P_p(x-\tau, y-\gamma)\delta(u-\tau, v-\gamma) d\tau d\gamma + \theta_{bg} \iint_{-\infty}^{\infty} PSF(\tau,\gamma) P_p(x-\tau, y-\gamma) d\tau d\gamma \end{aligned}$$

$$g(x) = \theta_I PSF(u,y) P_p(\theta_x, \theta_y, \phi_p) + \theta_{bg} \iint_{-\infty}^{\infty} PSF(\tau,\gamma) P_p(x-\tau, y-\gamma) d\tau d\gamma$$

By looking at each pixel, we integrate over the finite area A_k of the kth pixel centered at (x_i, y_j), with p being the index for the illumination pattern position:

$$\mu_{k,p} = \iint_{x,y \in A_k} g(x,y) dx dy$$

$$\mu_{k,p} = \theta_I P_p(\theta_x, \theta_y, \phi_p) \iint_{x,y \in A_k} PSF(u,v) dx dy + \theta_{bg} \underbrace{\iint_{x,y \in A_k} \left(\iint_{-\infty}^{\infty} PSF(\tau,\gamma) P_p(x-\tau, y-\gamma) d\tau d\gamma \right) dx dy}_{B_{k,p}}$$

It can be noticed that the term $B_{k,p}$ does not depend on the emitter position (θ_x, θ_y), it only depends on the considerd PSF-model, the active illumination pattern p and the pixel area A_k.

$$\mu_{k,p} = \theta_I P_p(\theta_x, \theta_y, \phi_p) \iint_{x,y \in A_k} PSF(u,v) dx dy + \theta_{bg} B_{k,p}$$

As already mentioned, in literature[16;27;28] typically a two-dimensional Gaussian shape is taken as a description for the PSF model. The width of the placed Gaussian shape blob σ, in the 2D case is given by $\sigma = \sqrt{\sigma_x^2 + \sigma_y^2}$, the PSF model centered at the position of the emitter is then defined as:

$$PSF(u,v) = h(u,v)^2 = \frac{1}{2\pi\sigma^2} e^{\frac{-(u^2+v^2)}{2\sigma^2}} \tag{22}$$

$$\mu_{k,p} = \frac{\theta_I}{2\pi\sigma^2} P_p(\theta_x, \theta_y, \phi_p) \iint_{x,y \in A_k} e^{\frac{-(u^2+v^2)}{2\sigma^2}} dxdy + \theta_{bg} B_{k,p}$$

$$\mu_{k,p} = \frac{\theta_I}{2\pi\sigma^2} P_p(\theta_x, \theta_y, \phi_p) \int_{y_k - \frac{\Delta y}{2}}^{y_k + \frac{\Delta y}{2}} \int_{x_k - \frac{\Delta x}{2}}^{x_k + \frac{\Delta x}{2}} e^{\frac{-(u^2+v^2)}{2\sigma^2}} dxdy + \theta_{bg} B_{k,p}$$

Where Δx and Δy are the pixel sizes in the x and y direction, respectively. The integral is evaluated over the finite area A_k of the kth pixel centered at (x_i, y_j):

$$\mu_{k,p} = \theta_I P_p(\theta_x, \theta_y, \phi_p) \underbrace{\frac{1}{2}\left(erf(\frac{u + \frac{\Delta x}{2}}{\sqrt{2}\sigma}) - erf(\frac{u - \frac{\Delta x}{2}}{\sqrt{2}\sigma})\right)}_{E_{x_k}(u)} \underbrace{\frac{1}{2}\left(erf(\frac{v + \frac{\Delta y}{2}}{\sqrt{2}\sigma}) - erf(\frac{v - \frac{\Delta y}{2}}{\sqrt{2}\sigma})\right)}_{E_{y_k}(v)} + \theta_{bg} B_{k,p} \tag{23}$$

Where the $erf(x)$ function is defined as

$$erf(x) = \frac{2}{\sqrt{\pi}} \int_0^x e^{-t^2} dt$$

The expected photon count at the k_{th} pixel can then be written in the following compact notation as:

$$\mu_{k,p}(u,v) = \theta_I P_p(\theta_x, \theta_y, \phi_p) E_{x_k}(u) E_{y_k}(v) + \theta_{bg} B_{k,p}$$

The expected photon count from all existing emitters E, can hence be written in the following compact notation as:

$$\mu_{k,p}(u,v) = P_p(\theta_x, \theta_y, \phi_p) \sum_{e=1}^{E} \theta_{I_e} E_{x_{k,e}}(u) E_{y_{k,e}}(v) + \theta_{bg} B_{k,p} \tag{24}$$

Without making use of the position-dependent unitless illumination power factor $P(x)$, the expected photon count in the kth pixel from each emitter is given by:

$$\mu_k(u,v) = \sum_{e=1}^{E} \theta_{I_e} E_{x_{k,e}}(u) E_{y_{k,e}}(v) + \theta_{bg} \tag{25}$$

B.2. Theoretical localization precision

In case of single emitter, where the parameter vector $\theta = [\theta_x, \theta_y, \theta_I, \theta_{bg}]$ the Fisher information matrix is defined as:

$$\mathcal{I}(\theta) = \sum_{k=1}^{K}\sum_{p=1}^{\mathcal{P}} \frac{1}{\mu_{k,p}} \begin{bmatrix} \frac{\partial^2 \mu_{k,p}}{\partial \theta_x^2} & \frac{\partial \mu_{k,p}}{\partial \theta_x}\frac{\partial \mu_{k,p}}{\partial \theta_y} & \frac{\partial \mu_{k,p}}{\partial \theta_x}\frac{\partial \mu_{k,p}}{\partial \theta_I} & \frac{\partial \mu_{k,p}}{\partial \theta_x}\frac{\partial \mu_{k,p}}{\partial \theta_{I_{bg}}} \\ \frac{\partial \mu_{k,p}}{\partial \theta_y}\frac{\partial \mu_{k,p}}{\partial \theta_x} & \frac{\partial^2 \mu_{k,p}}{\partial \theta_y^2} & \frac{\partial \mu_{k,p}}{\partial \theta_y}\frac{\partial \mu_{k,p}}{\partial \theta_I} & \frac{\partial \mu_{k,p}}{\partial \theta_y}\frac{\partial \mu_{k,p}}{\partial \theta_{I_{bg}}} \\ \frac{\partial \mu_{k,p}}{\partial \theta_I}\frac{\partial \mu_{k,p}}{\partial \theta_x} & \frac{\partial \mu_{k,p}}{\partial \theta_I}\frac{\partial \mu_{k,p}}{\partial \theta_y} & \frac{\partial^2 \mu_{k,p}}{\partial \theta_I^2} & \frac{\partial \mu_{k,p}}{\partial \theta_I}\frac{\partial \mu_{k,p}}{\partial \theta_{I_{bg}}} \\ \frac{\partial \mu_{k,p}}{\partial \theta_{I_{bg}}}\frac{\partial \mu_{k,p}}{\partial \theta_x} & \frac{\partial \mu_{k,p}}{\partial \theta_{I_{bg}}}\frac{\partial \mu_{k,p}}{\partial \theta_y} & \frac{\partial \mu_{k,p}}{\partial \theta_{I_{bg}}}\frac{\partial \mu_{k,p}}{\partial \theta_I} & \frac{\partial^2 \mu_{k,p}}{\partial \theta_{bg}^2} \end{bmatrix} \qquad \in \mathbb{R}^{4\times 4}$$

where the log-likelihood derivatives are given by:

$$\begin{aligned}
\frac{\partial \mu_{k,p}}{\partial \theta_{x_e}} &= -\theta_{I_e}\pi\eta_p q_{p,x} m_p \sin(\phi_p(r^\circ))\frac{1}{2}\Big(erf(\frac{u+\frac{\Delta x}{2}}{\sqrt{2}\sigma}) - erf(\frac{u-\frac{\Delta x}{2}}{\sqrt{2}\sigma})\Big)\Big(erf(\frac{v+\frac{\Delta_y}{2}}{\sqrt{2}\sigma}) - erf(\frac{v-\frac{\Delta y}{2}}{\sqrt{2}\sigma})\Big) \\
&\quad + \theta_{I_e}\frac{1}{\mathcal{P}}(1+m_p\cos\phi)\frac{1}{\sqrt{2\pi}\sigma}\big(e^{\frac{-(u+\frac{\Delta x}{2})^2}{2\sigma^2}} - e^{\frac{-(u-\frac{\Delta x}{2})^2}{2\sigma^2}}\big)\Big(erf(\frac{v+\frac{\Delta_y}{2}}{\sqrt{2}\sigma}) - erf(\frac{v-\frac{\Delta y}{2}}{\sqrt{2}\sigma})\Big) \\
\frac{\partial \mu_{k,p}}{\partial \theta_{y_e}} &= -\theta_{I_e}\pi\eta_p q_{p,y} m_p \sin(\phi_p(r^\circ))\frac{1}{2}\Big(erf(\frac{u+\frac{\Delta x}{2}}{\sqrt{2}\sigma}) - erf(\frac{u-\frac{\Delta x}{2}}{\sqrt{2}\sigma})\Big)\Big(erf(\frac{v+\frac{\Delta_y}{2}}{\sqrt{2}\sigma}) - erf(\frac{v-\frac{\Delta y}{2}}{\sqrt{2}\sigma})\Big) \\
&\quad + \theta_{I_e}\frac{1}{\mathcal{P}}(1+m_p\cos\phi)\frac{1}{2}\Big(erf(\frac{u+\frac{\Delta x}{2}}{\sqrt{2}\sigma}) - erf(\frac{u-\frac{\Delta x}{2}}{\sqrt{2}\sigma})\Big)\frac{1}{\sqrt{2\pi}\sigma}\big(e^{\frac{-(v+\frac{\Delta y}{2})^2}{2\sigma^2}} - e^{\frac{-(v-\frac{\Delta y}{2})^2}{2\sigma^2}}\big) \\
\frac{\partial \mu_{k,p}}{\partial \theta_{I_e}} &= \frac{1}{\mathcal{P}}(1+m_p\cos\phi)\frac{1}{4}\Big(erf(\frac{u+\frac{\Delta x}{2}}{\sqrt{2}\sigma}) - erf(\frac{u-\frac{\Delta x}{2}}{\sqrt{2}\sigma})\Big)\Big(erf(\frac{v+\frac{\Delta_y}{2}}{\sqrt{2}\sigma}) - erf(\frac{v-\frac{\Delta y}{2}}{\sqrt{2}\sigma})\Big) \\
\frac{\partial \mu_{k,p}}{\partial \theta_{bg}} &= \eta_p
\end{aligned}$$

Whereby the estimation precision of each parameter is given by the diagonal terms as follows:

$$\sigma_{\hat{\theta}} = \begin{bmatrix} \sigma_{\theta_x} \\ \sigma_{\theta_y} \\ \sigma_{\theta_I} \\ \sigma_{\theta_{bg}} \end{bmatrix} = \begin{bmatrix} \sqrt{Var_{\theta_x}(\hat{\theta})} \\ \sqrt{Var_{\theta_y}(\hat{\theta})} \\ \sqrt{Var_{\theta_I}(\hat{\theta})} \\ \sqrt{Var_{\theta_{bg}}(\hat{\theta})} \end{bmatrix} = \begin{bmatrix} \sqrt{(\mathcal{I}(\theta)^{-1})_{1,1}} \\ \sqrt{(\mathcal{I}(\theta)^{-1})_{2,2}} \\ \sqrt{(\mathcal{I}(\theta)^{-1})_{3,3}} \\ \sqrt{(\mathcal{I}(\theta)^{-1})_{4,4}} \end{bmatrix}$$

For the multi-emitter case, the following set of parameters per ROI is estimated:

$$\theta = [\theta_{bg}, \theta_{x_1}, \theta_{y_1}, \theta_{I_1}, \theta_{x_2}, \theta_{y_2}, \theta_{I_2}, \ldots, \theta_{x_E}, \theta_{y_E}, \theta_{I_E}]^{\mathsf{T}}, \qquad \in \mathbb{R}^T$$

$$\mathcal{I}(\theta) = \sum_{k=1}^{K}\sum_{p=1}^{\mathcal{P}} \frac{1}{\mu_{k,p}} \begin{bmatrix} \frac{\partial^2 \mu_{k,p}}{\partial \theta_{bg}} & \frac{\partial \mu_{k,p}}{\partial \theta_{bg}}\frac{\partial \mu_{k,p}}{\partial \theta_{x_1}} & \cdots & \cdots & & & \cdots & \frac{\partial \mu_{k,p}}{\partial \theta_{bg}}\frac{\partial \mu_{k,p}}{\partial \theta_{I_E}} \\ \frac{\partial \mu_{k,p}}{\partial \theta_{x_1}}\frac{\partial \mu_{k,p}}{\partial \theta_{bg}} & \frac{\partial^2 \mu_{k,p}}{\partial \theta_{x_1}} & \ddots & & & & & \vdots \\ \vdots & \vdots & \frac{\partial^2 \mu_{k,p}}{\partial \theta_{y_1}} & \ddots & & & & \vdots \\ \vdots & & \ddots & \frac{\partial^2 \mu_{k,p}}{\partial \theta_{I_1}} & & & & \vdots \\ \vdots & & & \ddots & \ddots & & & \vdots \\ \vdots & & & & \cdots & \frac{\partial \mu_{k,p}}{\partial^2 \theta_{x_E}} & \cdots & \vdots \\ \vdots & & & & & \cdots & \frac{\partial \mu_{k,p}}{\partial^2 \theta_{y_E}} & \frac{\partial \mu_{k,p}}{\partial \theta_{y_E}}\frac{\partial \mu_{k,p}}{\partial \theta_{I_E}} \\ \frac{\partial \mu_{k,p}}{\partial \theta_{I_E}}\frac{\partial \mu_{k,p}}{\partial \theta_{bg}} & \cdots & & & \cdots & \cdots & \frac{\partial \mu_{k,p}}{\partial \theta_{I_E}}\frac{\partial \mu_{k,p}}{\partial \theta_{y_E}} & \frac{\partial^2 \mu_{k,p}}{\partial \theta_{I_E}} \end{bmatrix} \in \mathbb{R}^{T\times T} \tag{26}$$

Whereby $T = 3E + 1$, for E being the number of emitters

B.3. Localization Improvement

It is well known that the covariance matrix of any unbiased estimator $\hat{\theta}$ is lower bounded by the CRLB matrix[18]. The Fisher information matrix over all pixels K and illumination patterns $\mathcal{P}$ and zero background $\theta_{bg} = 0$:

$$\mathcal{I}_{i,j}(\theta) = \sum_{k=1}^{K}\sum_{p=1}^{\mathcal{P}} \frac{1}{\mu_{k,p}} \frac{\partial \mu_{k,p}}{\partial \theta_i}\frac{\partial \mu_{k,p}}{\partial \theta_j}, \qquad where \;\; \mu_{k,p} = \sum_{e=1}^{E} \theta_{I_e} P_p(\phi_p(r_0)) E_{k,e}(\tilde{r})$$

The fisher information in the x-direction of the ith emitter for $i \in [1, \ldots, E]$:

$$\begin{aligned} \mathcal{I}_{x_i,x_i}(\theta) &= \sum_{k=1}^{K}\sum_{p=1}^{\mathcal{P}} \frac{1}{\mu_{k,p}} \Big(\frac{\partial \mu_{k,p}}{\partial \theta_{x_i}}\Big)^2 \\ &= \sum_{k=1}^{K}\sum_{p=1}^{\mathcal{P}} \mu_{k,p} \Big(\frac{\partial \ln \mu_{k,p}}{\partial \theta_{x_i}}\Big)^2 \\ &= \sum_{k=1}^{K}\sum_{p=1}^{\mathcal{P}}\sum_{e=1}^{E} \theta_{I_e} P_p(\phi_p(r^\circ)) E_{k,e}(\tilde{r}) \Big(\frac{\partial \ln \mu_{k,p}}{\partial \theta_{x_i}}\Big)^2 \end{aligned}$$

$$
\begin{aligned}
\frac{\partial \ln \mu_{k,p}}{\partial \theta_{x_i}} &= \frac{1}{E_{k,e}(\tilde{r})}\frac{\partial E_{k,e}(\tilde{r})}{\partial \theta_{x_i}} + \frac{1}{P_p(\phi_p(r^\circ))}\frac{\partial P_p(\phi_p(r^\circ))}{\partial \theta_{x_i}} \\
&= \frac{e^{\frac{-(x-\theta_x+\frac{\Delta x}{2})^2}{2\sigma^2}} - e^{\frac{-(x-\theta_x-\frac{\Delta x}{2})^2}{2\sigma^2}}}{\int_{-\frac{\Delta x}{2}}^{\frac{\Delta x}{2}} e^{\frac{-(x-\theta_x)^2}{2\sigma^2}} dx} + \frac{1}{P_p(\phi_p(r^\circ))}\frac{\partial P_p(\phi_p(r^\circ))}{\partial \theta_{x_i}} \\
&= \frac{x-\theta_x}{\sigma} + \frac{2\pi\eta_p q_{p,x} m_p \sin(\phi_p(r^\circ))}{\frac{1}{\mathcal{P}}(1+m_p\cos(\phi_p))} \\
\frac{\partial \ln \mu_{k,p}}{\partial \theta_{x_i}} &= \frac{x-\theta_x}{\sigma} + \frac{2\pi q_{p,x} m_p \sin(\phi_p))}{1+m_p\cos(\phi_p)} \\
\frac{\partial \ln \mu_{k,p}}{\partial \theta_{y_i}} &= \frac{y-\theta_y}{\sigma} + \frac{2\pi q_{p,y} m_p \sin(\phi_p))}{1+m_p\cos(\phi_p)}
\end{aligned}
$$

For $E = 1$

$$
\begin{aligned}
\mathcal{I}_{x_1,x_1}(\theta) &= \sum_{k=1}^{K}\sum_{p=1}^{\mathcal{P}} \theta_{I_1} P_p(\phi_p(r^\circ)) E_{k,1}(\tilde{r}) \Big(\frac{\partial \ln \mu_{k,p}}{\partial \theta_{x_1}}\Big)^2 \\
&= \sum_{k=1}^{K}\sum_{p=1}^{\mathcal{P}} \theta_{I_1} P_p(\phi_p(r^\circ)) E_{k,1}(\tilde{r}) \Big(\frac{x-\theta_x}{\sigma} + \frac{2\pi q_{p,x} m_p \sin(\phi_p(r^\circ))}{1+m_p\cos(\phi)}\Big)^2
\end{aligned}
$$

Since $\sum_{k=1}^{K}\sum_{p=1}^{\mathcal{P}} \theta_{I_1} P_p(\phi_p(r^\circ)) E_{k,1}(\tilde{r}) \approx \sum_{k=1}^{K} \theta_{I_1} E_{k,1}(\tilde{r}) \approx \theta_{I_1}$, approximating the pixel summation with the integration results in:

$$
\begin{aligned}
\mathcal{I}_{x_1,x_1}(\theta) &\approx \frac{\theta_{I_1}}{\sigma^2} + \theta_{I_1}\sum_{p=1}^{\mathcal{P}} 4\eta_p(\pi q_{p,x} m_p)^2 \frac{\sin^2(\phi_p)}{1+m_p\cos(\phi_p)} \\
&= \frac{\theta_{I_1}}{\sigma^2} + 4\pi^2\theta_{I_1}\sum_{p=1}^{\mathcal{P}} q_{p,x}^2 \underbrace{\eta_p m_p^2 \frac{\sin^2(\phi_p)}{1+m_p\cos(\phi_p)}}_{Q_p}
\end{aligned}
$$

For $E > 1$

$$
\begin{aligned}
\mathcal{I}_{x_i,x_i}(\theta) &= \sum_{k=1}^{K}\sum_{p=1}^{\mathcal{P}}\sum_{e=1}^{E} \theta_{I_e} P_p(\phi_p(r^\circ)) E_{k,e}(\tilde{r}) \Big(\frac{\partial \ln \mu_{k,p}}{\partial \theta_{x_i}}\Big)^2 \\
&\approx \sum_{e=1}^{E} \frac{\theta_{I_e}}{\sigma^2} + 4\pi^2\theta_{I_e}\sum_{p=1}^{\mathcal{P}} q_{p,x}^2 Q_p
\end{aligned}
$$

Let the total number of photons be equal to $\sum_{e=1}^{E} \theta_{I_e} = N$

$$\triangleright\ \mathcal{I}_{x_e,x_e}(\theta) \approx \frac{N}{\sigma^2} + 4\pi^2 N \sum_{p=1}^{\mathcal{P}} q_{p,x}^2 Q_p$$

$$\triangleright\ \mathcal{I}_{x_e,y_e}(\theta) \approx 4\pi^2 N \sum_{p=1}^{\mathcal{P}} q_{p,x} q_{p,y} Q_p$$

$$\triangleright\ \mathcal{I}_{y_e,y_e}(\theta) \approx \frac{N}{\sigma^2} + 4\pi^2 N \sum_{p=1}^{\mathcal{P}} q_{p,y}^2 Q_p$$

For the two considered orthogonal orientations (x, y), and for perfect modulation $m = 1$ the following expression simplifies to:

$$\sum_{p=1}^{\mathcal{P}} q_{p,x}^2 Q_p = \sum_{p=1}^{\mathcal{P}} \frac{1}{\mathsf{p}^2} \cos(\beta_p)^2 \eta_p^2 \frac{\sin^2(\phi_p)}{(1+\cos(\phi_p))^2} = \sum_{p=1}^{\mathcal{P}} \frac{1}{\mathsf{p}^2} \cos(\beta_p)^2 \eta_p^2 \frac{\sin^2(\phi_p)}{2} = \frac{1}{2\mathsf{p}^2}$$

The improvement factor obtained by SIMFLUX:

$$\begin{aligned}
\mathcal{I}_{x_e,x_e}(\theta) = \mathcal{I}_{y_e,y_e}(\theta) &= \frac{N}{\sigma^2} + \frac{2\pi^2 N}{\mathsf{p}^2} = \frac{N\mathsf{p}^2 + 2\pi^2 N\sigma^2}{\sigma^2 \mathsf{p}^2} \\
\sigma_{x_e,x_e}(\theta) = \sigma_{y_e,y_e}(\theta) &= \sqrt{\frac{1}{\frac{N\mathsf{p}^2+2\pi^2 N\sigma^2}{\sigma^2\mathsf{p}^2}}} = \frac{\sigma\mathsf{p}}{\sqrt{N\mathsf{p}^2 + 2\pi^2 N\sigma^2}} \\
&= \frac{\sigma\mathsf{p}}{\sqrt{\mathsf{p}^2 N(1 + \frac{2\pi^2 N\sigma^2}{\mathsf{p}^2})}} \\
&= \frac{\sigma}{\sqrt{N}} \frac{1}{\sqrt{1 + \frac{2\pi^2\sigma^2}{\mathsf{p}^2}}}
\end{aligned}$$

$$\text{Improvement factor: } I_f = \frac{\sigma_{SMLM}}{\sigma_{SIMFLUX}} = \frac{\frac{\sigma}{\sqrt{N}}}{\frac{\sigma}{\sqrt{N}} \frac{1}{\sqrt{1+\frac{2\pi^2\sigma^2}{\mathsf{p}^2}}}} = \sqrt{1 + \frac{2\pi^2\sigma^2}{\mathsf{p}^2}} \tag{27}$$

Which shows that for SIMFLUX over SMLM the improvement factor $I_f \geq 1\ \forall\ p, \sigma$
However, as earlier mentioned, assuming $m = 1$ is unrealistic. For $m < 1$, the localization precision will become worse and dependent on the global phase. This results in the localization precision being non-uniform and anisotropic to some extend.

$$\sigma_x = \frac{\sigma}{\sqrt{N}\sqrt{1 + 2\pi^2 \frac{\sigma^2}{\mathsf{p}^2} Q\left(\frac{2\pi x}{\mathsf{p}} - \chi_1\right)}}$$

$$\sigma_y = \frac{\sigma}{\sqrt{N}\sqrt{1 + 2\pi^2 \frac{\sigma^2}{\mathsf{p}^2} Q\left(\frac{2\pi y}{\mathsf{p}} - \chi_2\right)}}$$

B.4. Levenberg-Marquardt Algorithm

The Levenberg-Marquardt (LM) algorithm has the advantage of being relative insensitive to initial parameters and rapid convergence. In the LM approach the Hessian (second-derivative terms) is ignored and only the first derivatives are considered. The second order terms are ignored due to their potential destabilizing effects, e.g. jumping around the minima, and due to the frequent difficulty in computing them. In the neighborhood of the current set of parameters θ_{curr}, the optimization function $\mathcal{F}(\theta)$ may be approximated by its Taylor expansion as follows:

$$\mathcal{F}\left(\theta_{curr}+\Delta\theta\right) \approx \mathcal{F}(\theta_{curr}) + \nabla_\theta \mathcal{F}(\theta)\cdot\Delta\theta + \frac{1}{2}\Delta\theta^{\mathrm{T}}\cdot\underbrace{\nabla_\theta\nabla_\theta\mathcal{F}(\theta)}_{H(\theta)}\cdot\Delta\theta + \mathcal{O}^3 \tag{28}$$

where $\nabla_\theta\mathcal{F}(\theta)$ and $\nabla_\theta\nabla_\theta\mathcal{F}(\theta)$ are defined as:

$$\nabla_\theta\mathcal{F}(\theta) = \frac{\partial\mathcal{F}}{\partial\theta_i} = 2\sum_{k=1}^{K}\frac{\partial\mu_k}{\partial\theta_i} - 2\sum_{k=1}^{K} n_k\frac{1}{\mu_k}\frac{\partial\mu_k}{\partial\theta_i} = 2\sum_{k=1}^{K}\left(1-\frac{n_k}{\mu_k}\right)\frac{\partial\mu_k}{\partial\theta_i}$$

$$\nabla_\theta\nabla_\theta\mathcal{F}(\theta) = H(\theta) = \frac{\partial^2\mathcal{F}}{\partial\theta_i\partial\theta_j} = 2\sum_{k=1}^{K}\frac{\partial\mu_k}{\partial\theta_i}\frac{\partial\mu_k}{\partial\theta_j}\frac{n_k}{\mu_k^2} + \left(1-\frac{n_k}{\mu_k}\right)\frac{\partial^2\mu_k}{\partial\theta_i\partial\theta_j}$$

As already mentioned we ignore the second-derivative terms and thus from now on we continue with:

$$\nabla_\theta\mathcal{F}(\theta) = \sum_{k=1}^{K}\left(1-\frac{n_k}{\mu_k}\right)\frac{\partial\mu_k}{\partial\theta_i} + \mathcal{O}^2$$

$$\nabla_\theta\nabla_\theta\mathcal{F}(\theta) = \sum_{k=1}^{K}\frac{\partial\mu_k}{\partial\theta_i}\frac{\partial\mu_k}{\partial\theta_j}\frac{n_k}{\mu_k^2} + \mathcal{O}^2$$

Considering the expected photon count on the k_{th} pixel:

$$\mu_{k,p} = \sum_{e=1}^{E}\theta_{I_e}P_p(\phi_p(r^\circ))E_{k,e}(\tilde{r}) + \eta_p\theta_{bg},$$

In the numerical, Levenberg-Marquard based, implementation of the maximum likelihood estimation problem, the following set of parameters per ROI is estimated:

$$\theta = [\theta_{bg}, \theta_{x_1}, \theta_{y_1}, \theta_{I_1}, \theta_{x_2}, \theta_{y_2}, \theta_{I_2}, \ldots, \theta_{x_E}, \theta_{y_E}, \theta_{I_E}]^{\mathsf{T}}, \qquad \in \mathbb{R}^T$$

whereby in 2D the dimension of the parameter vector is equal to $T = 3E + 1$ and with partial derivatives (for the completely written out terms see B.2) :

$$\frac{\partial\mu_k}{\partial\theta} = \left[\frac{\partial\mu_k}{\partial\theta_{bg}}, \frac{\partial\mu_k}{\partial\theta_{x_1}}, \frac{\partial\mu_k}{\partial\theta_{y_1}}, \frac{\partial\mu_k}{\partial\theta_{I_1}}, \frac{\partial\mu_k}{\partial\theta_{x_2}}, \frac{\partial\mu_k}{\partial\theta_{y_2}}, \frac{\partial\mu_k}{\partial\theta_{I_2}}, \ldots, \frac{\partial\mu_k}{\partial\theta_{x_E}}, \frac{\partial\mu_k}{\partial\theta_{y_E}}, \frac{\partial\mu_k}{\partial\theta_{I_E}}\right]^{\mathsf{T}}$$

The following matrix $\alpha \in \mathbb{R}^{T\times T}$ and vector $\beta \in \mathbb{R}^{T}$ are defined:

$$\alpha_{i,j} = \sum_{k=1}^{K} \frac{\partial \mu_k}{\partial \theta_i}\frac{\partial \mu_k}{\partial \theta_j}\frac{n_k}{\mu_k^2}, \qquad \beta_i = -\sum_{k=1}^{K}\left(1-\frac{n_k}{\mu_k}\right)\frac{\partial \mu_k}{\partial \theta_i} \tag{29}$$

$$\alpha = \sum_{k=1}^{K}\frac{n_k}{\mu_k^2}\begin{bmatrix} \frac{\partial \mu_k}{\partial \theta_{bg}}\frac{\partial \mu_k}{\partial \theta_{bg}} & \frac{\partial \mu_k}{\partial \theta_{bg}}\frac{\partial \mu_k}{\partial \theta_{x_1}} & \cdots & \cdots & \cdots & \frac{\partial \mu_k}{\partial \theta_{bg}}\frac{\partial \mu_k}{\partial \theta_{x_E}} \\ \frac{\partial \mu_k}{\partial \theta_{x_1}}\frac{\partial \mu_k}{\partial \theta_{bg}} & \frac{\partial \mu_k}{\partial \theta_{x_1}}\frac{\partial \mu_k}{\partial \theta_{x_1}} & \ddots & & & \vdots \\ \vdots & \vdots & \frac{\partial \mu_k}{\partial \theta_{y_1}}\frac{\partial \mu_k}{\partial \theta_{y_1}} & \ddots & & \vdots \\ \vdots & & \ddots & \frac{\partial \mu_k}{\partial \theta_{I_1}}\frac{\partial \mu_k}{\partial \theta_{I_1}} & & \vdots \\ \vdots & & & \ddots & \ddots & \vdots \\ \vdots & & & & \cdots & \frac{\partial \mu_k}{\partial \theta_{y_E}}\frac{\partial \mu_k}{\partial \theta_{y_E}} \quad \frac{\partial \mu_k}{\partial \theta_{y_E}}\frac{\partial \mu_k}{\partial \theta_{I_E}} \\ \frac{\partial \mu_k}{\partial \theta_{I_E}}\frac{\partial \mu_k}{\partial \theta_{bg}} & \cdots & \cdots & \cdots & \cdots & \frac{\partial \mu_k}{\partial \theta_{I_E}}\frac{\partial \mu_k}{\partial \theta_{y_E}} \quad \frac{\partial \mu_k}{\partial \theta_{I_E}}\frac{\partial \mu_k}{\partial \theta_{I_E}} \end{bmatrix} \tag{30}$$

$$\beta = -\sum_{k=1}^{K}\left(1-\frac{n_k}{\mu_k}\right)\begin{bmatrix} \frac{\partial \mu_k}{\partial \theta_{bg}} & \frac{\partial \mu_k}{\partial \theta_{x_1}} & \frac{\partial \mu_k}{\partial \theta_{y_1}} & \frac{\partial \mu_k}{\partial \theta_{I_1}} & \cdots & \frac{\partial \mu_k}{\partial \theta_{y_E}} & \frac{\partial \mu_k}{\partial \theta_{I_E}} \end{bmatrix} \tag{31}$$

B.4.1. Iteration Step

If the current parameter set θ_{curr} is sufficiently near a local or the global minimum, by differentiating eq. 28 and equalizing it to zero, the optimal parameter set θ^*_{min}, which minimizes the objective function, hence maximizes the likelihood function can be obtained.

$$\begin{aligned} \nabla_\theta \mathcal{F}\left(\theta_{curr}+\Delta\theta\right) &= 0 \\ \nabla_\theta \mathcal{F}(\theta_{curr}) + \nabla_\theta\nabla_\theta \mathcal{F}(\theta)\cdot\Delta\theta &= 0 \\ \underbrace{\nabla_\theta\nabla_\theta \mathcal{F}(\theta)}_{\alpha}\cdot\Delta\theta &= \underbrace{-\nabla_\theta \mathcal{F}(\theta_{curr})}_{\beta} \end{aligned}$$

We then have the iteration step:

$$\theta_{t+1} = \theta_t + \alpha^{-1}\beta$$

In same cases the Taylor expansion can give a poor approximation, which leads to increasing in $\mathcal{F}(\theta)$, or the inversion of the Hessian matrix may become numerically ill-conditioned if the Hessian matrix is almost singular. For this reason the diagonal elements of the matrix α are augmented by an adaptive parameter λ

$$\hat{\alpha} = \alpha(I + I\lambda)$$

whereby the identity matrix $I \in \mathbb{R}^{T\times T}$. For relative low values of λ it approaches the Gaus-Newton algorithm, however for high values of λ, the algorithm will take a step mainly in the direction of the negative gradient, i.e. it approaches the steepest descent algorithm. The iteration step can thus be defined as:

$$\theta_{t+1} = \theta_t + \hat{\alpha}^{-1}\beta \tag{32}$$

Chapter 5

Conclusion

"The more I study science, the more I believe in GOD."
- Albert Einstein

This chapter serves as a brief summary and a concise discussion of the main findings and insights gained during the whole process. An effort has been made to make this work as self-contained and smooth to read as possible. Although this work might not necessarily be complete, hopefully the relevant topics are adequately covered, and an indication is provided for the reader of the precious role that fluorescence- and single-molecule localization microscopy plays in modern biology and the expected bright future of super-resolution localization microscopy.

5-1 Summary

For a long time, scientists were convinced of the impossibility of achieving a microscopic resolution beyond the diffraction limit of light, known as the Abbe-diffraction limit. This limitation prevents objects with a separation distance smaller than $\sim 200\ nm$ in the lateral direction and $\sim 500\ nm$ in the axial direction to be visualized and distinguished from each other. This resolution is not enough to differentiate between proteins, since proteins are typically in the range of a billionth of a meter (nm) in size. Over the last decades, a couple of so-called "super-resolution" fluorescence microscopy techniques have been developed, which are able to surpass the diffraction barrier. They offer high resolution imaging of various cellular structures and dynamics with a resolution far beyond the diffraction limit. The observation of, previously limited and unclear, cellular structures has demonstrated the great promise of super-resolution fluorescence microscopy in exemplifying biological processes at the cellular level. The pivotal and essential role that microscopes play these days in the study of the ongoing pandemic due to the emergence of the new Corona (SARS-CoV-2) virus in December 2019, in a market in Wuhan, China. This virus is currently being witnessed by more than 150 countries, has infected more than 60 million people around the world, and has resulted in the death of more than 1.4 million people.

Single-molecule localization microscopy (SMLM), with its variations, is currently one of the broadly used super-resolution imaging techniques. Inherently, SMLM is based on acquiring a sequence of diffraction-limited images, consisting of sparsely distributed emitting fluorophores. The total image processing procedure can be described as follows: data acquisition and pre-processing of the raw camera images; regions of interest (ROIs) detection and fluorophores localization; data post-processing and finally the visualization of the super-resolution image.

One of the most crucial questions in SMLM applications concerns the precision with which the location of a single molecule can be determined. The Cramér–Rao lower bound (CRLB), defined as the theoretical precision limit, is used to quantify the estimation performance in terms of localization precision. Recently, a couple of modulation enhanced single-molecule localization microscopy methods have shown resolution improvement by combining patterned illumination with SMLM techniques, such as MINFLUX [18] and SIMFLUX [9]. The challenging part is that the analysis of images by these methods requires sparse activation regions to prevent overlap between active emitters. During spot identification, the conventional and the extended (with illumination patterns) SMLM algorithms quickly lose both their precision and accuracy, when too many emitters are concurrently active in the imaging frame. From the various simulations performed, we noticed that this occurred for active emitter densities $\geq 0.5\ emitters/\mu m^2$. Several multi-emitter fitting techniques have been developed aiming for exploiting all available fluorescence data, consequently leading to resolution improvement at high molecular densities and the ability of resolving overlapping emitters, while minimizing the computational effort, e.g. 3B [11], SPIDER [29], BAMF [19] and MFA [28].

Here, we proposed a modulation enhanced SMLM maximum likelihood-based method, which is an extension of the current SIMFLUX [9] approach, able to localize multiple emitters simultaneously within a single ROI. The mathematical framework of the algorithm is comprehensively built up throughout this work; the expected theoretical improvement is elucidated and validated with realistic simulations. We presented the theoretical and numerical performance evaluation results of the Multi-SIMFLUX algorithm against standard 2D-Gaussian SMLM on simulated data. The localization performance of multi-SIMFLUX for various active emitter densities is compared against single-SIMFLUX, single-SMLM and multi-SMLM ($E = 5$). These simulations explore the effect of different realistic imaging conditions on the quantitative and qualitative achieved by the algorithm. The main findings are presented and discussed in Chapter 4.

To summarize, we can say that the developed Multi-SIMFLUX method enhances super-resolution reconstructions by improving the detection rate, while averagely maintaining the localization precision compared to conventional single molecule localization techniques. It is able to double the localization precision in comparison with conventional $2D$ Gaussian multi-emitter SMLM algorithms at low active emitter densities and maintains a slight localization precision improvement at higher densities. Our approach has shown to perform well in theory and on simulations. We foresee a bright future for its implementation on real experimental data. Higher density imaging permits shorter acquisition times; however, it results in more computational complexity in analysis and a huge dependence on hard- and software tools.

To the best of our knowledge, the MULTI-SIMFLUX approach is a pioneer in combining structured illumination patterns and multi-emitter fitting.

5-2 Future Outlook

Using the knowledge acquired in this study, a potential direction for future work is proposed.

- Multi-emitter localization has, due to its parallelizable characteristic, great potential for improving the imaging speed of super-resolution localization microscopy. Our obtained results are based on numerical simulations, since the use of simulated data has the advantage of the imaging conditions being known and more in control. However, we foresee that after developing and optimizing this approach, it will be useful for very highly densed active regions and for high-speed live imaging. Moreover, experimental measurements like for live cell imaging can contain a non-negligible amount of background noise, therefore it is also of great paramount to have accurate noise models and high-efficiency hard- and software tools to apply this approach on real experimental data. Also, the emitters' blinking and bleaching behaviour has to be taken into consideration by for instance Hidden Markov models.
- The ongoing revolution of deep learning applications has demonstrated its capability in the handling of enormous amounts of data within a decent amount of time, and impressive results in diverse image processing and computer-vision applications have been achieved. Hence, making it quite applicable for the implementation of decreasing acquisition and/or processing time and the extraction of more information from the input imaging frames. By combining multi-emitter SIMFLUX with deep learning to allow high-throughput data analysis, one can anticipate further improvements in quality and applicability of meLM for future life-science research. Of course, it would be interesting to investigate how to combine localization algorithms with deep learning to further improve the imaging speed and/or imaging throughput of SMLM, without compromising other requirements from high-throughput localization microscopy.
  To make efficient use of the available (simulated and/or experimental) data, the focus must be on capturing as many rich features as possible. This can be achieved by auto-encoder and U-net neural structures. The aim of the auto-encoder is to learn and represent (encode) the input data according to its most meaningful features that accurately describe and abstract away all of the details of that input. They are typically applied for the purpose of dimensionality reduction and data compression, hence improving computational efficiency. When only making use of an encode/decode architecture, the estimations tend to lack the sharpness and fine details. To help address this, cross or skip connections can be added between blocks of the network, resulting in a U-net like structure. The skip connections cross from same sized part in downsampling path to the upsampling path. These feature maps from the encoder layers are concatenated with the corresponding layers of the decoder. This will allow the network to combine local- and larger context information and maintaining fast propagation of data through the network.
  Furthermore, taking temporal dynamics (with Recurrent Neural Networks (RNNs) for instance) into consideration also minimizes the chance of missing useful information in the sequence of images, regarding localization in high density.
- Our study has shown that a simple Gaussian PSF model is sufficiently accurate for low-density data, whereas the quality of high-density imaging depends strongly on the model of the PSF. We believe that the PSF model will have an even more significant role in 3D multi-emitter SMLM applications.

Appendix A

Appendices

This appendix contains mathmatical notations and derivations which were referred to in the main work.

A-1 Fisher Information and Cramér Rao Lower Bound

We consider an independent random variable x, whose probability distribution function admits a Probability density function (PDF) $p(x|\theta)$. As already mentioned, if an event has a small probability of occurring, then the occurrence of that specific event does bring much information. The aim is to maximize the amount of information, which can be extracted from x about the estimation of the parameter θ. This can be achieved by maximizing the log-likelihood function of the obtained data $|l'(x|\theta)|$ (or preferably $[l'(x|\theta)]^2$). We define the following for the log-likelihood function:

$$l(x|\theta) = log\ p(x|\theta), \qquad l'(x|\theta) = \frac{\partial}{\partial\theta} log\ p(x|\theta) = \frac{p'(x|\theta)}{p(x|\theta)}$$

Thus the expected value of $[l'(x|\theta)]^2$, can be taken as a measure of the amount of information provided by the data about the parameter θ. The information in the random variable x regarding the estimation of the parameter θ is defined as the Fisher information matrix $\mathcal{I}(\theta)$ [48;41]:

$$\mathcal{I}(\theta) = \mathbb{E}_\theta[[l'(x|\theta)]^2] = \int [l'(x|\theta)]^2 p(x|\theta) dx \tag{A-1}$$

The expected value of the gradient of the log-likelihood function

$$\begin{aligned}\mathbb{E}_\theta[l'(x|\theta)] &= \int l'(x|\theta)p(x|\theta)dx \\ &= \int \frac{p'(x|\theta)}{p(x|\theta)} p(x|\theta)dx \\ &= \int p'(x|\theta)dx\end{aligned}$$

By assuming that integration and derivation may be exchanged, then

$$= \frac{\partial}{\partial\theta}\int p(x|\theta)dx = 0$$

Another notation is the following:

$$l''(x|\theta) = \frac{p''(x|\theta)}{p(x|\theta)} - [l'(x|\theta)]^2$$
$$E_\theta[l''(x|\theta)] = \int \left[\frac{p''(x|\theta)}{p(x|\theta)} - [l'(x|\theta)]^2\right] p(x|\theta)dx$$
$$E_\theta[l''(x|\theta)] = \underbrace{\int p''(x|\theta)dx}_{=0} - \mathbb{E}_\theta[[l'(x|\theta)]^2] = -\mathcal{I}(\theta)$$

So, we obtain another formulation for the Fisher information matrix:

$$\mathcal{I}(\theta) = -\mathbb{E}_\theta[l''(x|\theta)] \tag{A-2}$$

Fisher Information from a Poisson Distribution

Since counting photons is inherently an discrete operation, that can only produce positive integer outcomes, the Poisson distribution function is considered. By the consideration that the intensity (number of photons) n in each pixel follows a Poisson distribution, the probability of observing n photons in the k_{th} pixel is:

$$P(n_k|\mu_k(\theta)) = \frac{\mu_k^{n_k}}{n_k!}e^{-\mu_k} \tag{A-3}$$

where n_k is the observed intensity in the k_{th} pixel. Another fundamental characteristic of the Poisson distribution is that both the expected value and the variance of n_k are equal to μ_k, such that:

$$\mathbb{E}[n_k] = \mathbb{E}[(n_k - \mu_k)^2] = Var_\theta(n_k) = \mu_k$$

The likelihood function, for an image with K pixels, for parameter θ is defined as:

$$\mathcal{L}(n|\mu(\theta)) = \prod_{k=1}^{K} P(n_k|\mu_k(\theta)) \tag{A-4}$$

where $n = \{n_1, n_2, \ldots, n_K\}$ and $\mu = \{\mu_1, \mu_2, \ldots, \mu_K\}$ are the observed and expected intensities, respectively. The log-likelihood is:

$$l(x|\theta) = \sum_{k=1}^{K} \Big(x_k \ln(\mu_k) - \ln(x_k!) - \mu_k\Big)$$

The first and second partial derivatives of the log-likelihood:

$$l'(x|\theta) = \frac{\partial\ l(x|\theta)}{\partial\theta_i} = \sum_{k=1}^{K} \frac{x_k}{\mu_k}\frac{\partial\mu_k}{\partial\theta_i} - \frac{\partial\mu_k}{\partial\theta_i}$$
$$l''(x|\theta) = \frac{\partial^2\ l(x|\theta)}{\partial\theta_i\theta_j} = \sum_{k=1}^{K} \Big(\frac{-x_k}{\mu_k^2}\frac{\partial\mu_k}{\partial\theta_i}\frac{\partial\mu_k}{\partial\theta_j} + \frac{x_k}{\mu_k}\frac{\partial^2\mu_k}{\partial\theta_i\partial\theta_j} - \frac{\partial^2\mu_k}{\partial\theta_i\partial\theta_j}\Big)$$

The Fisher Information matrix can then be computed by calculating the following expectation:

$$\mathcal{I}_{i,j}(\theta) = -\mathbb{E}_\theta[l''(x|\theta)] = \sum_{k=1}^{K} \Big(\underbrace{\mathbb{E}[x_k]}_{=\mu_k}\frac{1}{\mu_k^2}\frac{\partial\mu_k}{\partial\theta_i}\frac{\partial\mu_k}{\partial\theta_j} - \underbrace{\mathbb{E}[x_k]}_{=\mu_k}\frac{1}{\mu_k}\frac{\partial^2\mu_k}{\partial\theta_i\partial\theta_j} + \frac{\partial^2\mu_k}{\partial\theta_i\partial\theta_j}\Big)$$

Hence, the Fisher Information matrix for Poisson distributed measurements is denoted a follows:

$$\mathcal{I}_{i,j}(\theta) = \sum_{k=1}^{K} \frac{1}{\mu_k} \frac{\partial \mu_k}{\partial \theta_i} \frac{\partial \mu_k}{\partial \theta_j} \tag{A-5}$$

while the Fisher Information matrix for Poisson distributed measurements with a sequence of $p = 1, 2, \ldots, \mathcal{P}$ illuminations, is denoted a follows

$$\mathcal{I}_{i,j}(\theta) = \sum_{k=1}^{K} \sum_{p=1}^{\mathcal{P}} \frac{1}{\mu_{k,p}} \frac{\partial \mu_{k,p}}{\partial \theta_i} \frac{\partial \mu_{k,p}}{\partial \theta_j} \tag{A-6}$$

By looking at the covariance around the expected estimate:

$$Var_\theta[l'(x|\theta)] = \mathbb{E}_\theta\big[[l'(x|\theta) - 0][l'(x|\theta) - 0]\big] = \mathbb{E}_\theta\big[[l'(x|\theta)]^2\big]$$

Therefore the definition of the Fisher information matrix can be written as:

$$\mathcal{I}(\theta) = Var_\theta[l'(x|\theta)] \tag{A-7}$$

Theoretically, the best-possible solution for an unbiased parameter estimation problem is derived by using the Cramer-Rau lower bound (CRLB), which is basically the limiting lower bound of the variance for any unbiased parameter estimator. Being able to place such a lower bound on the variance has proven to be extremely useful in practice. It provides a benchmark against, which the performance achieved from any unbiased estimator can be compared. Besides, it shows us the physical impossibility of finding an unbiased estimator, whose variance is less than this bound. The general expression for the Cramer-Rao Lower bound (CRLB) is given by the inverse of the Fisher information matrix $\mathcal{I}(\theta)$, which is defined as:

$$\mathcal{I}(\theta) = \int \Big[\frac{\partial \log p(x|\theta)}{\partial \theta}\Big]^2 p(x|\theta) dx \tag{A-8}$$

Where $p(x|\theta)$ is the probability density function (PDF) of the continuous parameter θ. Suppose that $\hat{\theta}(x)$ is an unbiased estimator of θ, where x is an independent random variable whose cumulative distribution function admits a density $p(x|\theta)$. Since $\hat{\theta}(x)$ is an unbiased estimator of θ, the expected value is defined as the following:

$$E\big[\hat{\theta}(x) - \theta\big] = 0$$
$$\int (\hat{\theta}(x) - \theta) p(x|\theta) dx = 0$$

This expression must hold for any value of θ, so the partial derivative with respect to θ must also equal zero.
Differentiating with respect to θ gives:

$$\begin{aligned}\frac{\partial}{\partial \theta} \int (\hat{\theta}(x) - \theta) p(x|\theta) dx &= \int (\hat{\theta}(x) - \theta) \frac{\partial}{\partial \theta} p(x|\theta) dx + \int \frac{\partial}{\partial \theta} (\hat{\theta}(x) - \theta) p(x|\theta) dx = 0 \\ &= \int (\hat{\theta}(x) - \theta) \frac{\partial}{\partial \theta} p(x|\theta) dx - \underbrace{\int p(x|\theta) dx}_{=1} = 0 \\ \int (\hat{\theta}(x) - \theta) \frac{\partial}{\partial \theta} p(x|\theta) dx &= 1\end{aligned}$$

Since we know that $\frac{\partial p(x|\theta)}{\partial \theta} = p(x|\theta) \frac{\partial log p(x|\theta)}{\partial \theta}$, we get

$$\int (\hat{\theta}(x) - \theta) p(x|\theta) \frac{\partial log p(x|\theta)}{\partial \theta} dx = 1$$
$$\int \underbrace{\Big((\hat{\theta}(x) - \theta)\sqrt{p(x|\theta)}\Big)}_{\mathbf{g}} \underbrace{\Big(\sqrt{p(x|\theta)} \frac{\partial log p(x|\theta)}{\partial \theta}\Big)}_{\mathbf{f}} dx = 1$$

Recall the Cauchy-Schwartz inequality:

$$\int \mathbf{gf} \leq \Big(\int \mathbf{f}^2 \int \mathbf{g}^2 \Big)^{\frac{1}{2}}$$

Implementing it yields to:

$$1 \leq \int \Big(\sqrt{p(x|\theta)} \frac{\partial log p(x|\theta)}{\partial \theta} \Big)^2 dx \int \Big((\hat{\theta}(x) - \theta) \sqrt{p(x|\theta)} \Big)^2 dx$$
$$1 \leq \underbrace{\int \Big(\frac{\partial log p(x|\theta)}{\partial \theta} \Big)^2 p(x|\theta) dx}_{\mathcal{I}(\theta)} \underbrace{\int \Big(\hat{\theta}(x) - \theta \Big)^2 p(x|\theta) dx}_{Var(\hat{\theta})}$$

Rearranging the inequality gives us the final result:

$$Var(\hat{\theta}) \geq \mathcal{I}(\theta)^{-1} \tag{A-9}$$

In case of single emitter, where the parameter vector $\theta = [\theta_x, \theta_y, \theta_I, \theta_{bg}]$ the Fisher information matrix is defined as:

$$\mathcal{I}(\theta) = \sum_{k=1}^{K} \sum_{p=1}^{\mathcal{P}} \frac{1}{\mu_{k,p}} \begin{bmatrix} \frac{\partial^2 \mu_{k,p}}{\partial \theta_x^2} & \frac{\partial \mu_{k,p}}{\partial \theta_x} \frac{\partial \mu_{k,p}}{\partial \theta_y} & \frac{\partial \mu_{k,p}}{\partial \theta_x} \frac{\partial \mu_{k,p}}{\partial \theta_I} & \frac{\partial \mu_{k,p}}{\partial \theta_x} \frac{\partial \mu_{k,p}}{\partial \theta_{I_{bg}}} \\ \frac{\partial \mu_{k,p}}{\partial \theta_y} \frac{\partial \mu_{k,p}}{\partial \theta_x} & \frac{\partial^2 \mu_{k,p}}{\partial \theta_y^2} & \frac{\partial \mu_{k,p}}{\partial \theta_y} \frac{\partial \mu_{k,p}}{\partial \theta_I} & \frac{\partial \mu_{k,p}}{\partial \theta_y} \frac{\partial \mu_{k,p}}{\partial \theta_{I_{bg}}} \\ \frac{\partial \mu_{k,p}}{\partial \theta_I} \frac{\partial \mu_{k,p}}{\partial \theta_x} & \frac{\partial \mu_{k,p}}{\partial \theta_I} \frac{\partial \mu_{k,p}}{\partial \theta_y} & \frac{\partial^2 \mu_{k,p}}{\partial \theta_I^2} & \frac{\partial \mu_{k,p}}{\partial \theta_I} \frac{\partial \mu_{k,p}}{\partial \theta_{I_{bg}}} \\ \frac{\partial \mu_{k,p}}{\partial \theta_{I_{bg}}} \frac{\partial \mu_{k,p}}{\partial \theta_x} & \frac{\partial \mu_{k,p}}{\partial \theta_{I_{bg}}} \frac{\partial \mu_{k,p}}{\partial \theta_y} & \frac{\partial \mu_{k,p}}{\partial \theta_{I_{bg}}} \frac{\partial \mu_{k,p}}{\partial \theta_I} & \frac{\partial^2 \mu_{k,p}}{\partial \theta_{bg}^2} \end{bmatrix} \qquad \in \mathbb{R}^{4 \times 4}$$

Whereby the estimation precision of each parameter is given by the diagonal terms as follows:

$$\sigma_{\hat{\theta}} = \begin{bmatrix} \sigma_{\theta_x} \\ \sigma_{\theta_y} \\ \sigma_{\theta_I} \\ \sigma_{\theta_{bg}} \end{bmatrix} = \begin{bmatrix} \sqrt{Var_{\theta_x}(\hat{\theta})} \\ \sqrt{Var_{\theta_y}(\hat{\theta})} \\ \sqrt{Var_{\theta_I}(\hat{\theta})} \\ \sqrt{Var_{\theta_{bg}}(\hat{\theta})} \end{bmatrix} = \begin{bmatrix} \sqrt{(\mathcal{I}(\theta)^{-1})_{1,1}} \\ \sqrt{(\mathcal{I}(\theta)^{-1})_{2,2}} \\ \sqrt{(\mathcal{I}(\theta)^{-1})_{3,3}} \\ \sqrt{(\mathcal{I}(\theta)^{-1})_{4,4}} \end{bmatrix}$$

For the multi-emitter case, the following set of parameters per ROI is estimated:

$$\theta = [\theta_{bg}, \theta_{x_1}, \theta_{y_1}, \theta_{I_1}, \theta_{x_2}, \theta_{y_2}, \theta_{I_2}, \ldots, \theta_{x_E}, \theta_{y_E}, \theta_{I_E}], \qquad \in \mathbb{R}^T$$

$$\mathcal{I}(\theta) = \sum_{k=1}^{K} \sum_{p=1}^{\mathcal{P}} \frac{1}{\mu_{k,p}} \begin{bmatrix} \frac{\partial^2 \mu_{k,p}}{\partial \theta_{bg}} & \frac{\partial \mu_{k,p}}{\partial \theta_{bg}} \frac{\partial \mu_{k,p}}{\partial \theta_{x_1}} & \cdots & \cdots & & & \cdots & \frac{\partial \mu_{k,p}}{\partial \theta_{bg}} \frac{\partial \mu_{k,p}}{\partial \theta_{I_E}} \\ \frac{\partial \mu_{k,p}}{\partial \theta_{x_1}} \frac{\partial \mu_{k,p}}{\partial \theta_{bg}} & \frac{\partial^2 \mu_{k,p}}{\partial \theta_{x_1}} & \ddots & & & & & \vdots \\ \vdots & \vdots & \frac{\partial^2 \mu_{k,p}}{\partial \theta_{y_1}} & \ddots & & & & \vdots \\ \vdots & & \ddots & \frac{\partial^2 \mu_{k,p}}{\partial \theta_{I_1}} & & & & \vdots \\ \vdots & & & \ddots & \ddots & & & \vdots \\ \vdots & & & & \cdots & \frac{\partial \mu_{k,p}}{\partial^2 \theta_{x_E}} & \cdots & \vdots \\ \vdots & & & & & \cdots & \frac{\partial \mu_{k,p}}{\partial^2 \theta_{y_E}} & \frac{\partial \mu_{k,p}}{\partial \theta_{y_E}} \frac{\partial \mu_{k,p}}{\partial \theta_{I_E}} \\ \frac{\partial \mu_{k,p}}{\partial \theta_{I_E}} \frac{\partial \mu_{k,p}}{\partial \theta_{bg}} & \cdots & & & \cdots & \cdots & \frac{\partial \mu_{k,p}}{\partial \theta_{I_E}} \frac{\partial \mu_{k,p}}{\partial \theta_{y_E}} & \frac{\partial^2 \mu_{k,p}}{\partial \theta_{I_E}} \end{bmatrix} \qquad \in \mathbb{R}^{T \times T}$$

Whereby $T = 3E + 1$, for E being the number of emitters. However, for the multi-emitter case the Fisher information matrix is singular due the occurrence of $x_i, y_i = x_j, y_j$, and near this singular point,

can not be used to correctly calculate estimator precision. For this reason we used the pseudo-inverse of the Fisher matrix to determine the CRLB:

$$Var(\hat{\theta}) \geq \mathcal{I}^{\dagger}(\theta)$$

whereby † denoted the psuedo-inverse, which is defines as:

$$\mathcal{I}^{\dagger}(\theta) = (\mathcal{I}^{\top}\mathcal{I})^{-1}\mathcal{I}^{\top}$$

hence the precision becomes:

$$\sigma_{\hat{\theta}} \geq \sqrt{(\mathcal{I}^{\top}\mathcal{I})^{-1}\mathcal{I}^{\top}}$$

A-2 Likelihood Ratio Test

The likelihood ratio test (LRT) is typically used to compare, the goodness of fit of two competing statistical models. The comparison is performed based upon the ratio of their (log-) likelihoods. For both models, maximum likelihood estimation is performed, whereby they maximize over different parameter spaces. A null hypothesis H_0, is usually set such that the parameter θ is in a specified set θ^0 and the alternative hypothesis H_1, is set such that the parameter θ is in a specified set θ^1. Both sets can span the entire parameter space Θ or a subset. The log likelihood ratio for H_0 is given by:

$$LLR = -2[\ln\ \mathcal{L}(\hat{\theta^0}) - \ln\ \mathcal{L}(\hat{\theta}^1)] = -2\ \ln\Big[\frac{\mathcal{L}(\hat{\theta^0})}{\mathcal{L}(\hat{\theta}^1)}\Big] \tag{A-10}$$

Whereby $\hat{\theta}^0$ and $\hat{\theta}^1$ are the maxima of the parameter spaces, θ^0 and θ^1 respectively. LRTs have typically been used to compare nested models, i.e. that complex models can be described by by simpler models by imposing some constraints on the parameters. By the Neyman-Peason lemma, the LRT has the highest power compared to the two other classical hypothesis testing approaches; the Lagrange multiplier- and the Wald test.

Generalized Likelihood Ratio Test - GLRT

The LRT has had a great contribution in the success to parametric inferences. In general LRT may not exist in nonparametric function estimation or if it exists it is hard to find. Thus, this approach does not applicable for non parametric inferences based on function estimation.The generalized likelihood test GLRT is able to overcome these drawbacks. Suppose the data has a PDF $p(x|\theta^0; H_0)$ under H_0 and $p(x|\theta^1; H_1)$ under H_1, the dimensions of θ^0 and θ^1 are not necessarily the same. The GRLT replaces the true parameters with their maximum likelihood estimates. Generally, the GLRT decides H_1 if

$$GLRT(x) = \frac{p(x|\hat{\theta}^1; H_1)}{p(x|\hat{\theta}^0; H_0)}\ >\ \gamma$$

Where $\hat{\theta}^1$ is the MLE (the value which maximizes $p(x|\theta^1; H_1)$) of θ^1 assuming H_1 is true and $\hat{\theta}^0$ is the MLE of θ^0 assuming H_0 is true. By determining the MLEs, also information about the unknown parameters is obtained. Another, sometimes more convenient form of the GLRT since $\hat{\theta}_i$ is the MLE under H_i:

$$GLRT(x) = \frac{\max_{\theta^1}\ p(x|\theta^1; H_1)}{\max_{\theta^0}\ p(x|\theta^0; H_0)} \tag{A-11}$$

A-3 Multiple Hypothesis Testing

Consider the case where we wish to distinguish between M $\{H_0, H_1, \ldots, H_{M-1}\}$ hypotheses. Such a problem arises in case of deciding how many emitters there are within a ROI. The hypothesis H_0, suggests that there are no emitters in a given ROI, H_1 suggests that there is 1 emitter, and so on. The optimize the decision, commonly the minimum probability error P_e criterion or its generalization, the Bayes risk, is employed [37].

The cost (loss in performance) assigned to the decision to choose H_i when H_j is true is denoted by $C_{i,j}$. We aim to choose the hypothesis (number of emitters) that minimizes the cost, hence optimizes performance. The expected costs or Bayes risk is denoted as:

$$\mathcal{R} = \sum_{i=0}^{M-1} \sum_{j=0}^{M-1} C_{i,j} P\left(H_i|H_j\right) P\left(H_j\right)$$

Let R_i be the set of values in R^M which map into the decision H_i. So in essence let $R_i = \{x : \ decide\ H_i\}$, where $i = 0, 1, \ldots, M-1$ partition the decision space so that:

$$\begin{aligned}\mathcal{R} &= \sum_{i=0}^{M-1} \sum_{j=0}^{M-1} C_{i,j} \int_{R_i} P\left(x|H_j\right) P\left(H_j\right) dx = \sum_{i=0}^{M-1} \sum_{j=0}^{M-1} C_{i,j} \int_{R_i} P\left(H_j|x\right) P\left(x\right) dx \\ &= \sum_{i=0}^{M-1} \int_{R_i} \sum_{j=0}^{M-1} C_{i,j} P\left(H_j|x\right) P\left(x\right) dx\end{aligned}$$

Let the average cost of deciding H_i if x is observed be $C_i = \sum_{j=0}^{M-1} C_{i,j} P(H_j|x)$

$$\mathcal{R} = \sum_{i=0}^{M-1} \int_{R_i} C_i P\left(x\right) dx$$

Hence, the goal is to decide H_i for which C_i minimum.

$$\hat{H} = arg \min_i \sum_{j=0}^{M-1} C_{i,j} P(H_j|x) = arg \min_i C_i\left(x\right)$$

Considering the Bayes theorem:

$$P\left(H_j|x\right) = P\left(x|H_j\right) P\left(H_j\right) / P\left(x\right)$$

the minimization can be rewritten as:

$$\hat{H} = arg \min_i \sum_{j=0}^{M-1} C_{i,j} P(H_j|x) = arg \min_i \sum_{j=0}^{M-1} C_{i,j} \frac{P\left(x|H_j\right) P\left(H_j\right)}{P\left(x\right)}$$

Since $P(x)$ is common to all terms and it is reasonable to assign equal probabilities to prior probabilities of the respective hypotheses, i.e. $P(H_i) = \frac{1}{M}$ we get:

$$\hat{H} = arg \min_i \frac{1}{M} \sum_{j=0}^{M-1} C_{i,j} P(x|H_j)$$

We introduce the log-likelihood ratio with respect to H_0, which is considered as a normalization:

$$ln\ \left(LR_{i,0}\left(x\right)\right) = LLR_{i,0}(x) = \ ln\left(\frac{p\left(x|H_i\right)}{p\left(x|H_0\right)}\right) = \sum_k x_k ln\left(\frac{\mu_k^i}{\mu_k^0}\right) - \mu_k^i + \mu_k^0$$

where the decision boundaries between the hypotheses are

$$ln\ \left(\mathrm{LR}_{i,j}\left(x\right)\right) = \ln\left(1\right) = 0\ \ so,\ LLR_{0,0} = ln(1) = 0$$

Hence, this is equivalent to minimizing

$$\hat{H} = arg\min_{i} \frac{1}{M} \sum_{j=0}^{M-1} C_{i,j} LLR_{j,0}(x)$$

If the minimizing i is not unique, we choose the largest minimizing i. As already mentioned the Bayes risk is a generalisation of the P_e, and it reduces to P_e in the case of:

$$C_{ij} = \begin{cases} 0 & i = j \\ 1 & i \neq j \end{cases}$$

$$\hat{H} = arg\min_{i} \frac{1}{M} \sum_{j=0}^{M-1} LLR_{j,0}(x) - LLR_{i,0}(x)$$

$$\hat{H} = arg\max_{i} \sum_{j=1}^{M-1} LLR_{j,0}(x)$$

We define the probability of error P_e as:

$$P_e = \sum_{i=0}^{M-1} \sum_{\substack{j=0 \\ j\neq i}}^{M-1} P(H_i|H_j)P(H_j) = \sum_{i=0}^{M-1} \sum_{\substack{j=0 \\ j\neq i}}^{M-1} \int_{R_i} P(H_j|x)P(x)dx$$

The goal is to minimize P_e, i.e. determining the correct number of emitters. Further assuming, $P(X) = c$ and using the Bayes' Theorem P_e reduces to,

$$P_e = \sum_{i=0}^{M-1} \sum_{\substack{j=0 \\ j\neq i}}^{M-1} P(x|H_j)P(H_j) = \frac{1}{M} \sum_{i=0}^{M-1} \sum_{\substack{j=0 \\ j\neq i}}^{M-1} \int_{R_i} P(x|H_j)$$

$$\sum_{i=0}^{M-1} \int_{R_i} P\left(x|H_j\right) dx\ = 1, \quad for\ i,j = 0,..,M-1$$

Whereby:

$$\int_{R_i} P\left(x|H_j\right) dx\ \leq 1, \quad for\ i,j = 0,..,M-1$$

An example for clarification, shown in Figure A-1 ($M = 3$) we obtain:

$$\begin{aligned}
P_e &= \frac{1}{3}\sum_{i=0}^{2}\sum_{\substack{j=0\\ j\neq i}}^{2} P\left(x \mid H_j\right) \\
&= \frac{1}{3}\left(\int_{R_1} P\left(x \mid H_0\right) dx + \int_{R_2} P\left(x \mid H_0\right) dx + \int_{R_0} P\left(x \mid H_1\right) dx + \int_{R_2} P\left(x \mid H_1\right) dx \right. \\
&\left. + \int_{R_0} P\left(x \mid H_2\right) dx + \int_{R_1} P\left(x \mid H_2\right) dx\right) \\
&= \frac{1}{3}\left(3 - \int_{R_0} P\left(x \mid H_0\right) dx - \int_{R_1} P\left(x \mid H_1\right) dx - \int_{R_2} P\left(x \mid H_2\right) dx\right) \\
&= 1 - \frac{1}{3}\left(\int_{R_0} P\left(x \mid H_0\right) dx + \int_{R_1} P\left(x \mid H_1\right) dx + \int_{R_2} P\left(x \mid H_2\right) dx\right)
\end{aligned}$$

It's less of an effort to compute the probability of error from the probability of making the correct decision, $P_e = 1 - P_c$. The probability of making the correct decision is defined as:

$$P_c = \frac{1}{3}(\int_{R_0} P\left(x|H_0\right) dx + \int_{R_1} P\left(x|H_1\right) dx + \int_{R_2} P\left(x|H_2\right) dx)$$

$$P_c = \frac{1}{3}(P_r\{x < \gamma_1|H_0\} + P_r\{\gamma_1 < x < \gamma_2|H_1\} + P_r\{x > \gamma_2|H_1\})$$

To minimize the P_e we should decide:

$$\begin{aligned}
H_0: &\quad if\ x < \gamma_1 \\
H_1: &\quad if\ \gamma_1 < x < \gamma_2 \\
H_2: &\quad if\ x > \gamma_2
\end{aligned}$$

To do so we again consider the (log) likelihood ratio:

$$ln\ \left(LR_{i,j}\left(x\right)\right) = \ ln\left(\frac{p\left(x|H_i\right)}{p\left(x|H_j\right)}\right) = \sum_k x_k ln\left(\frac{\mu_k^i}{\mu_k^j}\right) - \mu_k^i + \mu_k^j$$

Hence:

$$P_c = \frac{1}{3}(P_r\{x < \gamma_1|H_0\} + P_r\{\gamma_1 < x < \gamma_2|H_1\} + P_r\{x > \gamma_2|H_1\})$$
$$= \frac{1}{3}\left(P\left(LR_{0,1} > 0|H_0\right) + \left(P\left(LR_{1,2} > 0|H_1\right) - P\left(LR_{0,1} > 0|H_0\right)\right) + P\left(LR_{1,2} < 0\right)|H_2)\right)$$

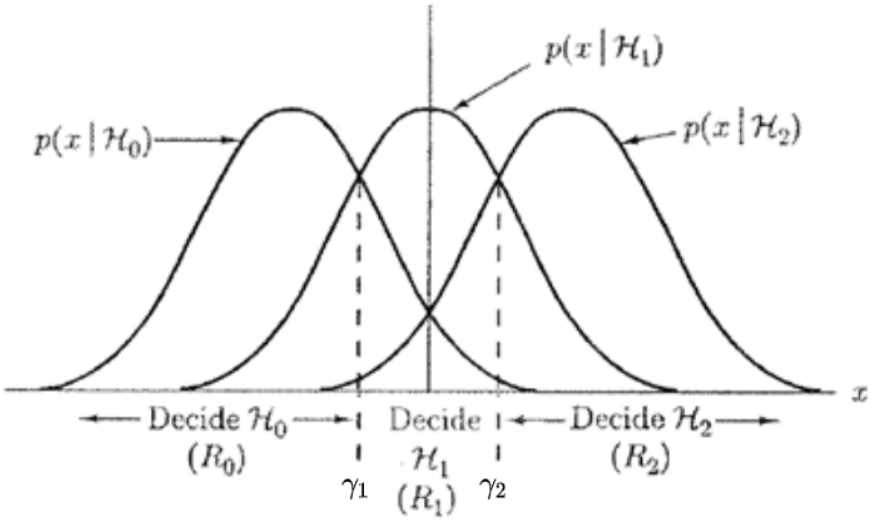

Figure A-1: Schematic illustration of a decision problem. Here we see three possible hypotheses H_i, with corresponding decision regions R_i that would result in a minimum probability of error [37].

As already mentioned, the log-likelihood ratio tends to be normally distributed, as the number of data points goes to infinty ($x \to \infty$), central limit theorem). The expected value μ and variance σ^2, are computed under the conditional H_i, i.e. the one assumed to be true:

$$\mu_{i,j,l} = \sum_{k}^{K} \mu_k^l \ln(\frac{\mu_k^i}{\mu_k^j}) - \mu_k^i + \mu_k^j$$

$$\sigma_{i,j,l}^2 = \sum_{k}^{K} \mu_k^l \ln(\frac{\mu_k^i}{\mu_k^j})$$

$$P_c = \frac{1}{3}(\phi(\frac{\mu_{0,1,0}}{\sigma_{0,1,0}}) + \phi(\frac{\mu_{1,2,1}}{\sigma_{1,2,1}}) - \phi(\frac{\mu_{0,1,0}}{\sigma_{0,1,0}}) + \phi(-\frac{\mu_{1,1,2}}{\sigma_{1,1,2}}))$$

$$P_c = \frac{1}{3}(\phi(\frac{\mu_{1,2,1}}{\sigma_{1,2,1}}) + \phi(-\frac{\mu_{1,1,2}}{\sigma_{1,1,2}}))$$

Bibliography

[1] *Nonlinear structured-illumination microscopy: wide-field fluorescence imaging with theoretically unlimited resolution.* Proc. Natl. Acad. Sci. USA, PubMed: 16141335, 2005.

[2] *The Nobel Prize in Chemistry 2014.* The Royal Swedish Academy of Sciences, Press release, 2014.

[3] *STORM Microscopy (Stochastic Optical Reconstruction Microscopy).* ThermoFisher scientific, 2018.

[4] *Coronavirus live realtime counter.* www.worldometers.info/coronavirus/, 2020.

[5] Patrina A.Pellet, Xiaoli Sun, Travis J.Gould, James E.Rothman, Ming-Qun Xu, Ivan R. Corrêa, Jr., and Joerg Bewersdorf. *Two-color STED microscopy in living cells.* Biomed Opt Express, 2011.

[6] Robert P.J. Nieuwenhuizen Bernd Reiger and Sjoerd Stallinga. *Image Processing and Analysis for Single-Molecule Localization Microscopy.* IEEE Signal Processing Magazine, V. 32, I. 1, 49 - 57, 2014.

[7] Bradbury, S., Evennett, and P. *Fluorescence Microscopy, Contrast Techniques in Light Microscopy.* BIOS Scientific Publishers, Ltd, 1996.

[8] Corey C.Ford and Jerome Eisenfeld. *Some unresolved questions pertaining to the mathematical analysis of fluorescence decay data.* Applied nonlinear analysis, 1979.

[9] Jelmer Cnossen, Taylor Hinsdale, Rasmus Ø. Thorsen, Florian Schueder, Ralf Jungmann, Carlas S. Smith, Bernd Rieger, and Sjoerd Stallinga. *Localization microscopy at doubled precision with patterned illumination.* BioRxiv, 2019.

[10] Justin Cooper, Alan Mullan, Aleksandra Marsh, and Marcin Barszczewski. *Characterization of performance of back-illuminated SCMOS cameras versus conventional SCMOS and EMCCD cameras for microscopy applications.* SPIE, 2019.

[11] Susan Cox, Edward Rosten, James Monypenny, Tijana Jovanovic-Talisman, Dylan T. Burnette, Jennifer Lippincott-Schwartz, Gareth E. Jones, and Rainer Heintzmann. *Bayesian localisation microscopy reveals nanoscale podosome dynamics.* Nature Methods, 9, 2, 195-200, 2012.

[12] Hendrik Deschout, Francesca Cella Zanacchi, Michael Mlodzianoski, Alberto Diaspro, Joerg Bewersdorf, Samuel T. Hess, and Kevin Braeckmans. *Precisely and accurately localizing single emitters in fluorescence microscopy.* Nature Methods 11, 253, 2014.

[13] Chao Dong, Chen Change Loy, Kaiming He, and Xiaoou Tang. *Learning a Deep Convolutional Network for Image Super-Resolution.* Department of Information Engineering, The Chinese University of Hong Kong, Microsoft Research, 2015.

[14] Gregor P.C. Drummen. *Fluorescent Probes and Fluorescence (Microscopy) Techniques — Illuminating Biological and Biomedical Research.* MDPI, 2012.

[15] Marcus Dyba and Stefan W.Hell. *Photostability of a fluorescent marker under pulsed excited-state depletion through stimulated emission.* Osa Publishing, 2003.

[16] Abbe E. *Beitrage zur Theorie des Mikroskops und der mikroskopischen Wahrnehmung.* Arch. Mikroskop Anat.;9:413–420, 1873.

[17] Betzig Eric et al. *Imaging intracellular fluorescent proteins at nanometer resolution.* PubMed, 2006.

[18] Balzarotti F., Eilers Y., Gwosch KC., Gynnå AH., Westphal V., Stefani FD., Elf J., and Hell SW. *Nanometer resolution imaging and tracking of fluorescent molecules with minimal photon fluxes.* Science.;355(6325):606-612 [PubMed], 2016.

[19] Mohamadreza Fazel, Michael J. Wester, Hanieh Mazloom-Farsibaf, Marjolein B. M. Meddens, Alexandra S. Eklund, Thomas Schlichthaerle, Florian Schueder, Ralf Jungmann, and Keith A. Lidke. *Bayesian Multiple Emitter Fitting using Reversible Jump Markov Chain Monte Carlo.* Scientific Reports 9, 13791 doi:10.1038/s41598-019-50232-x, 2019.

[20] Brain J Ford. *Antony van Leeuwenhoek- microscopist and visionary scientist.* Journal of Biological education, 1989.

[21] M. G. L. Gustafsson. *Surpassing the lateral resolution limit by a factor of two using structured illumination microscopy.* HORT COMMUNICATION," Journal of Microscopy, vol. 198, pp. 82–87, 2000.

[22] Mats G. L. Gustafsson, David A. Agard, and John Sedat. *I5M: 3D widefield light microscopy with better than 100 nm axial resolution.* Journal of Microscopy, Vol. 195, Pt 1, 1999.

[23] Mats L Gustafsson, Lin Shao, Peter Carlton, and Chung-Ju Rachel Wang. *Three-Dimensional Resolution Doubling in Wide-Field Fluorescence Microscopy by Structured Illumination.* ResearchGate, Biophysical Journal 94(12):4957-70, 2008.

[24] Fabian Göttfert, Christian A Wurm, Veronika Mueller, Sebastian Berning, Volker C Cordes, Alf Honigmann, and Stefan W Hell. *Coaligned Dual-Channel STED Nanoscopy and Molecular Diffusion Analysis at 20 Nm Resolution.* Biophys J. 2013;105(1):L01-L3. doi:10.1016/j.bpj.2013.05.029, 2013.

[25] Stefan W. Hell and Jan Wichmann. *Breaking the diffraction resolution limit by stimulated-emission—stimulated emission- depletion fluorescence microscopy.* Opt. Lett. 19, 780–782., 1994.

[26] Bo Huang, Mark Bates, and Xiaowei Zhuang. *Super resolution fluorescence microscopy.* NCBI PMC, 2014.

[27] Fang Huang, Tobias M P Hartwich, Felix E Rivera-Molina, Yu Lin, Whitney C. Duim, Jane J. Long, Pradeep D. Uchil, Jordan R. Myers, Michelle A. Baird, Walther Mothes, Michael W. Davidson, Derek Toomre, and Joerg Bewersdorf. *Video-rate nanoscopy using sCMOS camera–specific single-molecule localization algorithms.* Nature America, 2013.

[28] Fang Huang, Samantha L. Schwartz, Jason M. Byars, and Keith A. Lidke. *Simultaneous multiple-emitter fitting for single molecule super-resolution imaging.* OSA Publishing, 2016.

[29] Siewert Hugelier, Johan J. de Rooi, Romain Bernex, Sam Duwé, Olivier Devos, Michel Sliwa, Peter Dedecker, Paul H. C. Eilers, and Cyril Ruckebusch. *Sparse deconvolution of high-density super-resolution images.* Towards Data Science, 2016.

[30] Chen I and Ting AY. *Site-specific labeling of proteins with small molecules in live cells.* Curr. Opin. Biotechnol;16:35–40. [PubMed: 15722013], 2005.

[31] Kim I.Mortensen, L. Stirling Churchman, James A. Spudich, and Henrik FLyvbjerg. *Optimized localization-analysis for single-molecule tracking and super-resolution microscopy.* Nature Methods 7, 377-381, 2010.

[32] Yiming Li, Yuji Ishitsuka, Per Niklas Hedde, and G. Ulrich Nienhaus. *Fast and Efficient Molecule Detection in Localization-Based Super-Resolution Microscopy by Parallel Adaptive Histogram Equalization.* ACS Nano, 7, 6, 5207-5214, 2013.

[33] Jeff W Lichtman and José-Angel Conchello. *Fluorescence microscopy.* Nature Methods, 2005.

[34] Macmillan Publishers Limited. *Beyond the diffraction limit.* Nature Photonics 3, 361, 2009.

[35] Warren S. McCulloch and Walter Pitts. *A Logical Calculus of The Ideas Immanent in Nervous Activity.* Bulletin of Mathematical Biology Vol. 52, No. l/2. pp. 99-115, 1990.

[36] Junhong Min, Cédric Vonesch, Hagai Kirshner, Lina Carlini, Nicolas Olivier, Seamus Holden, Suliana Manley, Jong Chul Ye, and Michael Unser. *FALCON: fast and unbiased reconstruction of high-density super-resolution microscopy data.* Scientific Reports, 4, 4577, 2014.

[37] Steven M.Kay. *Fundamentals of statistical signal processing: estimation theory.* Prentice-Hall, Englewood Cliffs, NJ, USA, 1998.

[38] P. MucCullagh and J.A. Nelder. *Generalized linear models. 2nd Edition.* Chapman and Hall, 1989.

[39] Lin MZ and Wang L. *Selective labeling of proteins with chemical probes in living cells.* Science;281:269–272. [PubMed: 9657724], 1998.

[40] Elias Nehme, Lucien E. Weiss, Tomer Michaeli, and Yoav Shechtman. *Deep-STORM: super-resolution single-molecule microscopy by deep learning.* Phsysics Optics, 2018.

[41] Raimund J. Ober, Stripad Ram, and E.Sally Ward. *Localization Accuracy in Single-Molecule Microscopy.* Biophys., 2004.

[42] Wei Ouyang, Andrey Aristov, Mickaël Lelek, Xian Hao, and Christophe Zimmer. *Deep learning massively accelerates super-resolution localization microscopy.* Nature Biotechnology, 2018.

[43] Bernd Rieger and Sjoerd Stallinga. *The Lateral and Axial Localization Uncertainty in Super-Resolution Light Microscopy.* ChemsPhysChem, vol. 15, no.4, 664-670, 2014.

[44] Aldo Roda. *Discovery and development of the green fluorescent protein, GFP: the 2008 Nobel Prize.* Springer Link, Analytical and Bioanalytical Chemistry, 2008.

[45] Michael J. Rust, Mark Bates, and Xiaowei Zhuang. *Sub-diffraction-limit imaging by stochastic optical reconstruction microscopy (STORM).* Nat. Methods 3, 793, 2006.

[46] Hari Shroff, Helen White, and Eric Betzig. *Photoactivated Localization Microscopy (PALM) of Adhesion Complexes.* NCBI PMC, 2013.

[47] Alex Small and Shane Stahlheber. *Fluorophore localization algorithms for super-resolution microscopy.* Nature Methods, vol 11, no. 3, p. 267-279, 2014.

[48] Carlas S. Smith, Nikolai Joseph, Bernd Rieger, and Keith A. Lidke. *Fast, Single-Molecule Localization that Achieves Theoretically Minimum Certainty.* Nature Methods, 2010.

[49] Carlas Sierd Smith. *Optimum Single Molecule Localization Microscopy From Single Molecule Detections to Nanoscopic Observations.* Technical University of Delft, 2015.

[50] Artur Speiser, Srinivas C. Turaga, and Jakob H. Macke. *Teaching deep neural networks to localize sources in super-resolution microscopy by combing simulation-based learning and unsupervised learning.* arXiv:1907.00770, 2019.

[51] Petre Stoica and Thomas L. Marzetta. *Parameter Estimation Problems with Singular Information Matrices.* IEEE TRANSACTIONS ON SIGNAL PROCESSING, VOL. 49, NO. 1, 2001.

[52] F. Ströhl and C. F. Kaminski. *Frontiers in structured illumination microscopy.* Optica, vol. 3, p. 667, 2016.

[53] Johnny Tam and David Merino. *Stochastic optical reconstruction microscopy (STORM) in comparison with stimulated emission depletion (STED) and other imaging methods.* https://doi.org/10.1111/jnc.13257, 2015.

[54] Marcus Dyba Alexander Egner Thomas A. Klar, Stefan Jakobs and Stefan W. Hell. *Fluorescence microscopy with diffraction resolution barrier broken by stimulated emission.* Proceedings of the National Academy of Sciences, vol. 97, pp. 8206–8210, 2000.

Glossary

List of Acronyms

NA Numerical aperture
PSF Point spread function
OTF Optical transfer function
MTF Modulation transfer function
MLE Maximum likelihood estimation
MVU Minimum variance unbiased
MSE Mean squared error
GLRT Generalized likelihood ratio test
LS Least-squares
CoM Center of mass
CRLB Cramer-Rao Lower bound
FP Fluorescent protein
GFP Green fluorescent protein
SMLM Single-molecule localization microscopy
PALM Photo-activated localization microscopy
FPALM Fluorescence photo-activated localization microscopy
STORM Stochastic optical reconstruction microscopy
SIM Structured illumination microscopy
SSIM Saturated structured illumination microscopy
meLM Modulation-enhanced localization microscopy
STED Stimulated emission depletion
TIRF Total internal reflection fluorescence
GPU Graphics processing unit
ROI Region of interest
PDF Probability density function
EMCCD Electron-Multiplying Charge-Coupled Device
sCMOS scientific Complementary Metal-Oxide Semiconductor
ANN Artificial neural network
AI Artificial Intelligence